QUANTUM-BASED SPECTROSCOPY
AND
EFFICIENT ENERGY TRANSPORT WITH BIOMOLECULES

ROBERTO DE JESÚS LEÓN MONTIEL

under the supervision of
PROFESSOR JUAN P. TORRES

submitted this thesis in partial fulfillment
of the requirements for the degree of

Doctor

Acknowledgements

The work presented in this manuscript represents four hard, yet exciting years of my life. It is important to say that nothing of what you are about to read would have been possible without the support of all the people I met during this journey.

First of all, I would like to thank my advisor Prof. Juan P. Torres for giving me the opportunity to work in his group. Looking for new research directions, Juan motivated me to work on the exciting field of Quantum Biology. Even though this field was new for both of us, thanks to Juan's advice and support, we achieved all the objectives we set ourselves at the beginning of my Ph.D.

I cannot imagine doing all this work without the support of my parents Sara Josefina Montiel Feria and Juan León de la Vega. Every day of my life, they have encouraged me to pursue my dreams without hesitation. *Muchas gracias por su apoyo ma y pa.* Also, I would like to thank my brother Juan León Montiel and my sister Miriam León Montiel for all the good advices that they have given to me.

It was an honor to work, discuss and socialize together with all of the Quantum Engineering of Light group: Adam Vallés, Carmelo Rosales Guzmán, Jiří Svozilík, and Luis José Salazar Serrano.

I would like to thank ICFO's Managment, Administration and Engineering departments. Thanks to them ICFO is an absolutely great place to work, where the only thing you need to worry about is your research project.

Finally, I want to thank all my friends. I will keep you guys in my heart forever. As you already know, I am terrible at remembering names so, to avoid forgetting someone, I just want to say thank you all. These years would not have been the same without you.

Abstract

For many years, the fields of quantum optics and biology have rarely shared a common path. In quantum optics, most of the concepts and techniques developed over the years stand for systems where only a few degrees of freedom are considered and, more importantly, where the systems under study are assumed to be completely isolated from their surrounding environment. This situation is far from what we can find in nature. Biological complexes are, by definition, warm, wet and noisy systems subjected to environmental fluctuations, where quantum phenomena are unlikely to be observed. Notwithstanding, in recent years, this paradigm has begun to be questioned by several works where quantum-mechanical concepts have been introduced in order to describe the dynamics of important biological processes, such as energy transport in photosynthetic light-harvesting complexes.

The goal of this thesis is twofold. Firstly, we will investigate how ideas and techniques routinely used in quantum optics can be exploited in order to develop new quantum-based spectroscopy techniques and, secondly, we will examine to what extent microscopic quantum phenomena could impact on the efficient transport behavior of photosynthetic light-harvesting complexes. This problem is particularly relevant, because the understanding of fundamental mechanisms that enable the highly efficient transport of energy in photosynthetic systems could lead us to the design of future quantum-inspired light-harvesting technologies, such as high-efficiency organic solar cells.

The present thesis is organized as follows. In chapter 1, we will present a new technique to enhance the robustness and sensitivity of an optical label-free imaging system based on the interaction of coherent resonant pulses with an arbitrary sample via stimulated Raman adiabatic passage (STIRAP), which is a phenomenon that benefits from quantum coherence in order to enhance the flow of energy between the two light beams involved in the stimulated Raman process. Using this technique, in combination with a high-frequency phase-sensitive detection scheme, we will demon-

Abstract

strate that amazingly low concentration of atoms and molecules can be detected, up to 5 atoms of calcium and up to 20 molecules of neocyanine in a volume of 0.1 μm^3.

In chapter 2, we will use the light-matter interaction theory developed in the previous chapter to design a new experimental setup for measuring the temperature of atomic ensembles. The proposed scheme is based on a quantum interference effect that relates the temperature of an atomic ensemble with the emission cone width of Stokes photons that are spontaneously emitted when atoms are excited by an optical pulse. One of the attributes of this new technique is that, unlike commonly used time-of-flight measurements, the atomic cloud is not destroyed during each measurement.

The true role of entanglement in two-photon virtual-state spectroscopy, a two-photon absorption spectroscopy technique that allows one to retrieve information about the energy level structure of atoms or molecules, has been a controversial topic for years. In chapter 3, we will provide a thorough analysis of the virtual-state spectroscopy technique to show that, in the two-photon absorption process, the ability to obtain information about the energy level structure of a medium depends on the spectral shape of existing frequency correlations between the absorbed photons. Using this result, we will specify the type of two-photon source that is needed to experimentally implement virtual-state spectroscopy. In addition, by clarifying the role of entanglement in this technique, we will demonstrate that even paired photons carrying a low degree of entanglement, but with a proper spectral shape, can guarantee the successful retrieval of the energy level structure of the medium under study, thus showing that entanglement, by itself, is not the key ingredient to experimentally perform two-photon virtual state spectroscopy.

The last three chapters of this thesis are devoted to the description of energy transport in photosynthetic light-harvesting systems. In chapter 4, we will question recent claims that high-efficiency energy transport in light-harvesting complexes arises as a consequence of the quantum coherent evolution of the photosynthetic system and noise introduced by its surrounding environment, a process dubbed environment-assisted quantum transport or ENAQT. By using a classical stochastic model, we will explicitly demonstrate that highly efficient noise-assisted energy transport can be observed as well in purely classical systems. Using this result, we will propose an experimental setup, based on coupled classical electrical oscillators, where to observe the noise-assisted energy transport effect.

Motivated by the results presented in the previous chapter, we will implement, in chapter 5, the first phase of the experimental scheme proposed in chapter 4. It

consists of a setup that provides a unique tool to generate a tunable environment for classical electrical oscillators. We will illustrate the operation of the proposed setup by implementing the case of a damped random-frequency harmonic oscillator, where the tunability of the system is demonstrated by gradually changing the statistics of the oscillator's frequency distribution. The relevance of the proposed scheme resides in the fact that the high degree of tunability and control that it offers may allow us to design various types of noise with different probability distributions, which could be used in the study of non-Gaussian noise-induced effects. Moreover, it might allow us to study the transition from Markovian to non-Markovian dynamics of open systems.

In chapter 6, we provide the first study of the efficiency of photosynthetic energy transport where the initial excitation of the photosynthetic complex and the energy transfer to a reaction center are treated in more physically realistic ways. We will show that theoretical predictions are very sensitive to the details of these processes, especially to the energy transfer to the reaction center. We will demonstrate that the effect of ENAQT on the transport efficiency becomes negligible when considering more physically accurate models of energy transfer to a reaction center. Thus, we will call into question the widespread view that natural selection has optimized the interplay between quantum dynamics and noise in order to achieve a highly efficient photosynthetic energy transport.

Finally, because the topics addressed in this thesis are rather broad, we will present the conclusions in each chapter.

Resumen

Por muchos años, los campos de la óptica cuántica y la biología raramente han compartido un mismo camino. En la óptica cuántica, la mayoría de los conceptos y técnicas desarrolladas a lo largo de los años son válidas sólo en sistemas donde un número pequeño de grados de libertad es considerado y, más importante aún, donde se asume que los sistemas bajo estudio están completamente aislados del medio ambiente que los rodea. Esta situación está muy lejos de lo que podemos encontrar en la naturaleza. Los complejos biológicos son, por definición, sistemas a altas temperaturas, sujetos a fluctuaciones, en los cuales se cree que los fenómenos cuánticos son imposibles de observar. Sin embargo, en años recientes, esta creencia ha sido cuestionada por diferentes trabajos en los que conceptos de la mecánica cuántica han sido usados con el objetivo de describir la dinámica de procesos biológicos de gran importancia como, por ejemplo, el transporte de energía en los complejos de captación de luz en sistemas fotosintéticos.

El objetivo de esta tesis se divide en dos. Primeramente, investigaremos cómo las ideas y técnicas usadas comunmente en óptica cuántica pueden ser explotadas con el objetivo de desarrollar nuevas técnicas de espectroscopía y, segundo, estudiaremos hasta que punto los fenómenos cuánticos microscópicos pueden influir en el comportamiento del transporte eficiente de energía en sistemas fotosintéticos de captación de luz. Este problema es particularmente relevante, pues el entender los mecanismos fundamentales que permiten un eficiente transporte de energía en sistemas fotosintéticos nos podría conducir al diseño de nuevas tecnologías de captación y recolección de energía como, por ejemplo, celdas solares orgánicas de alta eficiencia.

La presente tesis está organizada de la siguiente forma. En el capítulo 1 presentaremos una nueva técnica para mejorar la robustez y sensibilidad de un sistema óptico de obtención de imágenes sin etiquetas, basado en la interacción de pulsos resonantes coherentes con una muestra biológica arbitraria a través del proceso conocido como paso adiabático estimulado de Raman o STIRAP por sus siglas en inglés, el cual hace

Resumen

uso de la coherencia cuántica con el objetivo de mejorar el flujo de energía entre los dos haces de luz involucrados en el proceso estimulado de Raman. Usando esta técnica, en combinación con un esquema de detección de alta frecuencia, sensible a la fase, demostraremos que es posible detectar muy bajas concentraciones de átomos y moléculas; hasta 5 átomos de calcio y hasta 20 moléculas de neocyanine en un volumen de 0.1 μm^3.

En el capítulo 2, usaremos la teoría de interacción luz-materia desarrollada en el capítulo anterior, para diseñar un montaje experimental de medición de temperatura de ensambles atómicos. El esquema propuesto está basado en un efecto de interferencia cuántica que relaciona la temperatura de un ensamble atómico con el tamaño del cono de emisión de fotones Stokes, que son emitidos de forma espontánea cuando los átomos en el ensamble son excitados por un pulso óptico. Uno de los principales atributos de esta nueva técnica es que, a diferencia de los métodos de medición basados en el tiempo-de-vuelo de los átomos, TOF por sus siglas en inglés, la nube atómica no es destruída durante cada medición.

El verdadero papel que juega el entrelazamiento en la espectroscopía de estados virtuales, una técnica de espectroscopía de absorción de dos fotones que permite extraer información de la estructura energética de átomos y moléculas, ha sido un tema controversial por muchos años. En el capítulo 3, haremos un análisis exhaustivo de la técnica de espectroscopía de estados virtuales para mostrar que, en el proceso de absorción de dos fotones, la posibilidad de obtener información acerca de la estructura de los niveles de energía de un medio arbitrario, depende de la forma espectral de las correlaciones en frecuencia entre los fotones que son absorbidos por el medio. Usando este resultado, especificaremos el tipo de fuente de pares de fotones que es necesario para implementar experimentalmente la espectroscopía de estados virtuales. Adicionalmente, al clarificar el verdadero papel que juega el entrelazamiento en esta técnica, demostraremos que incluso pares de fotones débilmente entrelazados, pero con una forma espectral correcta, pueden garantizar la extracción exitosa de la estructura energética del medio bajo estudio, mostrando así, que el entrelazamiento por si sólo no es el ingrediente clave para realizar experimentalmente la espectroscopía de estados virtuales.

Los últimos tres capítulos de esta tesis están dedicados a describir el transporte de energía en sistemas fotosintéticos de captación de luz. En el capítulo 4, cuestionaremos recientes ideas en las que se describe a la alta eficiencia en el transporte de energía de complejos fotosintéticos como consecuencia de la interacción entre la evolución cuán-

tica del sistema y el ruido introducido por el medio ambiente que lo rodea, un proceso conocido como transporte cuántico asistido por ruido o ENAQT por sus siglas en inglés. Haciendo uso de un modelo clásico estocástico, demostraremos explícitamente que el transporte de energía de alta eficiencia asistido por ruido, puede ser observado también en sistemas puramente clásicos. Usando este resultado, propondremos un arreglo experimental, basado en osciladores electrónicos clásicos acoplados, donde se puede observar el efecto de transporte de energía asistido por ruido.

Motivados por los resultados presentados en el capítulo anterior, implementaremos, en el capítulo 5, la primera fase del esquema experimental propuesto en el capítulo 4. El esquema consiste en un montaje electrónico que permite generar ruido sintonizable para osciladores eléctricos clásicos. Mostraremos el funcionamiento del arreglo propuesto, implementando el caso de un oscilador armónico amortiguado con una frecuencia aleatoria. El control que ofrece nuestro sistema es demostrado al cambiar, de forma gradual, la estadística de la distribución de frecuencias del oscilador. La relevancia del sistema propuesto reside en que el alto nivel de control y sintonización que ofrece, puede ser utilizado para diseñar varios tipos de ruido con diferentes distribuciones de probabilidad que, a su vez, podrían ser utilizados en el estudio de efectos inducidos por ruido no-Gaussiano. Además, este arreglo experimental nos permitiría estudiar la transición de la dinámica Markoviana a no-Markoviana en sistemas abiertos.

En el capítulo 6, presentaremos el primer estudio de la eficiencia de transporte de energía fotosintética en el cual la excitación inicial del complejo fotosintético y la transferencia de energía al centro de reacción fotoquímico son tratados de una forma físicamente realista. Mostraremos que las predicciones teóricas son muy sensibles a los detalles de estos procesos, especialmente a la transferencia de energía al centro de reacción. Demostraremos que el efecto de ENAQT en la eficiencia de transporte es despreciable cuando se consideran modelos más precisos de transferencia de energía al centro de reacción. Usando este resultado, cuestionaremos la idea de que la selección natural ha optimizado la interacción entre la dinámica cuántica y el ruido, con el objetivo de alcanzar una alta eficiencia en el transporte fotosintético de energía.

Finalmente, debido a que los temas abordados en esta tesis son bastante amplios, presentaremos las conclusiones en cada capítulo.

List of publications

This thesis is based on the following publications:

- **R. de J. León-Montiel** and Juan P. Torres, *Enhancing the sensitivity and robustness of label-free imaging systems via stimulated Raman adiabatic passage*, New. J. Phys. **14**, 013018 (2012).

- **R. de J. León-Montiel** and Juan P. Torres, *Measurement of the temperature of atomic ensembles via which-way information*, Phys. Rev. A **85**, 033801 (2012).

- **R. de J. León-Montiel**, J. Svozilík, L. J. Salazar-Serrano, and Juan P. Torres, *Role of the spectral shape of quantum correlations in two-photon virtual-state spectroscopy*, New J. Phys. **15**, 053023 (2013).

- **R. de J. León-Montiel** and Juan P. Torres, *Highly efficient noise-assisted energy transport in classical oscillator systems*, Phys. Rev. Lett. **110**, 218101 (2013).

- **R. de J. León-Montiel**, J. Svozilík, and Juan P. Torres, *Generation of a tunable environment for electrical oscillator systems*, Phys. Rev. E **90**, 012108 (2014).

- **R. de J. León-Montiel**, Ivan Kassal, and Juan P. Torres, *The importance of excitation and trapping conditions in photosynthetic environment-assisted energy transport*, submitted.

Other publications by the author:

- S. Palacios, **R. de J. León-Montiel**, M. Hendrych, A. Valencia, and Juan P. Torres, *Flux enhancement of photons entangled in orbital angular momentum*, Opt. Express **15**, 14108 (2011).

List of publications

- J. Svozilík, **R. de J. León-Montiel**, and Juan P. Torres, *Implementation of a spatial two-dimensional quantum random walk with tunable decoherence*, Phys. Rev. A **86**, 052327 (2012).

- Y. A. de Icaza Astiz, V. G. Lucivero, **R. de J. León-Montiel**, and M. W. Mitchell, *Optimal signal recovery for pulsed balanced detection*, arXiv:1403.7085 [quant-ph].

Contents

Chapter 1

Enhancing the sensitivity of label-free imaging systems via stimulated Raman adiabatic passage

Label-free optical imaging deals with the problem of detecting the presence of specific molecular species without the use of auxiliary alien substances, such as fluorophores. To address this issue, what is needed is an efficient, highly selective technique capable of sampling specific vibrations of atoms or molecules, and this can be provided by resonance Raman spectroscopy [1].

In 2008, an optical label-free imaging technique based on stimulated Raman scattering (SRS) was demonstrated [2, 3]. In this technique, the frequency difference between two pulses (pump and Stokes) is tuned in order to match the atomic frequency transition between two energy levels, which results in the depletion of the pump and, consequently, in the amplification of the Stokes beam via a stimulated Raman transition. Using a high-frequency phase-sensitive detection technique, Freudiger *et al.* [2] managed to measure a stimulated Raman loss (SRL) $\Delta E_p/E_p \sim 10^{-7}$, where E_p is the initial energy of the pump pulse and ΔE_p is the loss experienced by the pulse. This value of the SRL corresponds, for instance, to detecting a concentration of some $50\mu M$ (molecule number density of 10^{16} cm^{-3}) of retinol.

Here, we introduce a new technique that combines the above mentioned optical imaging scheme with a quantum optics technique that enhances the transfer of atomic populations, namely stimulated Raman adiabatic passage (STIRAP). Using a STIRAP

(a)   (b)
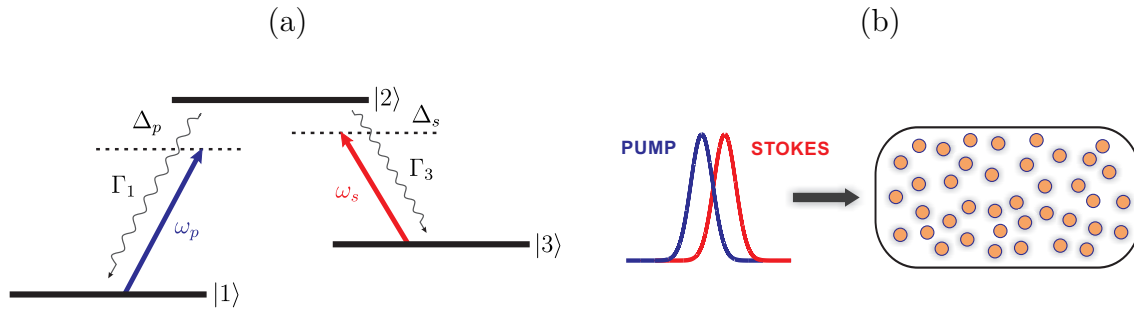
Fig. 1.1 (a) Scheme of a three-level system in Λ configuration. (b) Ensemble of three-level atoms shined by two temporally delayed classical pulses.

configuration, we show that one can, in principle, go beyond the current level of sensitivity, i.e., lowering the minimum concentration of molecules that can be detected, while at the same time enhancing the robustness of the system against variations in the laser parameters: intensities, detunings, pulse shapes, pulse widths and pulse delays. This high sensitivity could also be employed for detecting a larger number of molecules within a shorter acquisition time, which is of great importance in applications such as *in-vivo optical imaging*, a technique that requires primarily high speed.

This chapter is organized as follows. Section 2.1 provides the theoretical framework of the proposed technique. Section 2.2 describes the robustness and high efficiency that STIRAP can offer to label-free imaging systems. Finally, Section 2.3 shows how STIRAP could enable the detection of very low concentration of atoms and molecules.

1.1 Basic equations

Stimulated Raman adiabatic passage is a robust process that benefits from quantum coherence to enhance the population transfer between two quantum states of an atom, ion or molecule by means of two coherent light pulses [4–7]. In general, STIRAP can be modeled by considering an ensemble of atoms, with concentration N, where individual atoms are described as a three-level system in a Λ configuration, as depicted in Fig. 1.1. Each of the states is non-degenerate and there is no direct coupling between states $|1\rangle$ and $|3\rangle$. The atoms interact with two light pulses. The pump pulse, with central frequency ω_{p}, couples the state $|1\rangle$ with the intermediate state $|2\rangle$, and the Stokes pulse, with central frequency ω_{s}, couples the state $|3\rangle$ with the state $|2\rangle$. Because coherent phenomena are important in the STIRAP process, specific energy level configurations and nearly transform limited pulses are needed [8].

The Hamiltonian that describes the interaction of the atoms with the two pulses can be written in the rotating-wave approximation as [5]

$$H\left(t\right) = \frac{\hbar}{2} \begin{bmatrix} 0 & \Omega_{\mathrm{p}}^{*}\left(t\right) & 0 \\ \Omega_{\mathrm{p}}\left(t\right) & 2\Delta_{\mathrm{p}} & \Omega_{\mathrm{s}}\left(t\right) \\ 0 & \Omega_{\mathrm{s}}^{*}\left(t\right) & 2\left(\Delta_{\mathrm{p}} - \Delta_{\mathrm{s}}\right) \end{bmatrix}, \tag{1.1}$$

where $\Omega_{\mathrm{p}}\left(t\right) = -\boldsymbol{\mu}_{12} \cdot \mathbf{E}_{\mathrm{p}}/\hbar$ and $\Omega_{\mathrm{s}}\left(t\right) = -\boldsymbol{\mu}_{32} \cdot \mathbf{E}_{\mathrm{s}}/\hbar$ are the Rabi frequencies of the pump and Stokes pulses, respectively, and the coefficients $\boldsymbol{\mu}_{12}$ and $\boldsymbol{\mu}_{32}$ describe the dipole moments for each transition. Here, $\Delta_{\mathrm{p}} = \omega_{21} - \omega_{\mathrm{p}}$ and $\Delta_{\mathrm{s}} = \omega_{23} - \omega_{\mathrm{s}}$ correspond to the detunings of the pump and Stokes frequencies, respectively.

To introduce dissipation effects from level $|2\rangle$ to levels $|1\rangle$ and $|3\rangle$, we model the dynamics of the system by means of the Lindblad equation

$$i\hbar \frac{d\rho}{dt} = [H, \rho] + \mathcal{L}_{\mathrm{diss}}[\rho], \tag{1.2}$$

where ρ is the density matrix of the system and $\mathcal{L}_{\mathrm{diss}}$ is a Lindblad operator that describes the spontaneous emission within the three-level system. This operator is defined by [9]

$$\mathcal{L}_{\mathrm{diss}}[\rho] = \begin{bmatrix} -2\Gamma_1\rho_{22} & (\Gamma_1 + \Gamma_3)\rho_{12} & 0 \\ (\Gamma_1 + \Gamma_3)\rho_{21} & 2(\Gamma_1 + \Gamma_3)\rho_{22} & (\Gamma_1 + \Gamma_3)\rho_{23} \\ 0 & (\Gamma_1 + \Gamma_3)\rho_{32} & -2\Gamma_3\rho_{22} \end{bmatrix}, \tag{1.3}$$

where Γ_1 and Γ_3 are the decay rates from state $|2\rangle$ to states $|1\rangle$ and $|3\rangle$, respectively.

The measurement of atom (molecule) concentrations in an extended area requires considering the changes of the pump and Stokes pulses while they propagate through the sample [10, 11]. If we make use of the slowly varying envelope approximation, the wave equations that describe the evolution of the pump and Stokes fields can be written, in terms of the corresponding Rabi frequencies, as [12]

$$\left(\frac{\partial}{\partial t} + \mathrm{c}\frac{\partial}{\partial z}\right) \Omega_{\mathrm{p}}\left(z, t\right) = -i\alpha_{\mathrm{p}}\rho_{12}^{*}, \tag{1.4}$$

$$\left(\frac{\partial}{\partial t} + \mathrm{c}\frac{\partial}{\partial z}\right) \Omega_{\mathrm{s}}\left(z, t\right) = -i\alpha_{\mathrm{s}}\rho_{32}^{*}, \tag{1.5}$$

where c is the speed of light and ρ_{ij} $(i, j = 1, 2, 3)$ are the elements of the density matrix

and ρ_{ij}^* stands for the complex conjugate of ρ_{ij}. The effect of the atomic medium on the pump and Stokes pulses propagation depends on the two absorption coefficients: $\alpha_\mathrm{p} = \omega_\mathrm{p} \mathrm{N} |\mu_{21}|^2 / \epsilon_0 \hbar$ and $\alpha_\mathrm{s} = \omega_\mathrm{s} \mathrm{N} |\mu_{23}|^2 / \epsilon_0 \hbar$, with ϵ_0 being the vacuum permittivity. In writing Eqs. (1.4) and (1.5) we have considered that the fields propagate parallel to the z-direction and that the medium is homogeneous, so atoms are assumed to be fixed and uniformly distributed within the ensemble. Equations (1.2), (1.4) and (1.5) constitute the mathematical description of the system under study. Due to the complexity of the system of partial differential equations, we need to numerically solve them in a moving frame defined by the variables $t' = t - z/\mathrm{c}$ and $z' = z$ (see Appendix A for further details).

1.2 Robustness and high efficiency of STIRAP

To provide a thorough analysis of the robustness and high efficiency that STIRAP can offer to label-free imaging systems, we have solved the set of equations described in the previous section by using a $^{40}\mathrm{Ca}^+$ ions ensemble as model system. In our simulations, we have considered the atomic levels $4^2 S_{1/2}$, $4^2 P_{1/2}$ and $3^2 D_{3/2}$ for the states $|1\rangle$, $|2\rangle$ and $|3\rangle$, respectively. Their corresponding transition lifetimes are taken to be $\Gamma_1^{-1} = 7.7$ ns and $\Gamma_3^{-1} = 94.3$ ns. The initial condition of the atomic system is then defined by considering that atoms are initially in the state $|1\rangle$, so the elements of the initial density matrix read as

$$\rho_{11}(0) = 1, \quad \rho_{ij}(0) = 0 \quad (ij \neq 1). \tag{1.6}$$

For the light excitation, we assume that the initial pump and Stokes pulses exhibit a Gaussian shape given by

$$\Omega_{\mathrm{p,s}}(t) = \Omega_0 \exp\left\{-4\ln 2 \left[(t \pm \tau/2)/\mathrm{T}\right]^2\right\}, \tag{1.7}$$

where T is the full pulse width at half maximum, Ω_0 is the peak Rabi frequency and τ is the temporal delay between the pulses. Notice that, in order to reduce harmful effects of the spontaneous decay, we need to employ light pulses with time duration much shorter than the lifetime of each transition.

To provide a point of comparison, in what follows, we will compare STIRAP with SRS based on overlapping pulses. Such comparison has been experimentally done for instance, in the picosecond multiphoton detection of sodium [13].
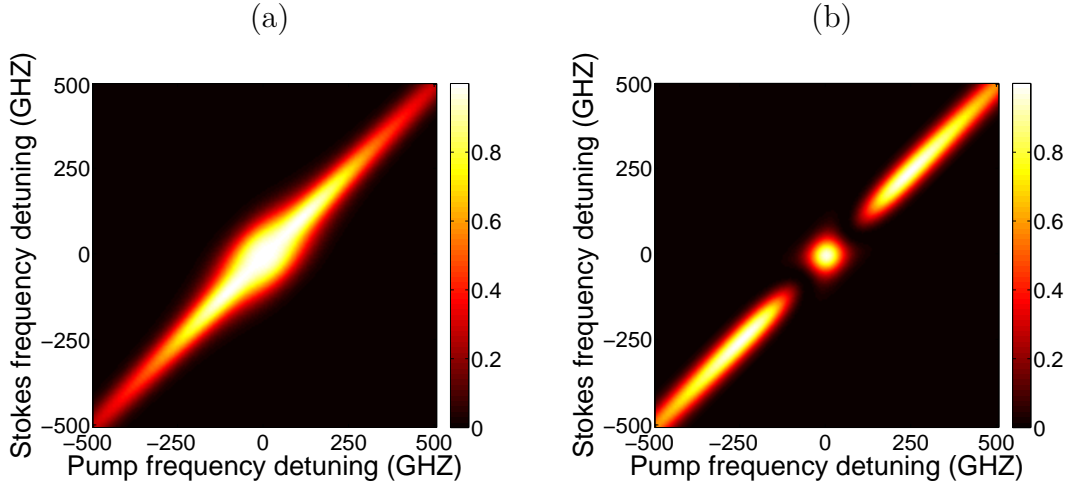
Fig. 1.2 Contour plot of the fraction of population transferred to level $|3\rangle$ as a function of the detuning from the atomic resonances of the pump (Δ_p) and the Stokes (Δ_s) pulses for (a) STIRAP, and (b) overlapping pulses.

STIRAP can achieve complete population transfer between states $|1\rangle$ and $|3\rangle$ if the quantum state of the atom can follow adiabatically one particular time-dependent eigenstate of the Hamiltonian given by Eq. (1.1), the so-called dark state [5]. Two conditions must be satisfied for trapping the system in a dark-state [4]. Firstly, the frequencies of the pulses need to be tuned to the two-photon resonance regime, i.e., $\Delta_p = \Delta_s$. Figure 1.2 shows the fraction of population transferred to the state $|3\rangle$ as a function of the detunings of the pump and Stokes pulses. Notice from Fig. 1.2(a) that one-photon resonance ($\Delta_p = \Delta_s = 0$) is not a requisite for achieving an efficient transfer of population when using a STIRAP configuration. In contrast, when performing SRS with overlapping pulses, the amount of atomic population transferred to the state $|3\rangle$ do in fact depend on the one-photon condition, as shown in Fig. 1.2(b).

The second and most distinguishing condition is that the evolution of the fields must be adiabatic, following a counterintuitive ordering of the light pulses [14]. The system starts with all the population in the ground state $|1\rangle$ and the Stokes field Ω_s is applied first. In this case, the initial state of the system corresponds exactly to the dark state. Afterwards, Ω_p is adiabatically increased and, at the same time, Ω_s is decreased until the condition $\Omega_p \gg \Omega_s$ is reached. In this scenario, all the population can be transferred to the state $|3\rangle$, with almost 100% efficiency.

We can produce nearly complete population transfer between states $|1\rangle$ and $|3\rangle$ when the pump and Stokes pulses overlap. However, SRS with overlapping pulses

Enhancing the sensitivity of label-free imaging systems via stimulated Raman adiabatic passage

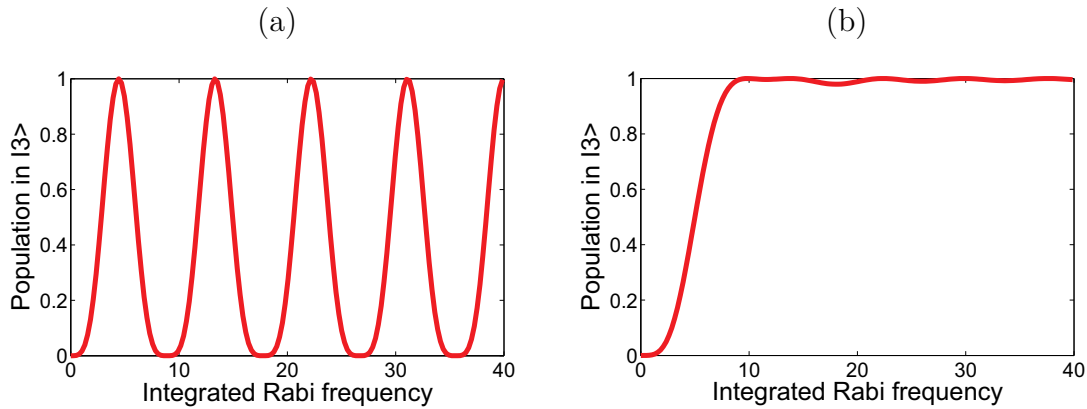(a)   (b)

Fig. 1.3 Fraction of atomic population transferred to level $|3\rangle$ as a function of the integrated Rabi frequency of pulses with time duration T = 10 ps and pulse delays (a) $\tau = 0$, (b) $\tau = 0.55$ T.

is not so robust against changes in the shape or intensity of the pulses, features that could change due to variations in the laser parameters or the propagation of the pulses through the ensembles. Figure 1.3 shows the fraction of atoms that reach state $|3\rangle$ as a function of the integrated Rabi frequency, i.e. $A = \int \Omega(t)\, dt$, for the case of overlapping pulses ($\tau = 0$) and the STIRAP configuration with temporal delay $\tau = 0.55$T. To understand why STIRAP is more robust against changes in the pulse shapes than the overlapping pulses configuration, let us assume that the initial pulses have an initial Rabi frequency Ω_0 so that $A = 13$, which corresponds to nearly 100% population transfer in both configurations. For the case of overlapping pulses, increases of 10% in the integrated Rabi frequency of the pulses diminish the population transfer to $\sim 50\%$, while decreases of 10% produce a population transfer of $\sim 70\%$. On the contrary, in the STIRAP regime, a nearly complete transfer of population is produced within the same range of variations.

Information about the number of atoms or molecules that constitute the sample under study is retrieved by measuring the stimulated Raman Gain (SRG), i.e. $\Delta E_s / E_s$, where ΔE_s is the gain in energy of the Stokes pulse and E_s is the energy carried by the initial Stokes pulse. As previously mentioned, the integrated Rabi frequency is set to $A = 13$, which maximizes the transfer of population for both the SRS with overlapping and non-overlapping pulses, as depicted in Fig. 1.4(a).

Figure 1.4(b) shows the change of SRG as a function of the distance traversed by the pulses through a sample with an ion number density of 10^{18} cm^{-3}. We can observe that the SRG is always higher in the STIRAP configuration. Furthermore,

(a)

(b)

(c)
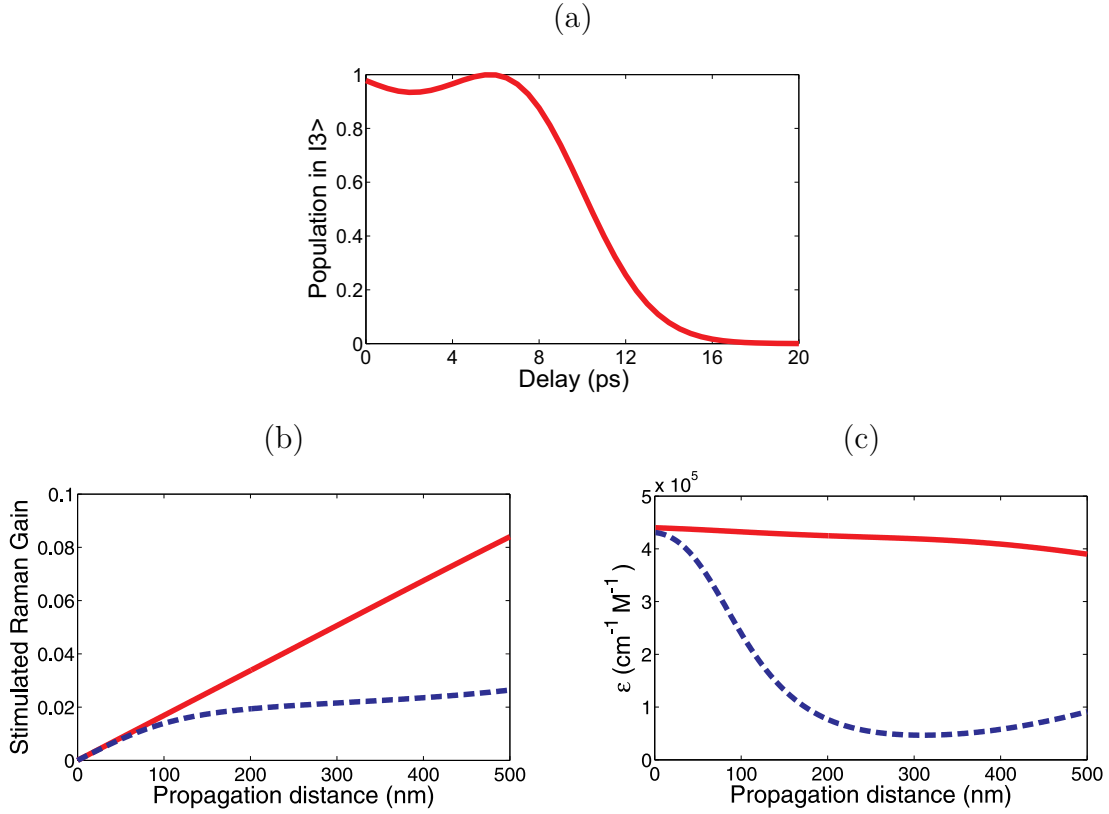
Fig. 1.4 (a) Population transferred to level $|3\rangle$ as a function of the delay between pulses. (b) SRG as a function of the propagation distance through a sample with an ion number density of 10^{18} cm^{-3}. (c) Molar amplification coefficient as a function of the distance. Solid line: STIRAP; dashed line: overlapping pulses.

the information provided by Fig. 1.4(b) can be used in order to analyze how the light absorption changes when propagating along the sample. To this end, we compute the effective molar amplification coefficient ϵ, which is a measure of how strongly a sample absorbs light at a given wavelength. This coefficient is defined by $\epsilon = A/\mathrm{N}L$, where A is the absorbance of the sample and L is the pathlength [15]. Figure 1.4(c) shows the effective molar amplification (in units of M^{-1}cm^{-1}) as a function of the propagation distance. Notice that, in the initial stages of propagation, the pulses experience small changes that do not affect the absorption properties of the sample. However, as the pulses continue to propagate, their shapes and temporal delays start to change [see Fig. 1.5(a)]. One can see that, even though the changes in the integrated Rabi frequency are comparable in both cases [see Fig. 1.5(b)], the effective molar amplification coefficient remains practically unchanged for STIRAP, while it decreases in the case of overlapping pulses.
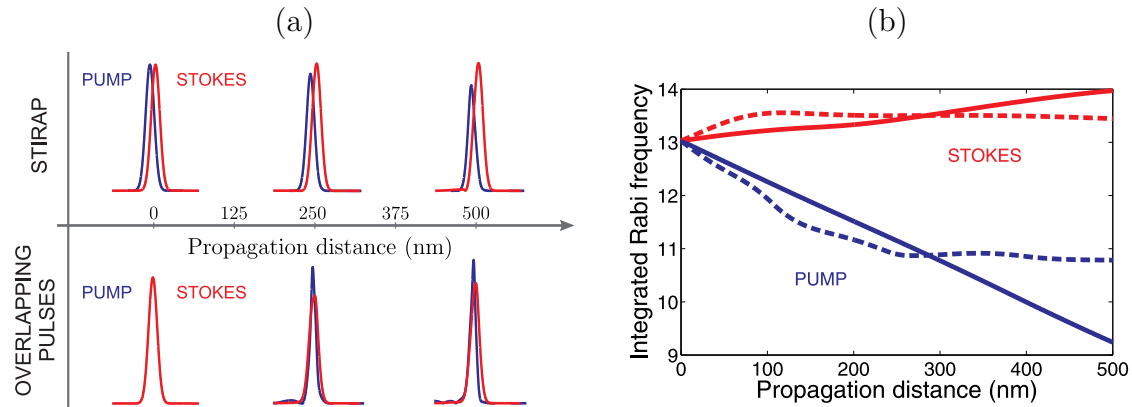
Fig. 1.5 (a) Shapes of the pump and Stokes pulses during propagation. (b) Evolution of the integrated Rabi frequency of the pulses propagating in STIRAP (solid line) and overlapping pulse (dashed line) configurations.

We have observed that when considering samples containing a high concentration of atoms or molecules ($> 10^{18}$ cm^{-3}), the SRG is always higher with STIRAP. However, as we will see in the next section, for low concentration samples, variations in the SRG are no longer due to propagation through the sample, but to the precise preparation of the initial pulses.

1.3   Highly sensitive molecular detection

Optical imaging based on SRS is especially suited for detecting very low concentrations of atoms or molecules. In particular, the combination of such technique together with STIRAP provides a higher sensitivity than the commonly used overlapping pulses configuration.

Figure 1.6 shows that in low concentration samples, both SRS configurations yield the same linear dependence between concentration and SRG, with an effective molar amplification coefficient $\epsilon = 440000$ M^{-1}cm^{-1}. This value of the molar amplification coefficient represents a sensitivity enhancement that would allow us to detect concentrations of up to $\sim 10^{13}$ cm^{-3}. We can observe from Fig. 1.6(b) that SRS with STIRAP always achieves a higher sensitivity than SRS with overlapping pulses. Moreover, notice that fractional changes in the initial integrated Rabi frequency do not modify substantially the molar amplification coefficient in the case of STIRAP; whereas in the case of overlapping pulses, a fractional change of 20% could severely affect the sensitivity.

Fig. 1.6 (a) Stimulated Raman Gain as a function of the ion number density. (b) Molar amplification coefficient as a function of the fractional change in the integrated Rabi frequency of the pulses initially prepared in STIRAP (solid line) and overlapping pulse (dashed line) configurations. Propagation distance is set to $L = 500$ nm.

At this point, we have presented the efficiency enhancement for detecting Calcium ions; however, since our interest resides in molecular systems, we now turn our attention to ensembles of neocyanine molecules. This molecule is of great chemical interest due to its intense absorption (180000 $M^{-1}cm^{-1}$) and short excited lifetimes (~ 120 ps) [16]. Because of these properties, neocyanine has already been considered as a test molecule in experimental realizations of label-free imaging [17, 18].

The level configuration for neocyanine is shown in Fig. 1.7(a). Transitions $|1\rangle \rightarrow |2\rangle$ and $|3\rangle \rightarrow |2\rangle$ are excited by laser pulses with central wavelength of 770 nm and 850 nm, respectively. We illuminate the sample with 15 fs pulses and a time delay of 9.33 fs between them (STIRAP configuration). The laser is set to have 4 mW average power and 80 MHz repetition rate. For the sake of comparison with Refs. [17, 18], we have assumed that the pulses have a transversal section S~ 1 μm^2 and that they propagate 100 nm within the sample. From these parameters, we obtain a volume in the laser focus of 10^{-19} m^3 (10^{-16} L).

Figure 1.7(b) shows the SRG as a function of the neocyanine concentration. Notice that by using a STIRAP configuration we can obtain an effective molar amplification coefficient of $\epsilon = 11350$ $M^{-1}cm^{-1}$. This value of the molar amplification coefficient represents a sensitivity enhancement that would allow us to detect concentrations of up to ~ 0.5 μM, which is a concentration ten and two times smaller than previously reported in Refs. [17] and [18], respectively.

Enhancing the sensitivity of label-free imaging systems via stimulated Raman adiabatic passage

(a)

(b)
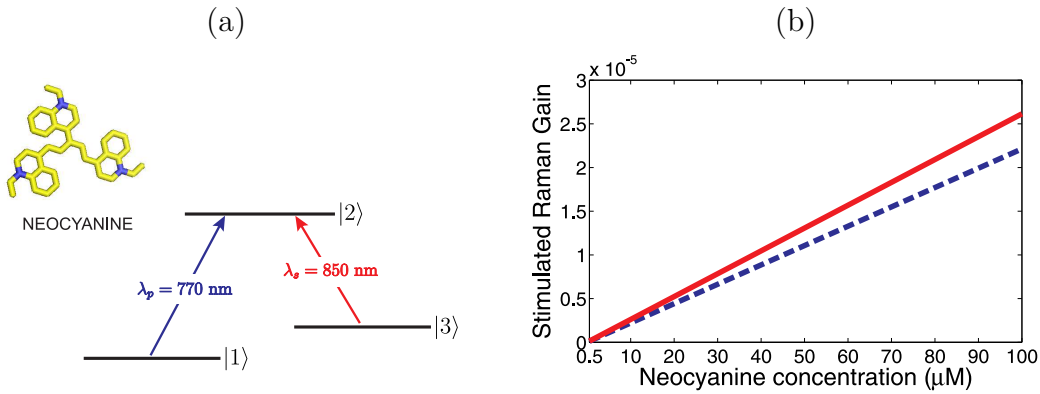
Fig. 1.7 (a) Scheme of the neocyanine three-level configuration. (b) Stimulated Raman Gain as a function of the concentration of neocyanine for pulses propagating in STIRAP (solid line) and overlapping pulse (dashed line) configurations. Propagation distance is set to $L = 100$ nm. The figure of neocyanine molecule was drawn using PyMOL [19].

Conclusions

In this chapter, we have described a new technique to enhance the robustness and sensitivity of an optical label-free imaging technique based on SRS. The proposed technique is based on the interaction of coherent resonant pulses with a specific sample via stimulated Raman adiabatic passage. In principle, in combination with a high-frequency phase-sensitive detection scheme, it allows one to detect amazingly low concentrations of atoms and molecules. For instance, with an effective molar amplification coefficient of 440000 $M^{-1}cm^{-1}$ and SRG $> 10^{-7}$, it is possible to detect $n \sim 10^{-7} S/(2.303\epsilon)$ ions, which for $S \sim 10 \ \mu m^2$ yields $n \sim 5$ ions.

In the case of molecular ensembles, we have shown that using a STIRAP configuration, an effective molar amplification coefficient of 11350 $M^{-1}cm^{-1}$ can be obtained. For this value of the molar coefficient, a SRG $> 10^{-7}$ and $S \sim 1 \ \mu m^2$, we could experimentally detect $n \sim 20$ neocyanine molecules, which is two times smaller than the lowest reported value.

We have observed that when using a STIRAP configuration, the SRG remains linear with respect to the concentration of molecules and the propagation distance traveled by the pulses, which enables a straightforward quantitative analysis. Finally, we have demonstrated that STIRAP is less sensitive to changes in the energy or shape of the initial pulses, which would make it easy to experimentally carry out under realistic experimental conditions.

Chapter 2

A new technique for measuring the temperature of atomic ensembles

Atomic ensembles provide a robust platform for many theoretical and experimental schemes for the implementation of several quantum information protocols [20, 21] and, in particular, for the generation of paired photons with non-classical correlations [22, 23]. In these photon-generation schemes, a weak classical field (pump pulse) interacts with an atomic ensemble leading to the spontaneous emission of a photon with a lower energy (Stokes photon). Since the Stokes photon and the atomic ensemble are highly correlated, the projection of the Stokes photon results in the generation of an atomic state that is a coherent superposition of all possible states of the ensemble where only one atom is excited, the so-called collective atomic state [24].

Although in most experiments the emitted Stokes photons are detected at small angles ($\sim 0° - 3°$) [22, 23, 25–27], the direction in which they can be emitted from the atomic cloud has been a subject of study for years. For instance, it has been shown that in the case of room-temperature ensembles, where atoms are considered to move fast within the cloud, Stokes photons are emitted within a small cone around the direction of propagation of the pump beam [28, 29]. In contrast, for the case in which atoms are considered to be fixed in their positions, as in cold atomic ensembles, Stokes photons have no preferred direction of emission [30, 31], always that it is not forbidden by the transition matrix elements. These results consider only the angular distribution of emitted photons in two limiting cases: when atoms are either moving very fast (high temperature) or completely fixed (low temperature) within the cloud.

However, the transition between these two cases had not been investigated before.

In this chapter, we construct a theoretical model that allows us to describe the angular distribution of emitted Stokes photons as a function of the temperature of the atomic ensemble. Then, by making use of this model, we develop a new technique where the measurement of the width of the Stokes emission cone is used to determine the temperature of the atomic cloud. Moreover, we demonstrate that such measurement can be done thanks to the close relationship that exists between the range of possible directions of emission, and the *which-way* information available about where the photon originated, i.e., knowledge of the position of the atom that emitted the photon during the light-matter interaction. The importance of the proposed technique resides in the fact that, unlike commonly used time-of-flight measurement [32], the atomic cloud is not destroyed during each measurement. Therefore, this new technique takes a place in the group of nondestructive measurements, such as resonance fluorescence spectrum analysis [33], recoil-induced resonances [34], and transient four-wave mixing [35], with the difference that it does not require any additional elements in the basic writing-reading experimental setup, which makes it appealing for its implementation.

This chapter is organized as follows. Section 2.1 presents the developed theoretical model. In Section 2.2, we make use of the new model to investigate the angular distribution of emitted Stokes photons as a function of the temperature of the atomic ensemble. Finally, Section 2.3 describes the proposed experimental scheme for measuring the temperature of atomic clouds.

2.1 The model

Imagine the scenario where an ensemble of N identical three-level atoms in Λ configuration (Fig. 2.1) is illuminated by a weak laser pulse coupling the transition $|g\rangle \rightarrow |e\rangle$ with a detuning Δ. Then, after some time, spontaneous decay of an atom in the ensemble leads to the generation of a photon with different wavelength (Stokes photon), leaving the atom in the symmetric state $|s\rangle$. In this situation, how could we know the direction in which the Stokes photon is emitted? Furthermore, how would the path of the photon be related, if so, to the temperature of the ensemble? To address these questions, we proceed as follows.

We consider the pump beam as a slowly varying classical field propagating along the z direction, with a Rayleigh range much larger than the length of the atomic
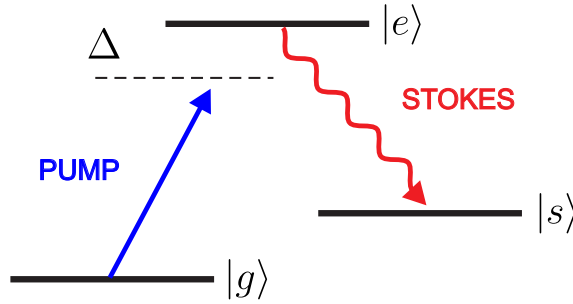
Fig. 2.1 Three-level atom in Λ configuration. Transition from the ground $|g\rangle$ to the excited state $|e\rangle$ is produced by a weak pump pulse with detuning Δ. After excitation, a photon with lower energy (Stokes photon) is spontaneously emitted, leaving the atom in the symmetric state $|s\rangle$.

ensemble, defined as

$$E_{\mathrm{p}}\left(\mathbf{r}, t\right) = u\left(\mathbf{r}_{\perp}\right)\xi(t)\exp\left\{ik_0 z - i\omega_0 t\right\} + \mathrm{H.c.}, \tag{2.1}$$

where $\omega_0 = k_0 \mathrm{c}$ is the central frequency, c is the speed of light, $u\left(\mathbf{r}_{\perp}\right)$ describes the transverse spatial shape of the pump beam and $\xi(t)$ its temporal shape. Here, H.c. stands for the Hermitian conjugate.

Because only one Stokes photon is emitted by the ensemble, the Stokes field is taken as a quantum field described by the expression

$$\hat{E}_{\mathrm{s}}^{\dagger}\left(\mathbf{r}, t\right) = \int \hat{a}(\mathbf{k})\exp\left\{i\mathbf{k}\cdot\mathbf{r} - i\omega t\right\}d\mathbf{k}, \tag{2.2}$$

where $\hat{a}(\mathbf{k})$ is the annihilation operator, $\mathbf{k} = (k_x, k_y, k_z)$ is the wavevector of the Stokes photon and $\omega = |\mathbf{k}|\mathrm{c}$ its frequency.

To model the interaction of the light fields with the atomic ensemble, we make use of the Hamiltonian [28]

$$H(t) = \sum_{i=1}^{N}\hat{\sigma}_{sg}^{i}\int d\mathbf{k}g_{\mathbf{k}}a^{\dagger}(\mathbf{k})\exp\left\{i\Delta\omega t\right\}u\left(\mathbf{r}_{\perp,i}\right)\xi\left(t\right)\exp\left\{-i\Delta\mathbf{k}\cdot\mathbf{r}_i\right\} + \mathrm{H.c.}, \tag{2.3}$$

where $\hat{\sigma}_{sg}^{i} = |s\rangle_i\langle g|$ is the transition operator for the ith atom, $\mathbf{r}_i = (x_i, y_i, z_i)$ is the vector position of the ith atom, $g_{\mathbf{k}}$ is the coupling coefficient of the transition, $\Delta\omega = \omega - (\omega_0 - \omega_{sg})$ and $\Delta\mathbf{k} = \mathbf{k} - k_0\hat{z}$, with ω_{sg} being the transition frequency between states $|g\rangle$ and $|s\rangle$.

For the initial conditions of the system, we assume that, before the interaction, all

the atoms are in the ground state and that there are no Stokes photons in the optical modes, so the initial state of the system reads

$$|\Psi\rangle_0 = |g_1...g_i...g_N\rangle \otimes |0\rangle_{\mathbf{k}}. \tag{2.4}$$

Then, considering that the pump field is weak enough, we can make use of first-order perturbation theory to write the state of the system as

$$|\Psi\rangle = |\Psi\rangle_0 - i\,\varepsilon\,(\Delta\omega) \sum_{i=1}^{N} \int d\mathbf{k}\,u\,(\mathbf{r}_{\perp,i}) \exp\{-i\Delta\mathbf{k} \cdot \mathbf{r}_i\}\,|g_1...s_i...g_N\rangle\,|\mathbf{k}\rangle, \tag{2.5}$$

where $\varepsilon(\Delta\omega) = \int_0^t dt'g\,\xi(t')\exp(i\Delta\omega t')$. In writing Eq. (2.5), we have assumed that $\Delta\mathbf{k}$ is independent of the frequency, $|\mathbf{k}| \simeq k_0$, and that the coupling is the same for all allowed directions of emission of the Stokes photons, $g_{\mathbf{k}} = g$.

Before we continue with the description of the model, it is important to remark that the use of first-order perturbation theory is motivated by the experiments in which a weak pump pulse and a short interaction time are used in order to guarantee that the probability of creating more than one excitation in the collective atomic state is very low [23, 25–27]. Therefore, the weak-pumping condition makes a perturbative approach suitable for describing a realistic situation.

Making use of Eq. (2.5), we can recover the cases presented in Refs. [28–31], namely the emission of Stokes photons from *cold* and *hot* atomic ensembles. In the former case, since the atoms are considered to be fixed in their positions, we can directly use Eq. (2.5) to find that the probability of emitting a photon in a given direction $\mathbf{k}$ is the same for all directions (i.e., there is no preferred direction of emission) independently of the specific shape of the atomic cloud. In contrast, in the latter case, due to the fact that during the light-matter interaction the atoms are moving fast, an average over all positions $\mathbf{r}_i$ should be performed [28, 36], so the state of the systems takes the form

$$|\Psi\rangle = |\Psi\rangle_0 - i\varepsilon\,(\Delta\omega) \int d\mathbf{k}\,F\,(\Delta\mathbf{k})\,|\mathbf{k}\rangle \otimes \sum_{i=1}^{N} |g_1...s_i...g_N\rangle\,, \tag{2.6}$$

where the average value over all positions is defined as

$$F\,(\Delta\mathbf{k}) = \int d\mathbf{r}u(\mathbf{r}_{\perp}) \exp\{-i\Delta\mathbf{k} \cdot \mathbf{r}\}\,\mathrm{P}_{\mathrm{dis}}(\mathbf{r}), \tag{2.7}$$

with $\mathrm{P}_{\mathrm{dis}}(\mathbf{r})$ being the atomic distribution function. Using Eq. (2.6), one can obtain that the Stokes photons are emitted in a small cone around the direction of the pump

(see Refs. [28, 29] for a detailed calculation), whose width depends on the particular spatial shape of the atomic cloud. Notice that, in this case, the photon and atomic degrees of freedom can be decoupled, and the quantum state of the atoms corresponds to the so-called symmetric collective atomic state, i.e., $|s_a\rangle = 1/\sqrt{N} \sum_1^N |g_1...s_i...g_N\rangle$.

Notice that the transition from the two limiting cases, cold and hot atomic ensembles, cannot be explored by means of Eq. (2.5), because it does not show any temperature dependence. However, we can model this dependence by introducing a new function describing the movement of each atom as a function of the ensemble's temperature. This new function writes

$$f\left(\mathbf{r}, \mathbf{r}_i\right) = \frac{1}{\pi^{3/2} A^3\left(T\right)} \exp\left[-\frac{|\mathbf{r} - \mathbf{r}_i|^2}{A^2\left(T\right)}\right], \tag{2.8}$$

where $\mathbf{r}_i$ is the mean position of the ith atom and the function $A\left(T\right) = \mathrm{v}_a \tau$ determines the radius of the area over which the atoms can move during the interaction time. It depends on the pump pulse duration τ, and on the speed $(\mathrm{v_a} = \sqrt{2K_B T/m})$ most likely to be possessed by any atom of the system. m is the mass of the atom, K_B is the Boltzmann constant and T is the temperature of the atomic ensemble. Notice that the origin of $\mathrm{v_a}$ lies in the Maxwell−Boltzmann distribution. This distribution is assumed, because it has been shown that the Maxwell-Boltzmann distribution provides an accurate description of the motion of atoms at temperatures above tenths of μK [32, 37]. Therefore, Eq. (2.8) is useful for describing the motion of atoms undergoing a transition from the hot to the cold condition, provided that the lowest temperature values are above tenths of μK.

By substituting Eq. (2.8) into Eq. (2.5), we find that the temperature-dependent quantum state of the system atoms-photon can be written as

$$\begin{aligned}
|\Psi\rangle = |\Psi\rangle_0 - i\varepsilon\left(\Delta\omega\right) \sum_{i=1}^{N} \int d\mathbf{k} \int_V d\mathbf{r} f\left(\mathbf{r}, \mathbf{r}_i\right) u\left(\mathbf{r}_\perp\right) \\
\times \exp\left\{-i\Delta\mathbf{k} \cdot \mathbf{r}\right\} |g_1...s_i...g_N\rangle |\mathbf{k}\rangle,
\end{aligned} \tag{2.9}$$

where V stands for the volume of the cloud. Notice that, in the limit where $A \to 0$ (cold atomic ensemble), the function given in Eq. (2.8) tends to a Dirac delta function, and we recover the state of the system described by Eq. (2.5).

To obtain the angular distribution of the emitted Stokes photons, we trace out the atomic variables of the density matrix of the system, i.e., $\rho = |\Psi\rangle \langle\Psi|$. Neglecting the

vacuum contribution, the reduced density matrix of the photon state writes

$$\rho_{\mathrm{s}} = \sum_{i=1}^{N} \int d\mathbf{k} d\mathbf{k}' S(\mathbf{r}_i, \mathbf{k}) S^*(\mathbf{r}_i, \mathbf{k}') |\mathbf{k}\rangle\langle\mathbf{k}'|, \tag{2.10}$$

where

$$S(\mathbf{r}_i, \mathbf{k}) = \int_V d\mathbf{r} f(\mathbf{r}, \mathbf{r}_i) u(\mathbf{r}_\perp) \exp\left(-i\Delta\mathbf{k} \cdot \mathbf{r}\right). \tag{2.11}$$

Considering that the atoms are contained in a cell with transversal dimensions L_x, L_y and length L_z, we can solve Eq. (2.11) to obtain

$$S(\mathbf{r}_i, \mathbf{k}) = \frac{1}{8}\alpha^2 \Phi(x_i, k_x)\Phi(y_i, k_y)\Omega(z_i, k_z), \tag{2.12}$$

where

$$\alpha = \left(\frac{r_0^2}{A^2 + r_0^2}\right)^{1/2}, \tag{2.13}$$

$$
\begin{aligned}
\Phi(x_i, k_x) =& \exp\left[-\frac{k_x^2 r_0^2}{4} - \left[\frac{\alpha}{r_0}\left(x_i + i\frac{r_0^2 k_x}{2}\right)\right]^2\right] \\
&\times \left\{\mathrm{erf}\left[-\frac{\alpha^3}{2}\left(2x_i - ik_x A^2 - \frac{L_x}{\alpha^2}\right)\right] \right. \\
&\left. - \mathrm{erf}\left[-\frac{\alpha^3}{2}\left(2x_i - ik_x A^2 + \frac{L_x}{\alpha^2}\right)\right]\right\},
\end{aligned}
\tag{2.14}
$$

$$
\begin{aligned}
\Omega(z_i, k_z) =& \exp\left[-\frac{k_z^2 A^2}{4} - ik_z z_j\right] \\
&\times \left\{\mathrm{erf}\left[-\frac{1}{2A}\left(2z_i - ik_z A^2 - L_z\right)\right] \right. \\
&\left. - \mathrm{erf}\left[-\frac{1}{2A}\left(2z_i - ik_z A^2 + L_z\right)\right]\right\}.
\end{aligned}
\tag{2.15}
$$

Notice that the presence of the error function [erf(x)] in Eqs. (2.14) and (2.15) is due to the integration over the finite volume V of the cell that contains the atoms.

Finally, we can find that the probability of emitting a Stokes photon in the direction $\mathbf{k}$ is given by the diagonal terms of the density matrix (2.10),

$$P(\mathbf{k}) = \sum_{i=1}^{N} |S(\mathbf{r}_i, \mathbf{k})|^2, \tag{2.16}$$

where the normalization condition writes $\sum_{i=1}^{N} \int d\mathbf{k} |S(\mathbf{r}_i, \mathbf{k})|^2 = 1$. In general, because
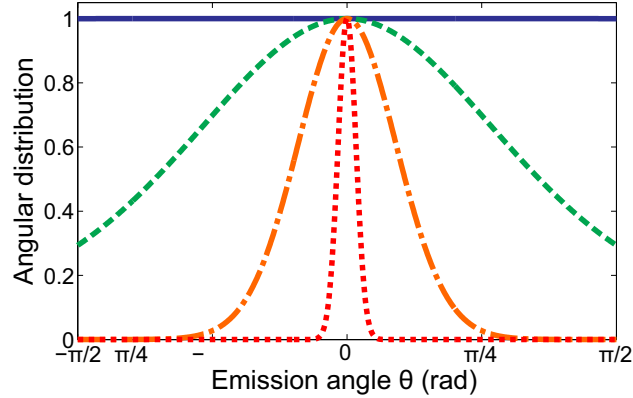
Fig. 2.2 Angular distribution of emitted Stokes photons for different temperatures of the atomic ensemble. Solid line: $T = 100$ μK; Dashed line: $T = 1$ K; Dash-dotted line: $T = 10$ K; Dotted line: $T = 300$ K. In all cases, the pump pulse duration is set to $\tau = 10$ ns.

the atomic cloud contains a large atom number density, the atomic summation can be rewritten as $\sum_{i=1}^{N} \rightarrow (N/V) \int dV$.

Notice that, in order to obtain the angular distribution of photons as a function of the temperature, equation (2.16) needs to be solved numerically due to the presence of the error function in Eqs. (2.14) and (2.15). However, since the functions of the spatial variables are separated [as can be seen from Eq. (2.12)], the numerical integration can be easily performed.

2.2 Angular distribution of emitted Stokes photons

We have computed the angular distribution of the emitted Stokes photons considering an ensemble of ^{87}Rb atoms contained in a pencil-shaped cell with transversal dimensions: $L_x = L_y = 2$ mm, and length $L_z = 30$ mm. The atoms are illuminated by a pump pulse with a transversal shape given by $u(\mathbf{r}_\perp) \sim \exp\left\{-(x^2 + y^2)/r_0^2\right\}$, where $r_0 = 2$ mm is the beam waist of the pump beam. The level configuration of the atoms is set to $5^2P_{1/2}$ for the excited level $|e\rangle$, and the Zeeman-splitting levels $5^2S_{1/2}\,(F = 1)$ and $5^2S_{1/2}\,(F = 2)$ for the $|g\rangle$ and $|s\rangle$ states, respectively.

Figure 2.2 shows the angular distribution (normalized to the maximum) of emitted Stokes photons as a function of the angle θ between the direction of the pump and the emitted photon [as shown in Fig. 2.3(a)]. In the low temperature limit, the

spontaneous emission of Stokes photons has no preferred direction. This result agrees with Ref. [23], in which Stokes photons are said to be emitted into 4π steradian. In contrast, as the temperature of the cloud is increased, the probability distribution narrows around $\theta = 0$, showing that in the case of warm atomic ensembles, Stokes photons are emitted preferentially along the direction of the pump, as it has been experimentally observed, for instance, in Ref. [22].

The results presented in Fig. (2.2) can be understood in terms of the *which-way* information left in the atoms after emitting a Stokes photon, i.e., the information about the position of the atom that emitted the photon. In the case of cold atomic ensembles, the fact that atoms are fixed would allow us, in principle, to obtain information about the position of the atom that emitted the photon. In this situation, the possible paths of the Stokes photon will not interfere, because which-way information has been left in the ensemble. This can be clearly seen from Eq. (2.16), which for cold atomic clouds takes the form

$$P_{\text{cold}}(\mathbf{k}) = \sum_{i=1}^{N} |u\left(\mathbf{r}_{\perp,i}\right)|^2 . \tag{2.17}$$

Equation (2.17) shows that emission of Stokes photons from a cold atomic ensemble has no preferred direction. Moreover, notice that it describes a sum of the squared amplitudes of the fields, which is a footprint of an incoherent sum, where interference effects are not present.

In the case of hot atomic ensembles, one can easily show that Eq. (2.8) is a constant within the integration volume, so we can write Eq. (2.16), assuming a large atom number density, as

$$P_{\text{hot}}(\mathbf{k}) = \left| \sum_{i=1}^{N} u\left(\mathbf{r}_{\perp,i}\right) e^{-i\Delta \mathbf{k} \cdot \mathbf{r}_i} \right|^2 . \tag{2.18}$$

We can observe from Eq. (2.18) that interference between possible paths of the Stokes photon is now restored, because which-way information has been erased by the movement of the atoms in the cloud. Interestingly, this which-way information effect has also been observed, for instance, in the context of second-order interference of single photons [38].

It is important to highlight that the results presented here show that whether interference effects are present does not depend on the actual acquisition of information from the system, but on the possibility to obtain such information. This fundamental relationship between interference and indistinguishability has been pointed out, for

(a)

(b)
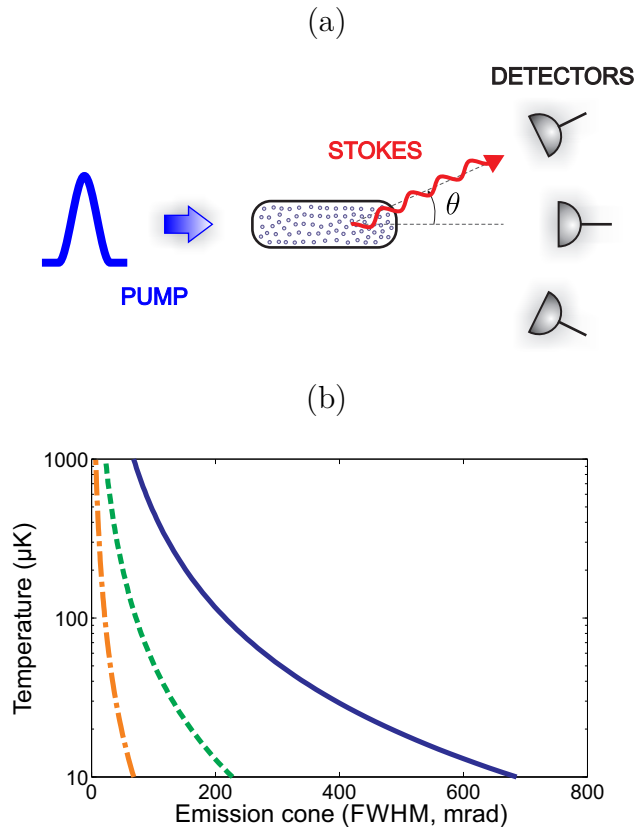
Fig. 2.3 (a) Proposed experimental setup: an array of detectors is used to measure the width of Stokes emission cone in order to determine the temperature of the atomic ensemble. (b) Temperature of the atomic cloud as a function of the full width at half maximum of the emission cone, considering different pulse durations. Solid line: $\tau = 10 \ \mu$s; Dashed line: $\tau = 30 \ \mu$s; Dash-dotted line: $\tau = 100 \ \mu$s.

instance, in Ref. [39].

2.3 Experimental proposal

The close relationship between the width of the Stokes emission cone and the temperature of the atomic ensemble allows us to introduce a new technique for measuring the temperature of atomic clouds. The proposed experimental scheme consists of an array of detectors (or a movable detector) that would be able to detect Stokes photons along different directions, as shown in Fig. 2.3(a). In this way, by measuring the width of the emission cone, we could use Eq. (2.16) to retrieve information about the temperature of the atomic ensemble. To exemplify how the proposed technique would

perform, Fig. 2.3(b) shows the temperature of the atomic ensemble as a function of the full width at half maximum (FWHM) of the emission cone. Notice that, by selecting a sufficiently short pulse, the dependence of the emission cone on the temperature of the ensemble gets smoother. This can be useful for a better discrimination of the width of the emission cone, enhancing thus the precision of the technique. Also, notice that the proposed experimental scheme is not based on the ballistic expansion of the atomic cloud [32], so each measurement can be performed without destroying it.

2.4 Heralded generation of the symmetric atomic state

Another important feature of Eq. (2.9) is that it can also be used to describe how the generation of the symmetric collective atomic state depends on the temperature of the atomic cloud. When a Stokes photon is detected in an arbitrary direction $\mathbf{k}$, i.e., is projected into the state $|\mathbf{k}\rangle$, the corresponding quantum state of the atomic cloud is

$$|\Psi\rangle_a = \sum_{i=1}^{N} S\left(\mathbf{r}_i, \mathbf{k}\right) |g_1...s_i...g_N\rangle. \tag{2.19}$$

The projection of Eq. (2.19) on the symmetric state $|s_a\rangle$ can then be used to find the probability of generating a symmetric state in the atomic ensemble. In the cold atoms case, although Stokes photons are emitted in a larger emission cone, only a small fraction of them (those in a small angle around the pump beam) correspond to the symmetric state [see Figs. 2.4(a,b)]. In contrast, when the temperature of the cloud is increased, which-way information is erased and the emission cone gets narrower [Fig. 2.4(g)]. In this case, as it can be seen from Fig. 2.4(h), photons emitted in all allowed possible directions are in the symmetric state. Notwithstanding, if we want to enhance the flux of detected Stokes photons, we are again forced to detect them in small emission angles around the pump beam. Therefore, in all cases, one needs to detect the Stokes photons in a small cone around the direction of propagation of the pump beam, if the goal is to generate the symmetric collective atomic state. But, as Fig. 2.4 shows, the reason behind this restriction depends on the temperature of the atomic ensemble.

(a)

(b)

(c)

(d)

(e)

(f)

(g)

(h)
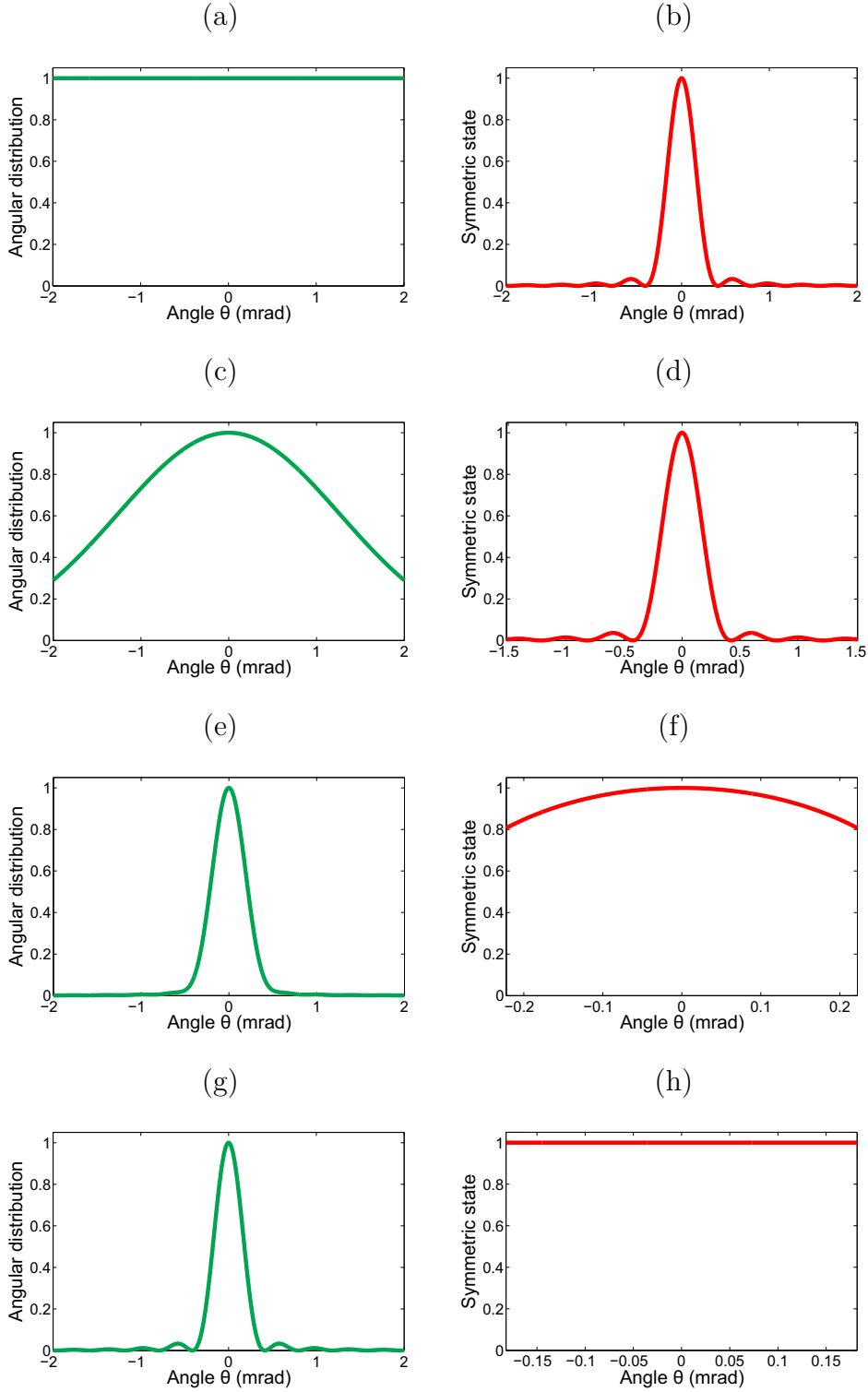
Fig. 2.4 Angular distribution of the emitted Stokes photons [(a),(c),(e) and (g)], and the weight of the symmetric atomic state $|\langle s_a|\Psi\rangle_a|^2$ (within the FWHM of the emission cone) [(b), (d), (f) and (h)] for different radius of the region where atoms are let to move: (a,b) A=1 μm, (c,d) A=100 μm, (e,f) A=1 mm, and (g,h) A=100 mm. Pulse duration: 10 μs.

Conclusions

In this chapter, we have described the relationship that exists between the temperature of an atomic ensemble and the width of the emission cone of spontaneously emitted Stokes photons. Using this fundamental result, we have presented a new nondestructive technique for measuring the temperature of atomic clouds. Furthermore, we have shown that heralded generation of the collective symmetric atomic state requires the detection of the heralding Stokes photon in a narrow cone around the direction of the exciting pulse. For cold atomic clouds, this is the only direction that guarantees the generation of such state, whereas for hot atomic ensembles, it is the direction with the highest efficiency.

Role of entanglement in two-photon virtual-state spectroscopy

The two-photon absorption (TPA) process has played a fundamental role in the development of new technologies aimed at probing the structure of atoms and molecules, such as two-photon microscopy [40] and two-photon spectroscopy [41]. In particular, nonlinear two-photon spectroscopy has become an invaluable tool [42], where the capability of TPA is exploited to obtain information about a sample that would not be accessible otherwise.

With the appearance of new light sources capable of generating entangled photon pairs [43], new phenomena in TPA processes have been observed. Indeed, the linear dependence of the TPA rate on the photon flux [44], two-photon induced transparency [45], virtual-state spectroscopy [46, 47] and the selectivity of double-exciton states of chromophore aggregates [48] are effects that have been attributed to the presence of entanglement between the photons that participate in the TPA process. However, in some cases, the link between entanglement and the new effect is sometimes blurred. Thus, one can always wonder whether such effects are due to a particular feature of the photons that might be unrelated to their entangled nature. This is the case of certain phenomena that, when first described, were attributed to the existence of entanglement between pairs of photons. For instance, Nasr *et al.* [49] demonstrated a new scheme, based on entanglement, to enhance the resolution of an optical coherence tomography system by erasing the effects due to second-order chromatic dispersion. Later, the work in Ref. [50] showed that by properly introducing a phase conjugator

element in the optical coherence tomography scheme, which produces a Gaussian-state light source with frequency anti-correlation, a similar effect could be achieved. In dispersion cancelation, an effect that is observed in the temporal domain, namely the broadening of the second-order correlation function of paired photons propagating in two different optical fibers, it was shown that it could be suppressed, provided that the group velocity dispersion parameters of both fibers were identical but opposite in sign, and that the photons were entangled [51–53]. However, it has been recently demonstrated that such effects could also be produced by frequency-correlated photons, which nonetheless might be non-entangled [54, 55].

Remote temporal modulation [56, 57], an effect similar to dispersion cancelation, but observed in the frequency domain, describes the appearance of new frequency correlations when entangled paired photons are synchronously driven by two temporal modulators. In a similar manner to dispersion cancelation, if the two identical modulators are driven in opposite phases, their global effect is to negate each other, and the spectral correlations appear as those when no phase modulators are present. Again, it has been shown [55] that entanglement is not a requisite, and that the same effect can be observed using non-entangled optical beams bearing certain frequency correlations. All these examples illustrate the fact that the presence of entanglement is not the key enabling factor that allows the observation of dispersion cancelation and remote temporal modulation, but the existence of certain frequency correlations, a characteristic that takes place along the presence of entanglement, but it can also manifest without it.

In this chapter, we study one important spectroscopic application whose capabilities have been associated with the use of entangled photon pairs, namely two-photon virtual-state spectroscopy. The importance of this technique resides in the fact that, unlike commonly used two-photon absorption spectroscopy techniques, where pulsed and tunable sources are required, it is implemented by carrying out continuous-wave absorption measurements without changing the wavelength of the source [46, 47]. Unfortunately, this technique has not been broadly applied because the ease with which it can be performed is limited by the low efficiency photon generation in nonlinear crystals. However, with the advent of ultrahigh flux sources of entangled photons [58], this technique may open new research directions towards ultrasensitive detection in chemical and biological systems [59, 60].

To unveil the true role of entanglement in virtual-state spectroscopy, we make use of two ingredients. Firstly, we apply a full quantum formalism to the two-photon

state, so we can clearly identify the amount of entanglement existing between the photons. Secondly, we consider a general form of the two-photon state, which allows us to explore different types of correlations and spectral shapes of the photons. Using these ingredients, we show that the presence of entanglement does not guarantee the successful retrieval of spectroscopic information of the medium. In fact, it is the combination of entanglement and a specific shape of the frequency correlations between photons what makes the realization of two photon virtual-state spectroscopy possible.

This chapter is organized as follows. Section 3.1 provides the most general expression of the TPA transition probability for an arbitrary initial two-photon state. Then, by using this result, we compute the TPA transition probability for uncorrelated classical pulses, classical frequency-correlated photons, and quantum frequency-correlated (entangled) photons in Sections 3.2, 3.3 and 3.4, respectively.

3.1 Light-matter interaction

Let us consider the scenario where two photons are absorbed by an atom or a molecule inducing a transition between two of its energy levels that match the overall energy of the incident photons. Using a quantum mechanical approach, one can find that the probability that the atom or molecule undergoes a two-photon transition is given by a weighted sum of many energy non-conserving atomic transitions (virtual-state transitions) [61, 62] between its energy levels (see below). Even though it has been shown that information about these virtual-state transitions, a signature of the medium, can be extracted by Fourier transforming the TPA transition probability of mutually delayed entangled photons [46], one cannot avoid to wonder: Can we retrieve the sought-after information (energy level structure) with any type of frequency correlations between the photons? To address this question, we proceed as follows.

The interaction of a medium (atom or molecule) with a two-photon optical field $|\Psi\rangle$ can be described by the interaction Hamiltonian

$$H_I(t) = d(t) E^{(+)}(t), \tag{3.1}$$

where $d(t)$ is the dipole-moment operator and $E^{(+)}(t)$ is the positive-frequency part of the electric-field operator, which reads as $E^{(+)}(t) = E_1^{(+)}(t) + E_2^{(+)}(t)$. The electric

field operators $E_1^{(+)}(t)$ and $E_2^{(+)}(t)$ can be written as

$$E_j^{(+)}(t) = \int d\omega_j \sqrt{\frac{\hbar\omega_j}{4\pi\epsilon_0 cA}} a(\omega_j) \exp(-i\omega_j t), \tag{3.2}$$

where c is the speed of light, ϵ_0 is the vacuum permittivity, A is the effective area of the field, and $a(\omega_j)$ is the annihilation operator of a photonic frequency-mode, with frequency ω_j, bearing a specific spatial shape and polarization that, for the sake of simplicity, are not explicitly written.

The medium is initially in its ground state $|g\rangle$ (with energy ε_g). The probability that the medium is excited to the final state $|f\rangle$ (with energy ε_f), through a two-photon absorption process, is given by second-order time-dependent perturbation theory as [63]

$$P_{g\to f} = \left| \frac{1}{\hbar^2} \int_{-\infty}^{\infty} dt_2 \int_{-\infty}^{t_2} dt_1 M_d(t_1, t_2) M_E(t_1, t_2) \right|^2, \tag{3.3}$$

with

$$M_d(t_1, t_2) = \langle f| d(t_2) d(t_1) |g\rangle, \tag{3.4}$$

$$M_E(t_1, t_2) = \langle \Psi_f| E^{(+)}(t_2) E^{(+)}(t_1) |\Psi\rangle, \tag{3.5}$$

where $|\Psi_f\rangle$ denotes the final state of the optical field.

Equation (3.4) can be expanded in terms of virtual-state transitions to obtain

$$M_d(t_1, t_2) = \sum_{j=1} D^{(j)} \exp\left[-i(\varepsilon_j - i\kappa_j/2 - \varepsilon_f)t_2\right] \exp\left[-i(\varepsilon_g - \varepsilon_j + i\kappa_j/2)t_1\right], \tag{3.6}$$

where $D^{(j)} = \langle f| d |j\rangle \langle j| d |g\rangle$ are the transition matrix elements of the dipole-moment operator. We can see from Eq. (3.6) that excitation of the medium occurs through intermediate states $|j\rangle$, with complex energy eigenvalues $\varepsilon_j - i\kappa_j/2$, where κ_j stands for the natural linewidth of the intermediate states [64]. Also, we can write Eq. (3.5) as

$$M_E(t_1, t_2) = \langle \psi_f| E_2^{(+)}(t_2) E_1^{(+)}(t_1) |\psi_i\rangle + \langle \psi_f| E_1^{(+)}(t_2) E_2^{(+)}(t_1) |\psi_i\rangle, \tag{3.7}$$

where we have kept the terms in which only one photon from each field contributes to the overall two-photon excitation. The first term of Eq. (3.7) corresponds to the case in which the photon field $E_1^{(+)}(t)$ interacts first, and $E_2^{(+)}(t)$ interacts later. The remaining term describes the complementary case.

Because we are interested in a process in which the optical field that interacts with the medium is composed by only two photons, we consider the initial state of the field as an arbitrary two-photon state given by [65]

$$|\Psi\rangle = \int d\nu_{\mathrm{s}}d\nu_{\mathrm{i}}\Phi\left(\nu_{\mathrm{s}},\nu_{\mathrm{i}}\right)a_{\mathrm{s}}^{\dagger}\left(\nu_{\mathrm{s}}+\omega_{\mathrm{s}}^{0}\right)a_{\mathrm{i}}^{\dagger}\left(\nu_{\mathrm{i}}+\omega_{\mathrm{i}}^{0}\right)|0\rangle, \tag{3.8}$$

where "s" and "i" stand for the signal and idler photonic modes, $\nu_j = \omega_j - \omega_j^0$ $(j = \mathrm{s,i})$ are the frequency deviations from the central frequencies ω_j^0, and $\Phi\left(\nu_{\mathrm{s}},\nu_{\mathrm{i}}\right)$ is the joint spectral amplitude, or mode function, which fully describes the correlations and bandwidth of the two-photon state.

To quantify the degree of entanglement between the absorbed photons, we will make use of the entropy of entanglement, which is defined as [66]

$$\mathrm{S} = -\sum_{j}\lambda_j\mathrm{log}_2\lambda_j, \tag{3.9}$$

where λ_j are the eigenvalues of the Schmidt decomposition of the joint spectral amplitude, i.e., $\Phi\left(\nu_{\mathrm{s}},\nu_{\mathrm{i}}\right) = \sum_j \lambda_j^{1/2}f_j(\nu_{\mathrm{s}})g_j(\nu_{\mathrm{i}})$, with $f_j(\nu_{\mathrm{s}})$ and $g_j(\nu_{\mathrm{i}})$ corresponding to the Schmidt modes. It is worth remarking that the lack of entanglement between the pair of photons is characterized by a value of the entropy equal to zero.

In what follows, with the aim of recognizing in which situations virtual-state spectroscopy can be performed, we will compute the TPA transition probability of atomic hydrogen using different types of initial two-photon states. We have selected atomic hydrogen as model system, because it has been used in previous studies of virtual-state spectroscopy [46, 63] and it has been the subject of several one- and two-photon absorption experiments [67–70]. In our calculations, we will focus on the $1s \rightarrow 2s$ two-photon transition. Due to quantum number selection rules [69], this transition takes place via intermediate p states: $1s \rightarrow \{2p, 3p, ..., np\} \rightarrow 2s$, which are coupled to the s states by real-valued transition matrix elements. The hydrogen atom energy levels are $\varepsilon_n = -13.6/n^2$ eV $(n = 1, 2, 3, ...)$ and the natural linewidths of intermediate states κ_j are taken from Refs. [67, 69]. We will assume the condition $\varepsilon_f - \varepsilon_g = \omega_s^0 + \omega_i^0$, and that the final state $2s$ is Lorentzian broadened with a radiative lifetime $1/\kappa_f = 122$ ms [68], which is introduced in the model by averaging the TPA transition probability over a Lorentzian function of width κ_f [64].

3.2 TPA transition probability with uncorrelated classical pulses

We first consider the case in which the medium is illuminated by uncorrelated classical light. This case has been presented in Ref. [71], where it has been pointed out that spectroscopic information resident in the TPA signal is essentially the same, regardless of the existence of correlations between the absorbed photons.

To investigate virtual-state spectroscopy by means of uncorrelated light, we will assume that the two absorbed photons are embedded into rectangular-shaped pulses of the same duration $T_{\rm p}$, with a tunable time delay τ between them. This initial optical field can be represented by an uncorrelated two-photon state described by the normalized mode function

$$\Phi\left(\nu_{\rm s}, \nu_{\rm i}\right) = \frac{T_{\rm p}}{2\pi} \text{sinc}\left(T_{\rm p}\nu_{\rm s}/2\right) \text{sinc}\left(T_{\rm p}\nu_{\rm i}/2\right) \exp\left[i\left(\nu_{\rm s} - \nu_{\rm i}\right)\tau/2\right]. \tag{3.10}$$

With the state given by Eq. (3.10), and making use of Eqs. (3.3), (3.6) and (3.7), we can write the TPA transition probability as

$$P_{g\to f}\left(T_{\rm p}; \tau\right) = \frac{\omega_0^2}{\hbar^2 \epsilon_0^2 {\rm c}^2 A^2 T_{\rm p}^2} \left| \sum_j D^{(j)} \left[I_1 + I_2\right] \right|^2, \tag{3.11}$$

where

$$I_1 = \frac{\sin\left[\Delta\omega\left(T_{\rm p} - \tau\right)/2\right]}{\Delta_g \Delta\omega} - \frac{\sin\left[\Delta_f\left(T_{\rm p} - \tau\right)/2\right] \exp\left[i\Delta_g\left(T_{\rm p} + \tau\right)/2\right]}{\Delta_g \Delta_f}$$
$$- \frac{2i\sin\left(\Delta_g T_{\rm p}/2\right) \sin\left(\Delta_f \tau/2\right) \exp\left[-i\left(\Delta_f T_{\rm p} - \Delta_g \tau\right)/2\right]}{\Delta_g \Delta_f}, \tag{3.12}$$

$$I_2 = \frac{\sin\left[\Delta\omega\left(T_{\rm p} - \tau\right)/2\right]}{\Delta_g \Delta\omega} - \frac{\sin\left[\Delta_f\left(T_{\rm p} - \tau\right)/2\right] \exp\left[i\Delta_g\left(T_{\rm p} - \tau\right)/2\right]}{\Delta_g \Delta_f}, \tag{3.13}$$

with $\Delta_f = \varepsilon_j - i\kappa_j/2 - \varepsilon_f + \omega_0$, $\Delta_g = \varepsilon_g - \varepsilon_j + i\kappa_j/2 + \omega_0$, and $\Delta\omega = \varepsilon_g - \varepsilon_f + 2\omega_0$. For the sake of simplicity, in writing Eq. (3.11), we have assumed the condition $\omega_{\rm i}^0 = \omega_{\rm s}^0 = \omega_0$.

We have computed the TPA transition probability for different values of $T_{\rm p}$ and τ and, in all cases, it turned out to be a constant as a function of the delay τ between the pulses, when $\tau < T_{\rm p}$, which implies that a Fourier analysis with respect to τ would result in only one peak centered at zero frequency, meaning that spectroscopic information about intermediate levels of the medium is not present in the TPA signal.

Therefore, based on these results, we can conclude that when frequency correlations between the photons are not present, spectroscopic information about energy levels is not available. This implies that virtual-state spectroscopy cannot be performed by means of two delayed rectangular-shaped classical pulses, which is in contradiction with the results presented in section VI of Ref. [71].[1]

3.3 TPA transition probability with classically correlated photons

We now explore the case in which the two absorbed photons are frequency correlated but they are nonetheless non-entangled. To this end, we make use of the theory presented by Mollow in Ref. [64] to rewrite the TPA transition probability [Eq. (3.3)] as

$$P_{g \to f} = \frac{1}{\hbar^4} \int_{-\infty}^{\infty} dt'_2 dt'_1 dt_2 dt_1 \mathcal{L}^*(t'_2, t'_1) G^{(2)}(t'_2, t'_1; t_2, t_1) \mathcal{L}(t_2, t_1), \quad (3.14)$$

where $\mathcal{L}(t_2, t_1) = \Theta(t_2 - t_1) M_d(t_1, t_2)$, with $\Theta(t)$ being the Heaviside step function. Here, $G^{(2)}$ corresponds to the second-order field correlation function, which is defined in terms of the density operator ρ of the optical field as

$$\begin{aligned}
G^{(2)}(t'_2, t'_1; t_2, t_1) = &\operatorname{Tr}\left[\rho E_2^{(-)}(t'_2) E_1^{(-)}(t'_1) E_1^{(+)}(t_2) E_2^{(+)}(t_1)\right] \\
&+ \operatorname{Tr}\left[\rho E_2^{(-)}(t'_2) E_1^{(-)}(t'_1) E_2^{(+)}(t_2) E_1^{(+)}(t_1)\right] \\
&+ \operatorname{Tr}\left[\rho E_1^{(-)}(t'_2) E_2^{(-)}(t'_1) E_1^{(+)}(t_2) E_2^{(+)}(t_1)\right] \\
&+ \operatorname{Tr}\left[\rho E_1^{(-)}(t'_2) E_2^{(-)}(t'_1) E_2^{(+)}(t_2) E_1^{(+)}(t_1)\right],
\end{aligned} \quad (3.15)$$

where $\operatorname{Tr}[...]$ stands for the trace over the field states.

To compute the second-order correlation function, we consider a classically correlated two-photon state described by a density operator of the form

$$\rho = \int d\nu \, |\Phi(\nu, -\nu)|^2 \, |\omega^0 + \nu\rangle_1 |\omega^0 - \nu\rangle_2 \langle \omega^0 + \nu|_1 \langle \omega^0 - \nu|_2, \quad (3.16)$$

with ω^0 being the central frequency of the photons and $\Phi(\nu, -\nu)$ the mode function that describes the frequency correlations between them.

---

[1]The origin of this contradiction lies in the use, in Ref. [71], of a wrong identity for multiplication of rectangular functions. This identity creates correlations between the fields, which ultimately lead to non-monotonic behavior of the TPA transition probability.

By using Eq. (3.16), we find that the second-order correlation function of the classically correlated photons is given by

$$
\begin{aligned}
G^2(t_2', t_1'; t_2, t_1) = {} & \left(\frac{\hbar\omega^0}{2\pi\epsilon_0 cA}\right)^2 \exp[i\omega^0(t_2' + t_1' - t_2 - t_1)] \\
& \times \int d\nu \, |\Phi(\nu, -\nu)|^2 \cos\left[\nu(t_2 - t_1)\right] \cos[\nu(t_2' - t_1')].
\end{aligned}
\tag{3.17}
$$

Notice that the presence of the norm of the mode function cancels out any phase difference introduced by the delay τ [see Eqs. (3.10), (3.18) and (3.21)], which results in a TPA transition probability that does not depend on the delay between the photons. Therefore, we can conclude that when using non-entangled frequency-correlated photons, spectroscopic information about intermediate energy levels of the medium is not available in the TPA signal.

3.4 TPA transition probability with entangled photons

In light of the results presented so far, and the ideas and calculations originally introduced in Ref. [46], one cannot help to ask whether the presence of frequency entanglement between photons is the key ingredient that allows us to access information about the energy level structure of an arbitrary medium. In the following, we will compute the TPA transition probability using entangled photons bearing different spectral shapes to demonstrate that the presence of entanglement does not guarantee the successful retrieval of spectroscopic information of the medium. Rather, it is the use of a specific spectral shape of existing frequency correlations what makes the realization of two-photon virtual-state spectroscopy possible.

3.4.1 Two-photon state with a Gaussian spectral shape

In general, a two-photon state with tunable frequency correlations can be generated by means of type-II spontaneous parametric down-conversion (SPDC). In this process, two photons with orthogonal polarizations (signal and idler) are created by illuminating a second-order nonlinear crystal (of length L) with a Gaussian pulse, with temporal duration T_+ and frequency ω_{p}. To make the generated photons indistinguishable, after the crystal, the signal and idler interchange their polarization and traverse a similar

Fig. 3.1 Joint spectrum of the two-photon state for different values of T_-: (a) $T_- = 2$ ps, (b) $T_- = 20$ ps, and (c) $T_- = 200$ ps. (d) Entropy of entanglement as a function of T_- for Gaussian (red solid line) and sine cardinal (blue dashed line) shapes of the mode function. In all cases, the pump pulse duration is: $T_+ = 10$ ps.

crystal of length $L/2$. Finally, after the addition of a tunable delay τ between the photons, and restricting their spectrum using a Gaussian filter, the normalized mode function of the generated two-photon state is described by

$$
\begin{aligned}
\Phi\left(\nu_{\mathrm{s}}, \nu_{\mathrm{i}}\right) = \left(\frac{T_- T_+}{\sqrt{2\pi}}\right)^{1/2} \exp\left[-T_+^2\left(\nu_{\mathrm{i}} + \nu_{\mathrm{s}}\right)^2\right] \exp\left[-T_-^2\left(\nu_{\mathrm{s}} - \nu_{\mathrm{i}}\right)^2 / 4\right] \\
\times \exp\left[iLN_{\mathrm{p}}\left(\nu_{\mathrm{s}} + \nu_{\mathrm{i}}\right)/2 + i\nu_{\mathrm{i}}\tau\right],
\end{aligned}
\tag{3.18}
$$

where $T_- = \left(N_{\mathrm{s}} - N_{\mathrm{i}}\right)L/2$, with N_j $(j = \mathrm{i}, \mathrm{s}, \mathrm{p})$ being the inverse group velocities of the idler, signal and pump photons, respectively. In writing Eq. (3.18), we have made use of the group velocity matching condition [72]: $N_{\mathrm{p}} = \left(N_{\mathrm{i}} + N_{\mathrm{s}}\right)/2$, which ease the tuning of the frequency correlations between the photons [73].

31

The frequency correlation of down-converted photons can be tuned by properly selecting the values of T_+ and T_-. Figures 3.1(a)-(c) show the joint probability distribution of the two-photon state: $S\left(\nu_{\rm s}, \nu_{\rm i}\right) = \left|\Phi\left(\nu_{\rm s}, \nu_{\rm i}\right)\right|^2$, which measures the probability of detecting a signal photon of frequency $\omega_{\rm s}^0 + \nu_{\rm s}$ in coincidence with an idler photon of frequency $\omega_{\rm i}^0 + \nu_{\rm i}$. Notice that frequency anti-correlated photons [Fig. 3.1(a)] are obtained when $T_+ \gg T_-$, whereas for $T_+ \ll T_-$ we obtain frequency-correlated photons [Fig. 3.1(c)]. Interestingly, when $T_- = 2T_+$, one can generate a pair of uncorrelated photons [as depicted in Fig. 3.1(b)]. Figure 3.1(d) (red solid line) shows the dependence of the entropy of entanglement with T_- for a fixed value of T_+, considering a mode function of the form given by Eq. (3.18).

We can make use of the state described by Eq. (3.18) to find that the TPA transition probability for a two-photon state bearing a Gaussian spectral shape is given by

$$P_{g\to f}\left(T_-, T_+; \tau\right) = \frac{32\pi\omega_0^2}{\hbar^2\epsilon_0^2{\rm c}^2 A^2}T_+T_- \exp\left[-2T_+^2\left(\varepsilon_g - \varepsilon_f + \omega_{\rm p}\right)^2\right]$$

$$\times \left|\sum_j D^{(j)}\left\{F_+\left[\eta^{(j)}T_-; \tau\right]\exp\left[-i\eta^{(j)}\tau\right] + F_-\left[\eta^{(j)}T_-; \tau\right]\exp\left[i\eta^{(j)}\tau\right]\right\}\right|^2, \quad (3.19)$$

where $\eta^{(j)} = \Delta^{(j)} - i\kappa_j/2$, with the energy mismatch given by $\Delta^{(j)} = \varepsilon_j - \varepsilon_g - \omega_0$, and $F\left(\xi; \tau\right)$ is the plasma dispersion function [74], which is defined as

$$F_\pm\left(\xi; \tau\right) = \exp\left(-\xi^2\right)\left[1 - \frac{2i}{\sqrt{\pi}}\int_0^{\xi \pm \frac{i\tau}{2T_-}}\exp\left(y^2\right)dy\right]. \quad (3.20)$$

We have calculated the TPA transition probability as a function of the delay between the photons using two-photon states bearing different types of frequency correlations. In particular, we have computed Eq. (3.19) for uncorrelated and anti-correlated pairs of photons. As previously obtained, in the case of uncorrelated photons, the TPA signal is constant with the delay τ, so no spectroscopic information about intermediate energy levels is available.

Surprisingly, when considering anti-correlated photons, the TPA transition probability is also constant with the delay τ, which means that information about the energy level structure of the medium cannot be retrieved from the TPA signal either. This result demonstrates that the use of a source of paired photons with a high degree of entanglement does not guarantee the successful implementation of two-photon virtual-state spectroscopy. Therefore, we need to consider another property of the two-photon

state that is necessary to perform such technique, namely a specific spectral shape of the frequency correlations.

3.4.2 Two-photon state with a sine cardinal spectral shape

We now consider two-photon states bearing a sine cardinal spectral shape. The important feature of such states is that they are naturally harvested in the SPDC process, unlike states bearing a Gaussian spectral shape, which require a strong filtering of the pair of photons [75].

As in the previous section, we consider a type-II SPDC process where an additional nonlinear crystal of length $L/2$ is used to achieve indistinguishability of the photons. Then, by introducing a tunable delay τ between the photons, and without restricting their spectrum, the normalized mode function of the two-photon state can be written as

$$
\Phi\left(\nu_s, \nu_i\right) = \left(\frac{T_- T_+}{2\pi\sqrt{2\pi}}\right)^{1/2} \exp\left[-T_+^2\left(\nu_i + \nu_s\right)^2\right] \mathrm{sinc}\left[T_-\left(\nu_s - \nu_i\right)/2\right] \\
\times \exp\left[iLN_p\left(\nu_s + \nu_i\right)/2 + i\nu_i\tau\right].
\tag{3.21}
$$

The entropy of entanglement of the two-photon described by Eq. (3.21) is shown in Fig. 3.1(d) (blue dashed line). Notice that in this case, due to the presence of the sine cardinal function, only quasi-uncorrelated photons can be generated in the SPDC process.

Now, by using Eq. (3.21), we can find that the TPA transition probability for a two-photon state bearing a sine cardinal spectral shape is given by

$$
P_{g\to f}\left(T_-, T_+; \tau\right) = \frac{64\pi\omega_0^2}{\hbar^2\epsilon_0^2 c^2 A^2 T_-}\left[\frac{\sqrt{2}T_+}{\sqrt{\pi}}\exp\left[-2T_+^2\left(\varepsilon_g - \varepsilon_f + \omega_p\right)^2\right]\right] \\
\times \left|\sum_j A^{(j)}\left\{2 - \exp\left[-i\eta^{(j)}\left(T_- - \tau\right)\right] - \exp\left[-i\eta^{(j)}\left(T_- + \tau\right)\right]\right\}\right|^2,
\tag{3.22}
$$

where $A^{(j)} = D^{(j)}/\eta^{(j)}$.

Figure 3.2 shows the TPA transition probability as a function of the delay between the pulses. Notice that the TPA transition probability shows a non-monotonic behavior when considering an anti-correlated two-photon state. This means that spectroscopic information is contained within the TPA signal, which might be related to the energy level structure of the medium.
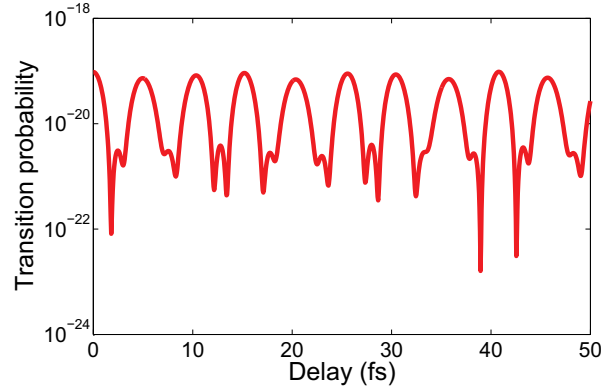
Fig. 3.2 Transition probability as a function of the delay τ for anti-correlated photons ($T_- = 2$ ps). Pump pulse duration: $T_+ = 10$ ps. Y-axis is set to a logarithmic scale.

In order to retrieve the information contained in the TPA signal, we follow Ref. [46] and perform an average of Eq. (3.22) over a range of values of T_- to obtain the weighted-and-averaged TPA transition probability

$$\bar{P}\left(\tau\right) = \frac{1}{T} \int_{T_-^{\min}}^{T_-^{\max}} P_{g\to f}\left(T_-, T_+; \tau\right) T_- dT_-, \qquad (3.23)$$

where $T = T_-^{\max} - T_-^{\min}$.

To experimentally perform the average in Eq. (3.23), a set of experiments with different values of T_- is needed. The parameter T_- can be tuned over a relatively broad range by means of different methods, depending on the system's configuration. For instance, in type-I SPDC (parallel-polarized photons), by changing the width of the pump beam the value of T_- can be modified [76]. Alternatively, in type-II SPDC, T_- is linearly proportional to the crystal length [77], so a proper set of wedge-shaped nonlinear crystals might be used.

To retrieve the spectroscopic information contained in the TPA signal, we perform a straightforward Fourier analysis of Eq. (3.23), provided that the condition $T \gg 1/\left|\Delta^{(j)} - \Delta^{(k)}\right|$ is satisfied. This condition needs to be fulfilled in order to eliminate unwanted terms at intermediate frequencies [46]. Figure 3.3 shows the result of Fourier transforming the weighted-and-averaged TPA transition probability. We can observe peaks located at the energy mismatch values: 5.1, 6.98, 7.65, 7.95, and 8.12 eV. Using these values, and the definition of energy mismatch, we obtain the virtual-state energy values: -3.40, -1.51, -0.85, -0.54, and -0.37 eV, which can be readily identified
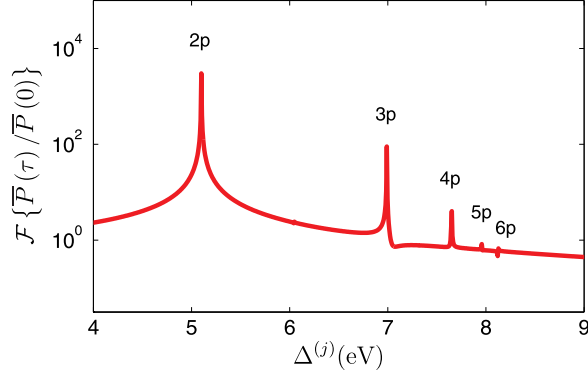
Fig. 3.3 Fourier transform of the normalized weighted-and-averaged TPA transition probability as a function of the energy mismatch $\Delta^{(j)}$. The delay range is set to $0 \leq \tau \leq 2$ ps, with an integration time of $2 \leq T_- \leq 10$ ps. Y-axis is set to a logarithmic scale.

with $n = 2, 3, 4, 5, 6$ corresponding to the $2p$, $3p$, $4p$, $5p$, and $6p$ states, respectively. It is important to remark that, in obtaining Fig. 3.3, we have computed the average over T_- with a time step $\delta T_- = 3$ fs. However, one can obtain the same results using a larger time step (up to 60 fs) in order to reduce (by an order of magnitude) the amount of experiments that are needed to calculate the weighted-and-averaged TPA transition probability.

To understand why two-photon virtual-state spectroscopy depends on the quantum interference of different contributions of intermediate-state transitions with a specific spectral shape, let us consider a simpler, although ideal, case where a single intermediate quantum state is present [75]. Figure 3.4 shows the two-photon transition probability as a function of the delay τ for a fixed value of T_- and T_+, considering the intermediate states: $3p$, $4p$ and $5p$. In the case of a two-photon state bearing a Gaussian mode function [Figs. 3.4(a)-(b)], and uncorrelated photons [Figs. 3.4(e)-(f)], contributions from different intermediate transitions are monotonically dependent on the delay τ. In contrast, when considering an entangled two-photon state with a sine cardinal mode function [Figs. 3.4(c)-(d)], contributions from different intermediate states exhibit an oscillatory behavior, whose frequency of oscillation corresponds precisely to the frequency of each transition. Consequently, the coherent summation of these contributions [Eq. (3.22)] leads to non-monotonic variations in the TPA signal [Fig. 3.2] that carry information about the frequency of all intermediate-state transitions. This information can later be extracted by Fourier transforming the weighted-and-averaged

(a)

(b)

(c)

(d)

(e)

(f)
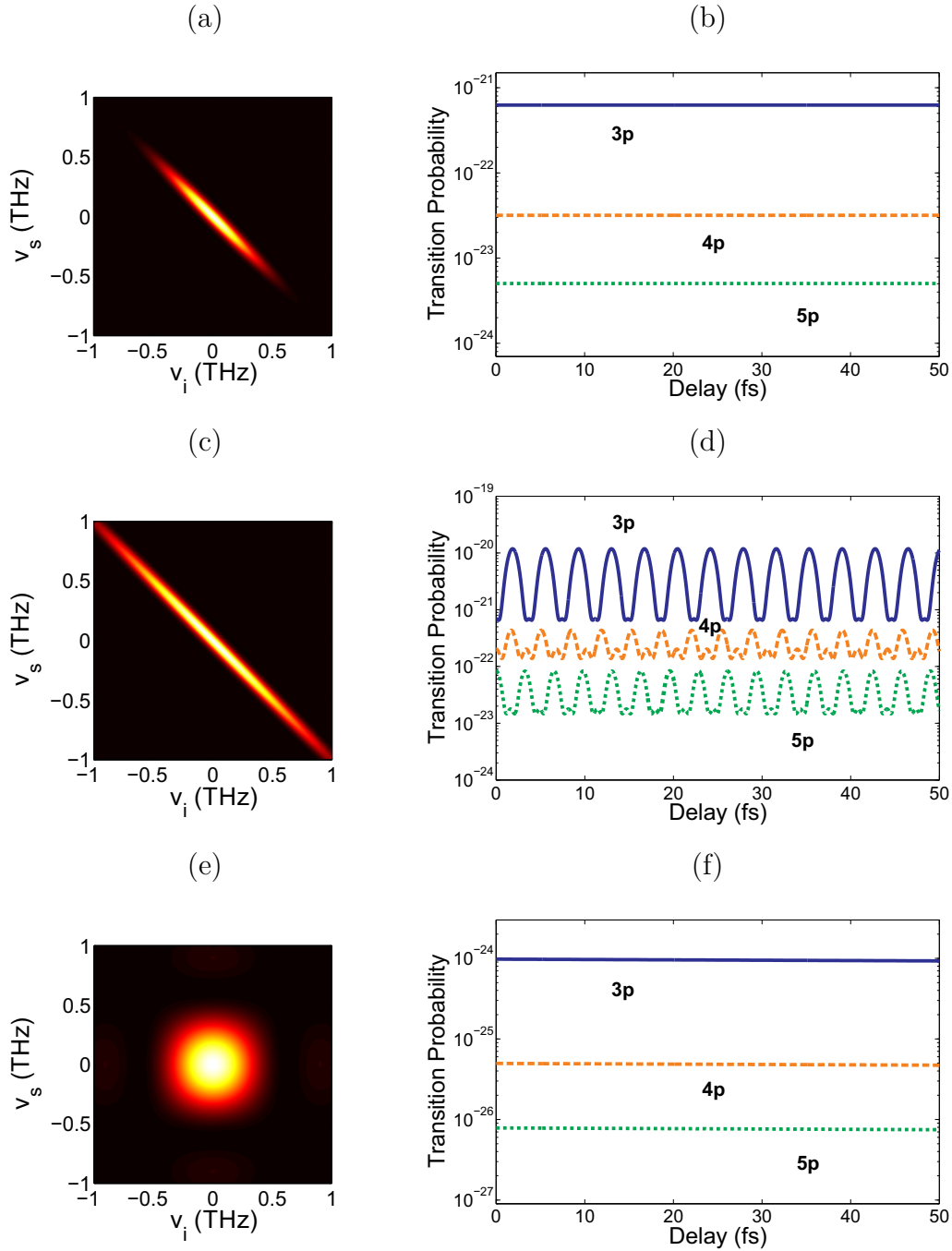

Fig. 3.4 Joint spectrum and single-intermediate level TPA transition probability as a function of the delay τ for (a,b) Gaussian mode function, (c,d) sine cardinal mode function and (e,f) uncorrelated photons. Intermediate levels correspond to: $3p$ (blue solid line), $4p$ (orange dashed line) and $5p$ (green dotted line). Pump pulse duration is set to $T_+ = 10$ ps, and $T_- = 2$ ps.

TPA signal [Eq. 3.23].

The physical reason why pairs of photons with a similar degree of entanglement, but different spectral shape, give rise to different results comes from the fact that TPA transition probabilities can be significantly affected by the shape of the two-photon mode function, as pointed out, for instance, in Ref. [75]. By increasing the time difference between the absorbed photons, i.e. increasing T_- or τ, one would expect a monotonic decay of the TPA signal, which is precisely what is observed with a Gaussian spectral shape. Interestingly, the situation changes when one considers a sine cardinal spectral shape of the photons. In this case, one can find values of T_- and τ where the TPA is no longer observed, a phenomenon dubbed entanglement-induced two-photon transparency [45]. In two-photon virtual-state spectroscopy, we benefit from this behavior to extract information about the energy level structure of the medium under study.

It is important to remark that the specific value of the pump duration T_+ does not modify the presented results, since it does not affect the way in which the contribution from different intermediate states interfere [Eq. (3.22)]. Moreover, we highlight the fact that the information depicted in Fig. 3.4 can also be obtained when quasi-uncorrelated photons are used, meaning that virtual-state spectroscopy can be performed even with a low degree of entanglement between the pair of photons. This low degree of entanglement, however, results in a lower TPA transition probability [see Eq. (3.22)], which might result in a low signal-to-noise ratio of an experimentally measured TPA signal. These results clearly describe the role of entanglement between photons, and their corresponding spectral shape, in two-photon virtual-state spectroscopy. While a proper spectral shape of the photons guarantees the successful realization of the technique, the degree of entanglement is used to control the strength of the TPA signal that is measured.

Conclusions

In this chapter, we have demonstrated that virtual-state spectroscopy cannot be performed with two uncorrelated rectangular-shaped classical pulses, which contradicts what was suggested in Ref. [71]. In addition, we have shown that the TPA transition probability of non-entangled frequency-correlated two-photon states shows a constant dependence on the temporal delay of the photons, meaning that they cannot be used in the implementation of virtual-state spectroscopy either. From these results, we

have concluded that one has to make use of two-photon states bearing non-classical frequency correlations in order to extract information about the energy level structure of an arbitrary medium. Interestingly, we have found that more important than the degree of entanglement between the photons, it is the specific spectral shape of their correlations what allows one to perform the two-photon virtual-state spectroscopy technique. We have demonstrated that while entangled states with a Gaussian spectral shape, and high degree of entanglement, cannot be used to perform virtual-state spectroscopy, surprisingly, entangled two-photon states bearing a sine cardinal spectral shape, and a very low degree of entanglement, can be used instead.

Finally, the results obtained in this chapter help to clearly identify the types of two-photon sources that can be used to experimentally implement virtual-state spectroscopy. By clarifying the role of entanglement in this technique, we have found that even paired photons carrying a low degree of entanglement, but with a proper spectral shape, can guarantee the successful retrieval of the energy level structure of the medium under study. This implies that entanglement, by itself, is not the key ingredient to experimentally perform two-photon virtual state spectroscopy.

Chapter 4

Highly efficient environment-assisted energy transport in classical oscillator systems

Because of their fundamental role in life, molecular mechanisms of energy transport in photosynthetic systems have been a subject of study for decades [78–81]. Recently, a renewed interest on this topic has arisen [82–84] thanks to the experimental observation of long-lived electronic coherences in bacterial light-harvesting complexes [85–88]. In view of these findings, several theoretical studies have been developed in order to describe, in a quantum scenario, how coherence effects could be playing an important role in the remarkably high efficiency of energy transport in photosynthetic systems [89–95]. This is specially notable since biological systems are, by definition, warm, wet and noisy systems subjected to environmental fluctuations, where quantum phenomena are unlikely to be observed.

In particular, it has been suggested that high efficiency transport arises as a result of the dynamical interplay between the "quantum" coherent evolution of the photosynthetic system and dephasing noise introduced by its surrounding environment, a phenomenon dubbed environment-assisted quantum transport (ENAQT) [96] or dephasing-assisted energy transport [97]. In coherent systems, disorder can cause localization and thus inhibit transfer [98]. In those cases, as stated in Ref. [99], ENAQT can be understood as the suppression of coherent quantum localization mediated by noise, which helps the excitation to move faster through the disordered photosynthetic

complex, thus increasing the efficiency of energy transport. In this context, ENAQT might be seen as a phenomenon that exists only in a regime where the quantum and classical worlds overlap [84].

However, in this chapter, we make use of the quantum-classical correspondence of electronic energy transfer presented in Ref. [100], to show that environment-assisted energy transport can also be found in a purely classical model, without the need to resort to quantum effects. The wider scope of applicability of the enhancement of energy transfer assisted by noise thus paves the way to the development of new technologies aimed at enhancing the efficiency of a myriad of energy transfer systems, from information channels in microelectronic circuits to long-distance high-voltage electrical lines.

This chapter is organized as follows. Section 4.1 describes the quantum model, which is represented by a system of N interacting sites, where its interaction with a surrounding environment is modeled by a pure dephasing process. We adopt this model, because it has been previously used for describing noise-assisted energy transfer processes in photosynthetic systems [96, 97, 99]. Section 4.2 presents the classical model of Refs. [100, 101], which corresponds to a system of N weakly-coupled harmonic classical oscillators. In this case, environmental effects are introduced by assuming that the frequency of each oscillator varies stochastically as a Gaussian Markov process. Finally, in section 4.3, we solve both cases using as model system a single unit of the Fenna-Matthews-Olson (FMO) complex of *Prosthecochloris aestuarii* to show that the same environment-assisted energy transport effect can be found in both classical and quantum models.

4.1   Quantum model

The dynamics of a single excitation in a network of N interacting sites is given by the tight-binding Hamiltonian [102]

$$H_S = \sum_{n=1}^{N} \epsilon_n \left| n \right\rangle \left\langle n \right| + \sum_{n \neq m}^{N} V_{nm} \left| n \right\rangle \left\langle m \right|, \tag{4.1}$$

where $\left| n \right\rangle$ denotes the excitation being at site n. The nth-site energies and the coupling between sites n and m are described by ϵ_n and V_{nm}, respectively.

To describe the dynamics of the system interacting with its surrounding environment, we make use of a simple Markovian model described by the Lindblad master

equation [103]

$$\frac{\partial \rho_{nm}}{\partial t} = -\frac{i}{\hbar} \left[H_S, \rho\right]_{nm} + \mathcal{L}_{\text{deph}} \left[\rho\right]_{nm} + D\left[\rho\right]_{nm},$$ (4.2)

where the interaction of the system with the environment is characterized by a pure dephasing process given by the Lindblad operator

$$\mathcal{L}_{\text{deph}} \left[\rho\right]_{nm} = - \left[1/2 \left(\gamma_n + \gamma_m\right) - \sqrt{\gamma_n \gamma_m} \delta_{nm}\right] \rho_{nm},$$ (4.3)

with γ_n being the dephasing rates. Even though the pure dephasing process described by Eq. (4.3) is not able to capture important aspects of electronic energy transfer, such as phonon relaxation [104], it provides a useful description of environmental effects in a simple way.

To quantify the transfer of energy from a chosen site k to the reaction center, we have phenomenologically introduced an irreversible decay process (with rate Γ) described by the operator [105]

$$D\left[\rho\right]_{nm} = -\Gamma \left\{\left|k\right\rangle \left\langle k\right|, \rho\right\}_{nm},$$ (4.4)

where $\{\cdot, \cdot\}$ stands for the anticommutator.

By making use of Eq. (4.2), one can define a measure for the efficiency of energy transport as the population transferred to the reaction center, within a time t, as

$$Q_{\text{eff}} = 2\Gamma \int_0^t \left\langle k\right| \rho\left(s\right) \left|k\right\rangle ds.$$ (4.5)

Equations (4.2) and (4.5) constitute the *quantum equations*, which have to be compared with the equations that will be obtained in the classical model.

4.2   Classical model

For the classical model, we now consider an ensemble of N weakly-coupled harmonic oscillators, each with mass M and frequency ω_n. In this case, the evolution of the system is described by the classical Hamiltonian

$$H_S = \sum_n \left(\frac{p_n^2}{2M} + \frac{M\omega_n^2}{2} q_n^2\right) + \frac{1}{2} \sum_{n \neq m} K_{nm} q_n q_m,$$ (4.6)

where q_n and p_n are the position and momentum of the oscillators, respectively, and K_{nm} stands for the coupling coefficient between the oscillators. By defining a new dimensionless complex amplitude [106]

$$\widetilde{z}_n(t) \equiv \widetilde{q}_n(t) + i\widetilde{p}_n(t), \tag{4.7}$$

with

$$\widetilde{q}_n = (M\omega_n/2\hbar)^{1/2} q_n \quad ; \quad \widetilde{p}_n = (2\hbar M\omega_n)^{-1/2} p_n, \tag{4.8}$$

the Hamilton equations of motion of the system can be cast into a single equation given by

$$\frac{\partial \widetilde{z}_n}{\partial t} = -i\omega_n \widetilde{z}_n - i \sum_m \widetilde{K}_{nm} \mathrm{Re}\{\widetilde{z}_m\}, \tag{4.9}$$

where $\mathrm{Re}\{...\}$ stands for the real part of a complex number, and

$$\widetilde{K}_{nm} = K_{nm}/(M\sqrt{\omega_n \omega_m}). \tag{4.10}$$

To include environmental effects on the system, we proceed in the same manner as in the construction of a Kubo oscillator [107, 108]. We assume that the frequency of each oscillator varies randomly, so it can be described by

$$\omega_n(t) = \omega_n + \phi_n(t), \tag{4.11}$$

where ω_n is now the average frequency of the nth oscillator and $\phi_n(t)$ describes a Gaussian Markov process satisfying the conditions

$$\langle \phi_n(t) \rangle = 0 \tag{4.12}$$
$$\langle \phi_n(t) \phi_m(t') \rangle = \gamma_n \delta_{nm} \delta(t - t'), \tag{4.13}$$

where δ_{nm} is the Kronecker delta, $\delta(t - t')$ is the Dirac delta function, and $\langle \cdots \rangle$ represents a stochastic average.

In Ref. [100], Eisfeld and Briggs demonstrated that one can transform Eq. (4.9), within the framework of Itô calculus [109], into a classical master equation that describes the temporal dynamics of a system of coupled harmonic oscillators subjected to environmental noise. However, to describe the transfer excitation from the kth oscillator to the reaction center, we extend this result and introduce an irreversible decay process (with rate Γ), described by $\mathcal{D}[\sigma]_{nm} = -\Gamma\{|k\rangle\langle k|, \sigma\}_{nm}$, where $\sigma_{nm} = \langle \widetilde{z}_n \widetilde{z}_m^* \rangle$.

In this way, we can write the *classical master equation* as

$$\frac{\partial \sigma_{nm}}{\partial t} = \mathcal{H}\left[\sigma\right]_{nm} + \mathcal{L}\left[\sigma\right]_{nm} + \mathcal{D}\left[\sigma\right]_{nm} + \frac{i}{\hbar} \sum_j \left(V_{mj} \left\langle \tilde{z}_j \tilde{z}_n \right\rangle - V_{nj} \left\langle \tilde{z}_j^* \tilde{z}_m^* \right\rangle \right), \quad (4.14)$$

with $V_{nm} = \widetilde{K}_{nm} \hbar / 2$, and

$$\mathcal{H}\left[\sigma\right]_{nm} = -i \left(\omega_n - \omega_m \right) \sigma_{nm} - \frac{i}{\hbar} \sum_j \left(V_{nj} \sigma_{jm} - V_{jm} \sigma_{nj} \right), \quad (4.15)$$

$$\mathcal{L}\left[\sigma\right]_{nm} = -\left[\frac{1}{2} \left(\gamma_n + \gamma_m \right) - \sqrt{\gamma_n \gamma_m} \delta_{nm} \right] \sigma_{nm}. \quad (4.16)$$

Using the model described by Eq. (4.14), the energy transfer efficiency within the ensemble of oscillators is then given by

$$C_{eff} = 2\Gamma \int_0^t \bar{\sigma}_{kk}\left(s\right) ds, \quad (4.17)$$

where $\bar{\sigma}\left(t\right) = \sigma\left(t\right) / \sum_n \sigma_{nn}$ is the normalized *classical density operator*.

Equations (4.14) and (4.17) represent the *classical equations*, whose results have to be compared with their quantum-mechanical counterpart, equations (4.2) and (4.5). Notice that due to the complexity of the set of quantum and classical equations, they need to be solved numerically. In particular, the computation of the classical model represents a major challenge because of the stochastic nature of Eq. (4.14). Appendix B describes the method used for solving this particular case.

4.3   Results: quantum vs classical

In the calculations that follow, we have used as model system a single unit of the Fenna-Matthews-Olson (FMO) complex of *P. aestuarii* [110]. The FMO is a pigment-protein complex that funnels energy from the light-harvesting chlorosomes to the reaction center in green sulfur bacteria [Fig. 4.1(a)] [111, 112]. It is a trimer of three identical subunits that interact weakly with each other. Each of these subunits is composed by seven bacteriochlorophyll-a (BChla) molecules supported by a protein scaffold as shown in Fig. 4.1(b). The FMO complex is generally modeled by a network of seven different sites, where the dynamics of a single excitation through the complex is governed by the specific values of the site energies (ϵ_n) and the coupling coefficients (V_{nm}). In particular, we can use the site energies and couplings given by Adolphs and Renger in Tables 2 and 4 of Ref. [110], to write the Hamiltonian (4.1) in its matrix

Highly efficient environment-assisted energy transport in classical oscillator systems
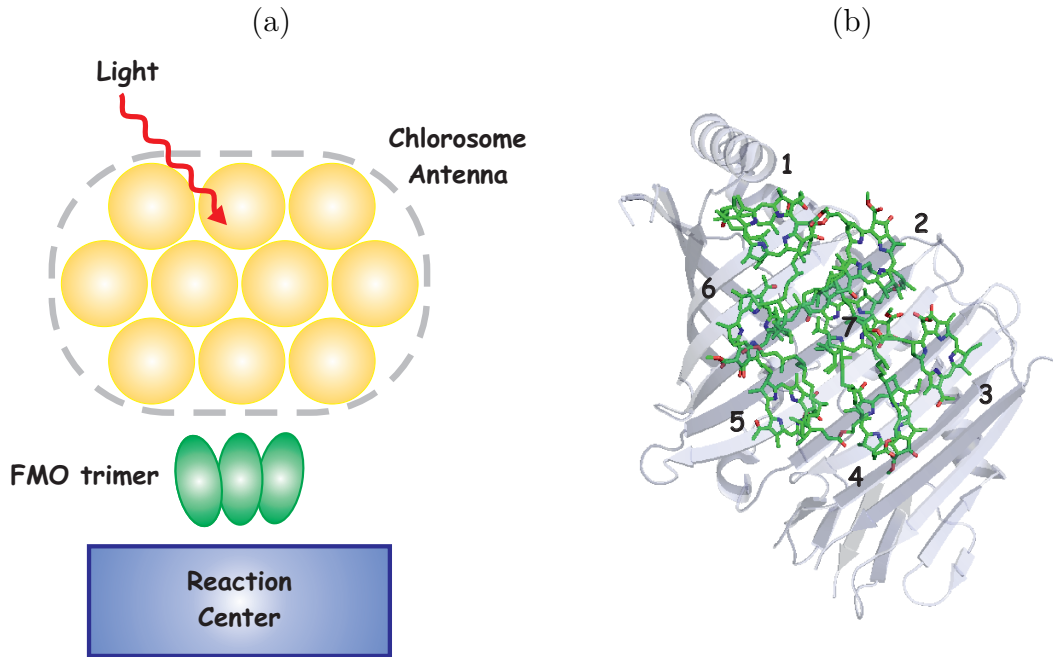

Fig. 4.1 (a) Diagram of the photosynthetic apparatus of green sulphur bacteria, including its antenna, the Fenna-Matthews-Olson (FMO) complex, and the reaction center. (b) Arrangement of the bacteriochlorophyll molecules of a single unit of the FMO complex. The figure of the FMO complex was drawn using PyMOL [19] and it is based on the Protein Data Bank entry 3ENI.

form (in units of cm^{-1}) as

$$
H_S = \begin{pmatrix}
12445 & -104.1 & 5.1 & -4.3 & 4.7 & -15.1 & -7.8 \\
-104.1 & 12450 & 32.6 & 7.1 & 5.4 & 8.3 & 0.8 \\
5.1 & 32.6 & 12230 & -46.8 & 1.0 & -8.1 & 5.1 \\
-4.3 & 7.1 & -46.8 & 12355 & -70.7 & -14.7 & -61.5 \\
4.7 & 5.4 & 1.0 & -70.7 & 12680 & 89.7 & -2.5 \\
-15.1 & 8.3 & -8.1 & -14.7 & 89.7 & 12560 & 32.7 \\
-7.8 & 0.8 & 5.1 & -61.5 & -2.5 & 32.7 & 12510
\end{pmatrix} . \tag{4.18}
$$

In our simulations, we take the initial state of the system as a single excitation being in the site 1. In FMO, BChl 3 is believed to be closest to the reaction center [110], so we set $k = 3$. We follow previous authors in estimating $\Gamma = 1 \, \text{ps}^{-1}$ [97, 113]. Furthermore, for the pure dephasing process, we consider that dephasing rates are the same for all sites ($\gamma_n = \gamma$) and that the efficiency of energy transfer is limited by the
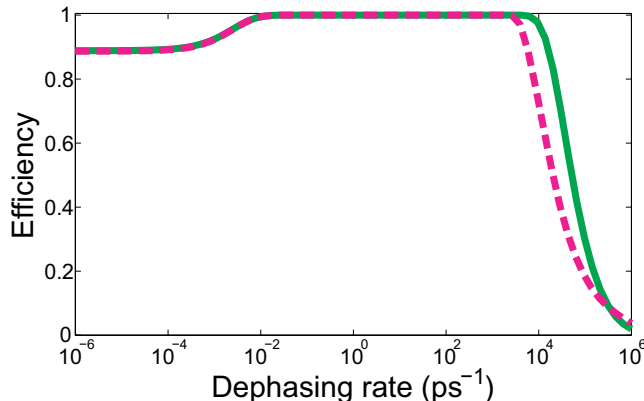
Fig. 4.2 Energy transfer efficiency in FMO as a function of the dephasing rate γ obtained from the quantum (green solid line) and the classical (pink dashed line) models.

finite excitation lifetime ($t \sim 1$ ns).

Figure 4.2 (green solid line) shows the efficiency of energy transfer as a function of the dephasing rate γ obtained by solving the quantum equations (4.2) and (4.5). We observe that at low dephasing, coherent evolution of the system leads to an efficiency of about 90%. However, when increasing the dephasing rate, efficiency grows to almost 100%, showing that environmental noise affects the system in such a way that the excitation reaches faster the trapping site, thus increasing the amount of energy that is transferred to the reaction center. Finally, for stronger dephasing, efficiency drops rapidly and almost no energy is transferred to the reaction. The effect described above corresponds to the so-called environment-assisted energy transport, which is an important phenomenon that might play a crucial role in the future design of new light-harvesting technologies.

Similar results can be obtained by using the classical model described by Eqs. (4.14) and (4.17). Figure 4.2 (pink dashed line) shows the efficiency of energy transfer as a function of the dephasing. We can observe that the same noise-assisted effect appears also in the purely classical model. Notice that both solutions agree for dephasing rates up to 10^3 ps^{-1}. However, for larger values of dephasing the quantum and classical solutions differ from each other. This in agreement with Ref. [100], where it has been shown that both models exhibit the same dynamics, provided that the condition $\gamma \ll \omega_n$ is satisfied.

Conclusions

Until recent years, noise-assisted energy transport in photosynthetic systems was understood as the suppression of coherent "quantum" localization through noise [96, 99]. However, as we have found, the same effect can also be observed in purely classical systems. This implies that one can make use of such systems in order to simulate the intricate energy transfer mechanisms that take place in molecular aggregates, such as the FMO complex.

Recently, it was suggested that classical LC oscillators (where L stands for inductance and C for capacitance) can be used to model coupled quantum two-level systems [114]. Therefore, one could think of an experimental apparatus comprising eight electrical oscillators with the eighth acting as an energy sink, i.e., the reaction center. Then, by stochastically modulating the frequencies ω_n, and properly controlling the noise intensity γ_n, one would be able, in principle, to observe the noise-assisted energy transport effect by monitoring the signal in the eighth oscillator. These classical simulations could be further used to compare with recent experimental proposals based on quantum-mechanical systems such as superconducting qubits [115], and coupled quantum-optical cavities [116].

The concept of noise-assisted transport has been extensively used for describing the inner working of quantum and classical systems [117]. Along these lines, the classical version of energy transfer assisted by noise opens a new research direction towards the development of new methods for enhancing the efficiency of a myriad of energy transport systems, such as small-scale information and energy transfer systems in microwave and photonic circuits, and long-distance high-voltage electrical lines. In this way, the work presented in this chapter demonstrates that a specific effect initially conceived in a quantum scenario is possible to be mimicked in a purely classical context, widening thus the scope of possible quantum-inspired light-harvesting technologies, such as highly efficient organic (and inorganic) solar cells.

Chapter 5

Generation of a tunable environment for electrical oscillator systems

Motivated by the results presented in the previous chapter, we now present an important step towards the simulation of photosynthetic energy transport in classical systems, namely the generation of a tunable environment for classical electrical oscillators.

The damped random-frequency harmonic oscillator is, without any doubt, a fundamental tool in statistical physics that has been extensively used to describe various physical systems in different research fields [118]. Amongst the many applications of this model, one can find that it has been successfully used, for instance, in the description of the statistical properties of dye lasers [119], the propagation of electromagnetic waves in random media [120], the population dynamics of living organisms [121], and the distribution of stock market price changes in economics [122].

As we argued in the previous chapter, networks of interacting noisy classical oscillators can feature certain physical process originally described in the study of open quantum systems, in particular the noise-assisted energy transport effect [123]. Based on these findings, one could think of reproducing the noise-assisted phenomenon by means of classical electrical systems. The use of such systems may result in experimental setups whose implementation could be easier than the recently proposed schemes based on superconducting qubits [115], and coupled quantum-optical cavities [116]. Even though the simulation of the coherent (noise-free) evolution of electrical oscillator systems is straightforward [114], the way to experimentally introduce, and control,

dephasing effects due to a surrounding environment remains a subject of lively interest.

In this chapter, we present an experimental setup that realizes as a tunable environment for classical electrical oscillators. We illustrate the operation of our experimental scheme by implementing the case of a damped random-frequency harmonic oscillator. The tunability of the system is then demonstrated by gradually modifying the statistics of frequency fluctuations, which is done by properly controlling the mean and variance of the oscillator's frequency distribution.

The proposed setup is particularly relevant, because it directly introduces fluctuations in the frequency of the oscillator, which contrasts with previous experimental studies of electrical oscillators subjected to noise, where fluctuations in the amplitude, rather than frequency, are introduced in the system [124]. Furthermore, because of its high degree of control and tunability, this system can readily be used to design various types of noise bearing different frequency probability distributions, which makes it an important tool for experimentally studying the effect of multiplicative and additive noise on instabilities of harmonic oscillators [124, 125], and for investigating the so-called noise-assisted energy transport in coupled oscillator networks.

This chapter is organized as follows. Section 5.1 provides the theoretical framework of the noisy harmonic oscillator model. Section 5.2 describes the proposed setup and section 5.3 presents the results of the experimental implementation of our scheme, where comparison with theoretical predictions is provided.

5.1   The model

The temporal evolution of a damped harmonic oscillator with a randomly fluctuating frequency is fully characterized by the equation

$$\frac{d^2x}{dt^2} + \Gamma\frac{dx}{dt} + \omega_0^2\left[1 + \phi\left(t\right)\right]x = 0, \tag{5.1}$$

where Γ is the damping coefficient, ω_0 is the average frequency of the oscillator and $\phi\left(t\right)$ describes a stochastic Gaussian process with zero average $\langle\phi\left(t\right)\rangle = 0$, and a specific autocorrelation function defined by $\langle\phi\left(t\right)\phi\left(t'\right)\rangle = \kappa\left(t - t'\right)$, where the function $\kappa\left(t - t'\right)$ defines the type of noise that influences the dynamics of the oscillator. For instance, when modeling ideal white noise, the autocorrelation function is defined as $\langle\phi\left(t\right)\phi\left(t'\right)\rangle = 2D\delta\left(t - t'\right)$, where D denotes the intensity of the noise. Another, more realistic example, is the colored noise, whose autocorrelation function writes

$\langle \phi(t) \phi(t') \rangle = (D/\tau_c) \exp(-|t - t'|/\tau_c)$, with τ_c being the correlation time of the stochastic process [126].

Using the cumulant expansion described by Van Kampen [127], one can show that the equation for the average amplitude of the oscillator $\langle x \rangle$ has the form (see Appendix C for details)

$$\frac{d^2 \langle x \rangle}{dt^2} + \left(\Gamma + \frac{\omega_0^4}{2\nu^2} c_2 \right) \frac{d \langle x \rangle}{dt} + \omega_0^2 \left[1 - \frac{\omega_0^2}{2\nu} \left(c_1 - \frac{\Gamma}{2\nu} c_2 \right) \right] \langle x \rangle = 0, \qquad (5.2)$$

where $\nu = (\omega_0^2 - \Gamma^2/4)^{1/2}$, and the coefficients c_1 and c_2 are given by

$$c_1 = \int_0^\infty \langle \phi(t) \phi(t - \xi) \rangle \sin(2\omega_0 \xi) \, d\xi, \qquad (5.3)$$

$$c_2 = \int_0^\infty \langle \phi(t) \phi(t - \xi) \rangle \left[1 - \cos(2\omega_0 \xi) \right] d\xi. \qquad (5.4)$$

Notice from Eq. (5.2) that the existence of frequency fluctuations in Eq. (5.1) introduces a noise-induced additional damping and a noise-induced frequency shift to the average signal of the oscillator. In what follows, we will use the frequency shift predicted by Eq. (5.2) in order to compare our experimental results with the theoretical model described by Eq. (5.1).

5.2   Experimental setup

The experimental scheme that allows us to introduce random frequency fluctuations into a harmonic oscillator model is described as follows. We first note that one can construct a system whose temporal dynamics corresponds to Eq. (5.1) by making use of electrical *RLC* oscillators (where R stands for resistance, L for inductance and C for capacitance). In these systems, the charge in the capacitor satisfies the same equation as Eq. (5.1), where the coefficients Γ and ω_0 are defined by [124]

$$\Gamma = R/L, \qquad (5.5)$$

$$\omega_0 = (LC_0)^{-1/2}, \qquad (5.6)$$

with C_0 denoting the average capacitance of the circuit. From Eq. (5.6) one can see that fluctuations in the frequency of the *RLC* oscillator can be introduced by
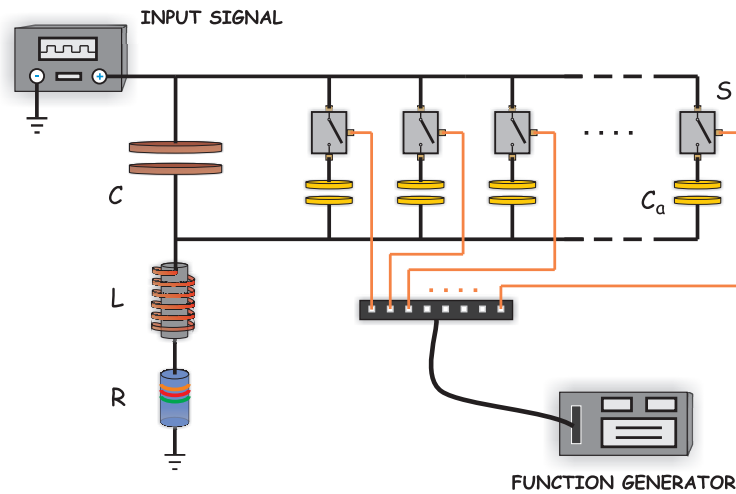
Fig. 5.1 Scheme of the damped random-frequency electrical oscillator consisting of a RLC circuit with central capacitance C, inductance L and a parasitic resistance R. Frequency fluctuations are introduced by switching *on* and *off* individual capacitors C_a by means of analog switches S, which are driven by the arbitrary function generator.

randomly switching the values of the capacitance.[1]

Random switching of capacitance is performed by connecting in parallel an array of eight capacitors, each with equal capacitance C_a, to a central capacitor C of the RLC circuit. To produce uncorrelated random switching, the individual capacitors are independently turned *on/off* by means of analog switches (NXP-74HC4066N quad bilateral switch), which are driven by independent digital signals provided by an arbitrary function generator (Signadyne digital I/O module SD-PXE-DIO-H0001), as depicted in Fig. 1. Since we are interested in simulating a Gaussian stochastic process, we program the arbitrary function generator so each capacitor has the same probability to be *on* or *off*. In this situation, one can show that the probability that n capacitors in the array are *on* satisfies a binomial distribution given by

$$P\left(n\right) = \binom{8}{n}\frac{1}{2^8},\tag{5.7}$$

where $n = \{0, 1, 2, ..., 8\}$. This distribution is defined by a mean value $\langle n \rangle = 4$ and a variance $\sigma_{\mathrm{b}}^2 = 2$. Note that the binomial distribution described in Eq. (5.7) is

---

[1]For the sake of simplicity, we have selected a random switching of the capacitance. However, one can always choose to randomly change the values of the inductance. By doing this, one adds more complexity to the system since the damping coefficient would randomly fluctuate as well.
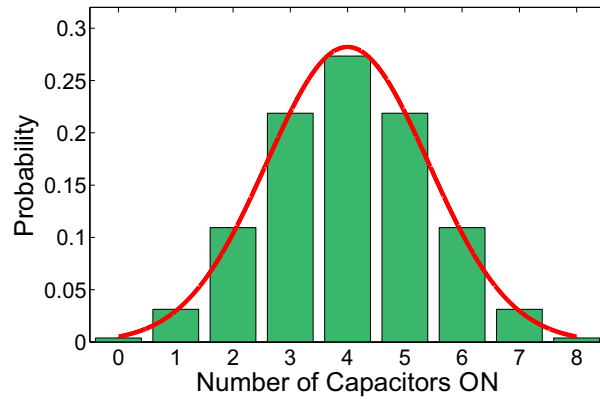
Fig. 5.2 The probability that n capacitors in the array are *on* follows a binomial distribution, which corresponds to a discretized Gaussian distribution with the same average and variance.

a discrete version of a Gaussian distribution with the same mean and variance, as depicted in Fig. 5.2. Notice from [Eq. (5.6)], that there exists a nonlinear relation between frequency and capacitance, which implies that the probability distribution of the frequency would correspond to a Gaussian distribution only in the cases where the condition $C_a \ll C$ is satisfied [128].

5.3 Implementation and Results

To illustrate the working of the proposed scheme, we construct a *RLC* circuit where the central capacitance C is provided by a 1 nF ceramic capacitor, the inductance L is introduced by a 1.5 mH ferrite core inductor, and resistance R represents the parasitic losses within the system. For the random switching of capacitance, we have designed several arrays using different ceramic capacitors with capacitance value $C_a = \{4.7, 10, 18, 33, 47, 68, 100\}$ pF. Note from Fig. **??** that by changing the values of C_a, we can modify the variance of the Gaussian frequency distribution, which in turn modifies the statistics of the noise in the system [126].

Because the frequency fluctuations need to be faster than the characteristic time evolution of the system, the digital signals from the arbitrary function generator are set to a time rate $\tau = 650$ ns, which is a longer time-duration than the response time of the analog switches (400 ns), and much shorter than the temporal evolution window ($t = 100$ μs) considered for the measurement of the signal.

(a)

(b)
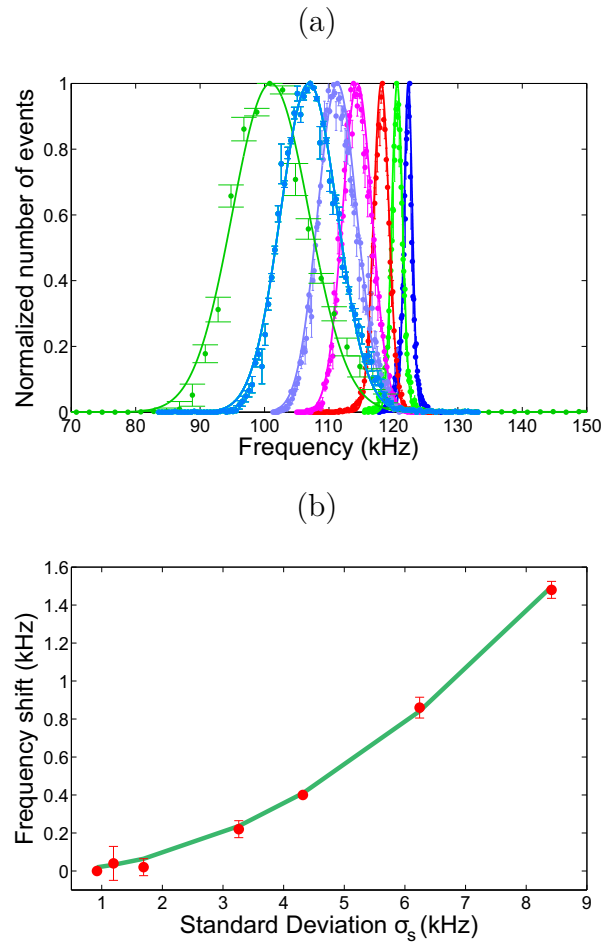
Fig. 5.3 (a) Signal frequency histograms using different capacitor arrays. From left to right: $C_\mathrm{a} = 100, 68, 47, 33, 18, 10, 4.7$ pF. Dotted line: Experimental data, Solid line: Gaussian fitting. (b) Frequency shift as a function of the standard deviation σ_s. Dotted line: Experiment, Solid line: Theory.

Using the system described above, we have performed the simulation of Eq. (5.1). For this, we have kept the capacitor C fixed and measured the average signal of the oscillator connected to different capacitor arrays. Figure 5.3(a) shows the histograms of the measured frequency in each case. Histograms were obtained from 50000 different realizations and they are normalized to the maximum number of events, where we define number of events as the number of realizations that have the same value of frequency. Notice that in all cases the probability distribution of the frequency follows a Gaussian distribution whose variance σ_s^2 depends on the value of C_a used in each capacitor array. These results demonstrate that the proposed setup allows one to

Fig. 5.4 Frequency histograms for different capacitor arrays centered in the same mean frequency $f_0 \simeq 123$ kHz. Dotted line: Experimental data, Solid line: Gaussian fitting. Parameters of the system used in each case are summarized in Table 5.1.
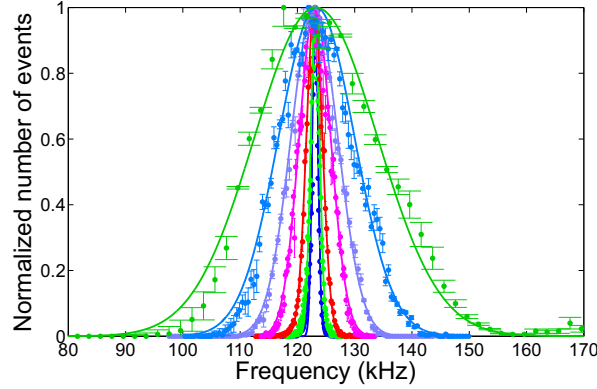
control the statistics of the noise that is introduced in the system, which is important when simulating the dynamics of open systems [96, 97, 100, 123].

To compare the results presented in Fig. 5.3(a) with the theoretical model, we have measured the frequency shift that arises out of the frequency fluctuations in Eq. (5.2). Figure 5.3(b) shows the frequency shift for each capacitor array. We have made use of Eq. (5.2), and the relation $D = \sigma^2 \tau$ [126], to find that the driving noise of our system can be described by a colored-noise-like autocorrelation function of the form

$$\langle \phi(t) \phi(t') \rangle = \frac{\sigma^2}{\omega_0^2} \exp\left(-\frac{|t - t'|}{\tau}\right), \tag{5.8}$$

where the mean value of the frequency is obtained by setting $C_0 = C + 4C_a$, and the variance of the driving noise is $\sigma^2 = (\eta \sigma_s)^2$, with $\eta = 3.4$. This relation between both variances can be understood as a consequence of the damping term in Eq. (5.1). The same effect can be found, for instance, in the Ornstein-Uhlenbeck process, where the resulting variance is proportional to the variance of the driving noise due to the presence of a damping term [127].

In general, when simulating open systems, one is interested in maintaining the mean frequency of each oscillator while increasing the strength of the noise [96, 97, 123]. This can be achieved in our system by properly controlling the values of the central capacitance C and the time duration τ of the digital signals. Figure 5.4 shows the frequency histograms measured with different capacitor arrays. Notice that by carefully selecting the parameters of the system, we are able to center all

C_a (pF)	4.7	10	18	33	47	68	100
C (nF)	1.120	1.090	1.053	0.978	0.933	0.840	0.355
τ (ns)	650	650	750	780	800	720	650

Table 5.1 Experimental parameters used to obtain the histograms shown in Fig. 5.4

the probability distributions in the same mean value of the frequency $f_0 \simeq 123$ kHz. Parameters of the system used in each case are summarized in Table 5.1. The results shown in Figs. 5.3 and 5.4 demonstrate the flexibility of our system when modifying the statistical properties of the environmental noise that interacts with the oscillator.

Conclusions

In this chapter, we have presented a system that performs as a tunable environment for classical electrical oscillators. We have illustrated its operation by simulating the case of a damped random-frequency harmonic oscillator, where perfect agreement with the theoretical model was obtained. Furthermore, we have demonstrated the high degree of control and tunability that our system can provide by gradually modifying the variance of the frequency fluctuations, while at the same time maintaining a fixed central frequency of oscillation, which is of great importance when simulating energy transfer mechanisms.

The high degree of tunability and control of the system may also allow us to design various types of noise with different probability distributions, which could be used in the study of instabilities of harmonic oscillators. Moreover, it might allow us to study the transition from Markovian to non-Markovian dynamics of open systems.

Finally, the results presented in this chapter represent an important step towards the simulation of photosynthetic energy transport in classical systems. These classical simulations could be used to compare with experimental proposals based on quantum-mechanical systems, to finally unveil which phenomena exclusively belong to the quantum world and which could be reproduced by purely classical models.

Chapter 6

Role of excitation and trapping conditions in photosynthetic energy transport

As we mentioned in previous chapters, since its first description in 2009, environment-assisted quantum transport (ENAQT) has been shown to be an important effect that occurs in a wide variety of quantum [96, 97, 99, 129–132] and classical [123] transport systems. Most importantly, it has been considered as the key process that enables the highly efficient energy transport of photosynthetic light-harvesting complexes [83, 84]. However, ENAQT has usually been investigated under assumptions that have been challenged since. In particular, in most models, it has been assumed that the system starts out with only one pigment molecule initially excited and that only one pigment molecule (the "trap") is responsible for the ultimate exciton transfer to the reaction center (RC). These assumptions are now known to be physically inaccurate: unless the system is so disordered that each eigenstate is effectively localized on one site, both the initial state and the trap will be at least partially delocalized.

In this chapter, we examine ENAQT in situations where both the excitation and the trapping are treated in more physically realistic ways. The most important result that we show is that the description of the coupling to the RC significantly influences the magnitude and, consequently, the importance of the predicted ENAQT. If the trap is localized at a particular site, as it has been assumed in previous works, we show that ENAQT persists under almost all excitation conditions, including excitation

by incoherent light (as predicted in Ref. [95]) as well as excitation transfer from an antenna complex. Notwithstanding, ENAQT is either absent or negligible if the coupling to the RC is treated as Förster transfer (as we argue it should be), meaning that it is unlikely to be important for influencing the biological function of natural light-harvesting complexes.

This chapter is organized as follows. Section 6.1 presents the general theoretical model that allows us to explore ENAQT under different excitation and trapping conditions. Section 6.2 shows the results of the calculations for each particular excitation and trapping condition and, in Section 6.3, we discuss the obtained results and explain, in physical terms, why they call into question the suggestion that natural selection has optimized the interplay between quantum dynamics and noise in order to achieve a highly efficient photosynthetic energy transport.

6.1   The model

Even though in chapter 4 we have already presented part of the theory of excitonic transport in photosynthetic systems, for completeness and easy reading of this chapter, we will describe the exciton dynamics model from the very beginning.

Let us consider the dynamics of excitons in a network of N chromophores (or sites). Under usual weak illumination, it is rare to find more than one exciton in a single complex. Therefore, we restrict ourselves to the single-exciton manifold, with state $|n\rangle$ indicating that the exciton is on site n. The system is then described by the tight-binding Hamiltonian [102]

$$H_S = \sum_{n=1}^{N} \epsilon_n |n\rangle \langle n| + \sum_{n \neq m}^{N} V_{nm} |n\rangle \langle m| , \tag{6.1}$$

where ϵ_n are the excitation energies of the molecules and V_{nm} the intermolecular couplings. We will denote the eigenstates of H_S as $|e_n\rangle$, with energies E_n,

$$H_S |e_n\rangle = E_n |e_n\rangle . \tag{6.2}$$

Also, we will refer to the state where no excitons are present as $|0\rangle$ and the state where the exciton has been transferred to the reaction center as $|RC\rangle$. Neither $|0\rangle$ nor $|RC\rangle$ are coupled to the states $|n\rangle$ through H_S.

The dynamics of a photosynthetic system interacting with its environment is in

general complicated and non-Markovian [102]. However, because this work is about qualitative features of ENAQT, we will use a Markovian model that, although simplistic, captures the essential physics, which is why it has been used in previous works [96, 97, 129]. We assume that the system-environment interaction can be modeled using a Lindblad master equation, according to which the density matrix ρ of the system obeys [103]

$$\frac{\partial \rho}{\partial t} = -\frac{i}{\hbar}[H_s, \rho] + \mathcal{L}_{\text{deph}}[\rho] + \mathcal{L}_{\text{diss}}[\rho] + \mathcal{L}_{\text{RC}}[\rho], \tag{6.3}$$

where the various non-unitary contributions are denoted $\mathcal{L}$. In particular,

$$\mathcal{L}_{\text{deph}}[\rho] = \sum_{n=1}^{N} 2\gamma_n \left(|n\rangle \langle n| \rho |n\rangle \langle n| - \frac{1}{2} \{|n\rangle \langle n|, \rho\} \right), \tag{6.4}$$

where $\{\cdot, \cdot\}$ is the anticommutator, describes a pure dephasing process that destroys the phase coherence between different sites at a site-dependent dephasing rate γ_n. This dephasing can be thought of as being caused by environment-induced fluctuations in the site energies [102]. Notice that this interpretation of dephasing was used in chapter 4 in order to develop the classical model of the dynamics of photosynthetic systems influenced by noise. The important aspect of Eq. (6.4) is that it acts on the site basis, a feature it shares with most models of chromophore noise, even those that are non-Markovian or at relatively low temperatures.

The remaining two terms in Eq. (6.3) describe two mechanisms by which the excitation can be lost during its motion throughout the photosynthetic complex. For the first term, we assume that the exciton can recombine at each site, transferring the excitation to the ground state $|0\rangle$ at a rate Γ_n

$$\mathcal{L}_{\text{diss}}[\rho] = \sum_{n=1}^{N} 2\Gamma_n \left(|0\rangle \langle n| \rho |n\rangle \langle 0| - \frac{1}{2} \{|n\rangle \langle n|, \rho\} \right). \tag{6.5}$$

The second term, $\mathcal{L}_{\text{RC}}[\rho]$, describes the unidirectional transfer of excitations to the RC. Because it also causes exciton disappearance from the $|n\rangle$-manifold, it will have a form analogous to Eq. (6.5). In what follows, we discuss its precise form, depending on the trapping conditions. In any case, the exciton will eventually either dissipate or be transferred to the RC, which motivates the definition of the efficiency η as the

probability that the energy will arrive at the RC rather than being dissipated

$$\eta = \lim_{t \to \infty} \langle \mathrm{RC} | \rho(t) | \mathrm{RC} \rangle . \tag{6.6}$$

The work presented in this chapter is about the value of η in different illumination and trapping conditions.

6.1.1 Transfer to the RC

In this chapter, the important message that we want to convey is that η is highly sensitive to how we describe the exciton transfer $\mathcal{L}_{\mathrm{RC}}[\rho]$ from the photosynthetic complex to the RC. The usual approach has been to use

$$\mathcal{L}_{\mathrm{RC}}[\rho] = \mathcal{L}_{\mathrm{RC}}^{\mathrm{local}}[\rho] = 2\Gamma_{\mathrm{RC}} \left(|\mathrm{RC}\rangle \langle k| \rho |k\rangle \langle \mathrm{RC}| - \frac{1}{2} \{ |k\rangle \langle k| , \rho \} \right), \tag{6.7}$$

where it is assumed that only one site, denoted k, transfer excitation to the RC (hence the superscript "local"). As we argued in chapter 4, Eq. (6.7) is based on the assumption that a particular site is closest to the RC and, consequently, that it will be the only one coupled to the RC. In that case, the efficiency can also be written as in Eq. (4.5), i.e.,

$$\eta = 2\Gamma_{\mathrm{RC}} \int_0^t \langle k| \rho(s) |k\rangle \, ds. \tag{6.8}$$

However, the localized transfer model does not correctly describe the physics of exciton transfer between a photosynthetic complex and a reaction center, which are weakly coupled. Exciton transfer between weakly coupled complexes is an incoherent process and proceeds via Förster resonant energy transfer (FRET) [102] at a rate given by Fermi's golden rule,

$$\kappa = \frac{2\pi}{\hbar} \sum_{D_i, A_i} \sum_{D_f, A_f} g_D(D_i) g_A(A_i) \left| \langle D_i A_i | J | D_f A_f \rangle \right|^2 \delta(E_{D_i} + E_{A_i} - E_{D_f} - E_{A_f}), \tag{6.9}$$

where the sums are over the *eigenstates* D_i and A_i of the (excited) donor and the (de-excited) acceptor and D_f and A_f of the (de-excited) donor and the (excited) acceptor. The initial populations of the donor and acceptor states are g_D and g_A, respectively, and the coupling $\langle D_i A_i | J | D_f A_f \rangle$ is the matrix element of the complete donor-acceptor Coulomb interaction J.

As emphasized above, FRET is a transfer process between populations of the donor

and acceptor eigenstates, *not sites.* In this situation, if the coupling J only involves site k in the donor, as it is reasonable to suppose, it should be decomposed into eigenstate components, each of which contributes to an independent incoherent rate. In the present case, this means replacing $\mathcal{L}_{RC}^{local}$ with

$$\mathcal{L}_{RC}^{FRET}[\rho] = 2\Gamma_{RC} \sum_{n=1}^{N} |\langle e_n | k \rangle|^2 \left(|RC\rangle \langle e_n | \rho | e_n \rangle \langle RC| - \frac{1}{2} \{|e_n\rangle \langle e_n|, \rho\} \right). \qquad (6.10)$$

The efficiency can still be calculated using Eq. (6.6), or, alternatively, Eq. (6.8) can be modified to

$$\eta = 2\Gamma_{RC} \int_0^t \sum_{n=1}^{N} |\langle e_n | k \rangle|^2 \langle e_n | \rho(s) | e_n \rangle \, ds. \qquad (6.11)$$

In the following, we will show results of calculations using both $\mathcal{L}_{RC}^{local}$ and $\mathcal{L}_{RC}^{FRET}$ in order to relate this work to previous studies and to highlight the importance of correctly modeling the system-RC coupling.

6.1.2 Initial excitation

In the same manner as in the case of energy transfer to the RC, the particular choice of an initial state for Eq. (6.3) involves certain concerns. Most importantly, it should be stressed that the excitation of photosynthetic complexes is not impulsive, except perhaps in ultrafast experiments. Rather, excitation occurs through a steady state [95, 133–135], where an external energy source, whether light or an antenna complex, continuously pumps the systems and where the excitation energy is continuously lost to either the environment or the RC.

In a steady-state context, the natural definition of efficiency is the ratio of exciton (or energy) flux to the RC to the incoming flux that pumps the system. Consequently, Eqs. (6.6), (6.8), and (6.11) may seem inappropriate. However, Jesenko and Žnidarič have shown that the efficiency of a steady-state process is equal to the efficiency of the corresponding impulsive case [136]. This implies that we can still use Eqs. (6.8) and (6.11) to evaluate the efficiency of energy transport and, at the same time, relate our results to the existing body of work.

We will consider three excitation regimes: localized excitation, excitation by transfer from an antenna complex, and photoexcitation.

Role of excitation and trapping conditions in photosynthetic energy transport

Localized initial excitation

The simplest model of initial excitation is localized excitation of a single site, which has been considered in numerous studies of excitonic energy transport and ENAQT [90, 94, 96, 97, 99, 129, 131, 134]. In this case, we can take "1" as the initially excited site and write the initial state of the system as

$$\rho_{\text{local}} = |1\rangle \langle 1|. \tag{6.12}$$

Using this initial state is equivalent, in the sense of Jesenko and Žnidarič [136], to a steady-state system whose master equation includes an additional term that transfers population from the ground state to $|1\rangle$,

$$\mathcal{L}_{\text{pump}}[\rho] = 2\Gamma_{\text{pump}} \left(|1\rangle \langle 0| \rho |0\rangle \langle 1| - \frac{1}{2} \{|0\rangle \langle 0|, \rho\} \right). \tag{6.13}$$

Excitation transfer from antenna complex

In many photosynthetic architectures, an exciton is harvested by peripheral antenna complexes before being transferred to the RC via other, intermediate complexes. This situation motivates the question of what is the appropriate initial state for an intermediate complex like FMO, which is excited by an antenna complex. As with transfer from a complex to the RC, transfer from an antenna is incoherent and proceeds by FRET. If the site closest to the antenna is "1", FRET would populate excitonic eigenstates in proportion in which they occur at site 1, giving the initial state

$$\rho_{\text{ant}} = \sum_{n=1}^{N} |\langle 1|e_n\rangle|^2 |e_n\rangle \langle e_n|. \tag{6.14}$$

The corresponding continuous pumping term is easily written down in analogy to Eq. (6.13).

Photoexcitation

When a light-harvesting complex is excited, one must distinguish the cases of coherent and incoherent illumination [95, 133, 135, 137–140].

On one hand, if the incoming light is incoherent (as is sunlight), various frequencies only excite populations of the eigenstates with which they are resonant, and not coherences between them [133, 137, 138]. If we assume that each transition has the same

oscillator strength, incoherent light will create a mixture of eigenstates in proportion to the intensity of the light spectrum at the transition frequency. For thermal light, such as sunlight, one obtains pumping from the ground state to

$$\rho_{\text{incoh}} = \frac{1}{\mathcal{N}} \sum_{n=1}^{N} I(E_n) \, |e_n\rangle \, \langle e_n| \,, \tag{6.15}$$

where $I(\omega)$ is the Planck distribution for the thermal light (we have used $T = 5800$ K, the effective temperature of the Sun, in calculations below) and $\mathcal{N}$ is the normalization constant. This is the correct "initial" state, in the sense of Jesenko and Žnidarič [136], for what is in reality a steady-state process.

If, on the other hand, the complex were excited by a coherent, transform-limited laser pulse, one would obtain a superposition instead of a mixed state [133, 137, 138]. The state will depend on details such as the spectrum, duration, intensity, and polarization of the pulse. However, to enable comparison with Eq. (6.15), we assume the same spectrum and that all eigenstates acquire the same phase, so we write the initial state as

$$\rho_{\text{coh}} = |\psi\rangle \, \langle\psi| \,, \quad \text{where} \quad |\psi\rangle = \frac{1}{\sqrt{\mathcal{N}}} \sum_{n=1}^{N} \sqrt{I(E_n)} \, |e_n\rangle \,. \tag{6.16}$$

6.2 Results

In the calculations that follow, we have used as the model system system a single unit of the FMO complex of *P. aestuarii*. In the same fashion as in chapter 4, we have used the site energies ϵ_n and couplings V_{nm} given in Tables 2 and 4 of Ref. [110], as well as the transfer rate $\Gamma_{\text{RC}} = 1$ ps^{-1}. For the newly introduced dissipation process, namely the irreversible lost of energy to the environment, we have assumed that the dissipative rates are the same for all molecules, $\Gamma_n = \Gamma = 5.0 \times 10^{-4}$ ps^{-1} [141], as are the dephasing rates, $\gamma_n = \gamma$, which we have taken to be an adjustable parameter.

We have calculated the efficiency η of excitonic transport through FMO using both the localized coupling to the RC and FRET models [Eqs. (6.7) and (6.10), respectively], as well as using all of the initial excitation conditions described in the previous section. In all cases, we have calculated the efficiency as a function of the dephasing rate γ, which allows us to detect the presence or absence of ENAQT. The results are shown in Figs. 6.1(a) and 6.1(b).

Role of excitation and trapping conditions in photosynthetic energy transport
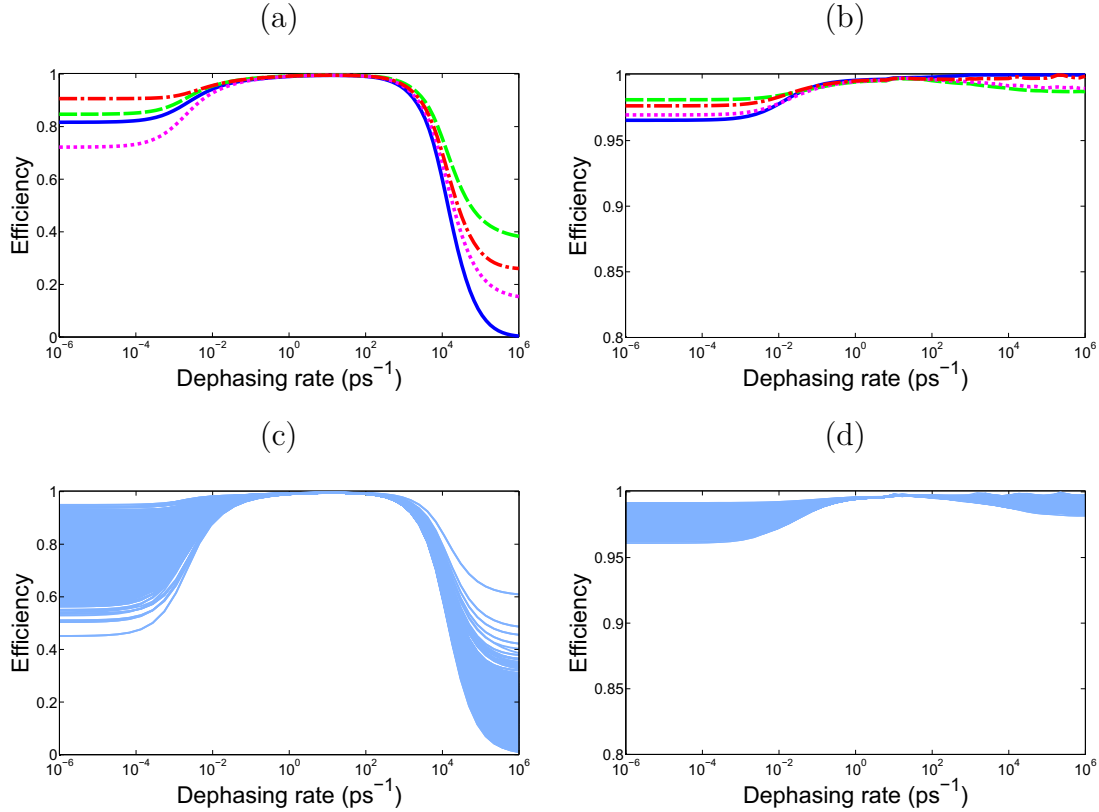

Fig. 6.1 Energy transfer efficiency in FMO as a function of the dephasing rate, assuming different initial states and different trapping mechanisms.
(a) Calculated using localized transfer to the reaction center (RC), as had been assumed in most previous works, Eq. (6.7). The efficiency is shown for four initial states:

- (i) ρ_{local}, transfer into site 1, Eq. (6.12) (solid line),
- (ii) ρ_{ant}, incoherent transfer from an antenna complex, Eq. (6.14) (dashed line),
- (iii) ρ_{incoh}, incoherent photoexcitation, Eq. (6.15) (dotted line),
- (iv) ρ_{coh}, coherent photoexcitation, Eq. (6.16) (dash-dotted line).

(b) Same initial states as in (a), but the exciton transfer to the RC is modeled as Förster resonant energy transfer (FRET), which is more physically realistic, see Eq. (6.10). Note the enlarged scale on the vertical axis.
(c) Same as (a), but with 1000 randomly chosen initial states, showing that ENAQT occurs in almost all initial conditions.
(d) Same as (b), but with 1000 randomly chosen initial states, showing that the four initial states above are typical.

To verify that the results for particular initial states hold in general, we have also computed the transport efficiency for 1000 random pure initial states, sampled from the uniform distribution on the $\mathbb{C}^7$ Hilbert space. This was done by normalizing a

vector X of 7 independent, identically distributed complex Gaussian random variables, $|\psi\rangle = X/\|X\|$. The results are shown in the shaded bands in Figs. 6.1(c) and 6.1(d). It is important to remark that, if the initial state were mixed, the efficiency would still lie within these bands because the efficiency, being a linear function of the initial state, is a convex combination of the component pure-state efficiencies.

6.3 Discussion

The results presented in Figs. 6.1(a)-(c) are drastically different to those in Figs. 6.1(b)-(d), which implies that it is crucial to describe the process of energy transfer to the RC correctly. We discuss the two cases separately.

6.3.1 Local transfer to the RC

In the case where $\mathcal{L}_{\mathrm{RC}}^{\mathrm{local}}$ is used to model exciton transfer from the FMO to the RC, we can observe from Figs. 6.1(a)-(c) that ENAQT survives under all initial conditions, including the biologically relevant transfer from antenna complex and excitation by incoherent light. The only exception would be if the exciton were initialized directly at the trap, which would result in a maximum of efficiency at infinite dephasing.

Whether ENAQT is observed depends on a competition of time scales. In particular, the fact that $\Gamma_{\mathrm{RC}} \gg \Gamma$ implies that any excitation that can reach the trap will be caught, increasing thus the efficiency. In any case, the excitation can only be dissipated if it gets stuck away from the trap by some means.

If dephasing (or other type of noise) is weak or absent, it is most appropriate to think of transport in the basis of the eigenstates of the Hamiltonian [102]. In the case where dephasing is very weak (or completely absent), the trapping at rate Γ_{RC} will quickly remove the exciton population at the trap site, leaving behind a state with no support at the trap. Since the exciton lifetime is finite, the eigenstate linewidths will broaden and partially overlap, allowing excitons to flow back to the trap site. However, because the dissipation is weak and the line broadening correspondingly small, this process will be slow, allowing a fraction of the population to be dissipated at the slower rate Γ. This dissipated energy would, of course, depend on the initial excitation state, as can be observed from in Figs. 6.1(a)-(c), where transport efficiencies of about 70–90% are obtained.

In the presence of weak (moderate) noise, the time-dependent environmental fluc-

tuations behave as perturbations that can shift populations between different eigenstates. In this situation, the excitons will shift among various sites as well, allowing almost all of them to reach the trapping site (and therefore be trapped) during the dissipative lifetime Γ^{-1}. This explains the enhancement in the energy transport efficiency at intermediate levels of dephasing, where almost 100% efficiency is achieved.

However, if the dephasing becomes very strong, the environment is essentially monitoring the populations at different sites. This gives rise to the Zeno effect, preventing excitons from moving between sites. Because excitons at non-trap sites will all be dissipated, the efficiency in this case would correspond to the initial population at the trap site multiplied by the branching ratio $\Gamma_{\mathrm{RC}}/(\Gamma + \Gamma_{\mathrm{RC}})$.

6.3.2 FRET to the RC

In the case where exciton transfer to the RC is modeled by using $\mathcal{L}_{\mathrm{RC}}^{\mathrm{FRET}}$, one obtains very different and contrasting results. We can observe from Figs. 6.1(b)-(d) that, in this situation, ENAQT is either much reduced or vanishes altogether. At most, the dephasing-induced enhancement of the energy transport rate is about 4%.

The efficiency is uniformly high in this case, always exceeding 96%. As mentioned before, $\Gamma_{\mathrm{RC}} \gg \Gamma$ means that the only way to get low efficiency is if the exciton is somehow prevented from reaching the trap site. If the trap is localized, as when $\mathcal{L}_{\mathrm{RC}}^{\mathrm{local}}$ is used, this can be achieved by also localizing the exciton. In contrast, when using $\mathcal{L}_{\mathrm{RC}}^{\mathrm{FRET}}$ the population from all eigenstates (albeit with different rates) is trapped, meaning that the exciton has nowhere to hide. The difference between these two regimes is most pronounced at high dephasing. In the local trap model, the Zeno effect can completely suppress the motion of the exciton to the trapping site, whereas in the FRET model this is no longer a problem, since all sites are able to transfer energy to the reaction center.

It is important to remark that similar results about exciton transport in FMO were obtained by Pelzer *et al.* [142] using the Keldysh Green's function formalism and assuming that the exciton source is an incoherent antenna complex. In their model there is also no ENAQT, in the sense that the probability that an exciton injected into FMO reaches the RC monotonically increases with the dephasing rate. The differences between their results and ours follow from different descriptions of the antenna and the RC. Pelzer *et al.* describe both the chlorosome and the RC as individual sites that are resonant with the highest and lowest exciton energies in FMO, respectively. One consequence of this model is that the exciton flux from the chlorosome to FMO

decreases with the dephasing rate. In contrast, we have assumed that the chlorosome spectrum is broad and that it can drive various transitions in FMO via FRET.

Conclusions

In this chapter, we have shown that changes in how the final exciton transfer to the RC is modeled can lead to qualitatively different conclusions about the importance of environmental noise in exciton transport. Although ENAQT is a robust effect that occurs with all initial states if one assumes a localized trapping, it mostly vanishes if the transfer to the RC is modeled as Förster transfer.

Even though we have used a simplified Markovian model in this work to emphasize the relevant physics, we would expect qualitatively similar behavior in more complicated models as well, provided that they involve variable-strength noise acting in the site basis (as most noise models do). Indeed, simulations of ENAQT in FMO using more sophisticated noise models have not found qualitatively important differences from the results obtained in the pure-dephasing model [130, 132]. Furthermore, although non-Markovian effects can influence the transport efficiency [132, 143], this is not a concern in steady-state systems, such as natural or artificial light-harvesting, where equivalent Markovian baths can be used.

Finally, as we have argued throughout this chapter, the FRET trapping model is likely to be the one that correctly captures the physics of excitonic transfer between weakly coupled complexes. The fact that the FRET model allows only a very small ENAQT motivates us to call into question the widespread view that natural selection has optimized the interplay between quantum dynamics and noise in order to achieve a highly efficient photosynthetic energy transport.

Summary and Conclusions

The results presented in this thesis can be summarized in two parts. In the first part, we have shown how concepts and techniques routinely used in quantum optics can provide a means for developing new highly sensitive spectroscopy techniques. Along these lines, (i) we have put forward a new technique for enhancing the sensitivity, and robustness, of an optical label-free imaging system based on the quantum-mechanical effect of stimulated Raman adiabatic passage. (ii) We have proposed a new way for measuring the temperature of atomic ensembles by making use of a fundamental feature of quantum interference known as which-way information, and (iii) we have demonstrated that two-photon virtual-state spectroscopy cannot be performed by means of classical light and that two-photon states bearing non-classical frequency correlations (entanglement), with a specific spectral shape, are needed in order to perform such technique.

The second part of this thesis has been devoted to exploring certain mechanisms of energy transport in photosynthetic light-harvesting complexes. This work has been done with the aim of recognizing whether quantum effects are necessary in order to explain the highly efficient transport behavior of photosynthetic systems. In this way, (iv) we have explicitly demonstrated that noise-assisted energy transport, a phenomenon originally conceived in a quantum scenario, can be found as well in purely classical systems. Motivated by these findings, (v) we have implemented the generation of a tunable environment for electrical oscillators, which represents an important step towards the simulation of photosynthetic energy transport in classical systems and, finally, (vi) we have provided the first study of photosynthetic environment-assisted energy transport, where the initial excitation of the photosynthetic complex and the energy transfer to the reaction center are treated in more physically realistic ways. We have shown that energy transport behavior is very sensitive to the details of these processes, particularly to the energy transfer to the reaction center. Moreover, we have demonstrated that the effect of the environment on the transport efficiency becomes

negligible when considering more physically accurate models of energy transfer to a reaction center. Therefore, based on these results, we have called into question the suggestion that natural selection has optimized the interplay between quantum dynamics and noise in order to achieve a highly efficient photosynthetic energy transport.

Bibliography

[1] T. G. Spiro, "Resonance Raman spectroscopy. New structure probe for biological chromophores," *Acc. Chem. Res.*, vol. 7, p. 339, 1974.

[2] C. W. Freudiger, W. Min, B. G. Saar, S. Lu, G. R. Holtom, C. He, J. C. Tsai, J. X. Kang, and X. S. Xie, "Label-free biomedical imaging with high sensitivity by stimulated Raman scattering microscopy," *Science*, vol. 322, p. 1857, 2008.

[3] A. Doerr, "Imaging goes label-free," *Nat. Methods*, vol. 6, p. 116, 2009.

[4] J. Oreg, F. T. Hioe, and J. H. Eberly, "Adiabatic following in multilevel systems," *Phys Rev. A*, vol. 29, p. 690, 1984.

[5] K. Bergmann, H. Theuer, and B. W. Shore, "Coherent population transfer among quantum states of atoms and molecules," *Rev. Mod. Phys.*, vol. 70, p. 1003, 1998.

[6] J. R. Kuklinski, U. Gaubatz, F. T. Hioe, and K. Bergmann, "Adiabatic population transfer in a three-level system driven by delayed laser pulses," *Phys. Rev. A*, vol. 40, p. 6741, 1989.

[7] N. V. Vitanov, K.-A. Suominen, and B. W. Shore, "Creation of coherent atomic superpositions by fractional stimulated Raman adiabatic passage," *J. Phys. B: At. Mol. Phys.*, vol. 32, p. 4535, 1999.

[8] U. Gaubatz, P. Rudecki, S. Schiemann, and K. Bergmann, "Population transfer between molecular vibrational levels by stimulated Raman scattering with partially overlapping laser fields. A new concept and experimental results," *J. Chem. Phys.*, vol. 92, p. 5363, 1990.

[9] P. A. Ivanov, N. V. Vitanov, and K. Bergmann, "Spontaneous emission in stimulated Raman adiabatic passage," *Phys. Rev. A*, vol. 72, p. 053412, 2005.

[10] R. R. Moseley, S. Shepherd, D. J. Fulton, B. D. Sinclair, and M. H. Dunn, "Spatial consequences of electromagnetically induced transparency: Observation of electromagnetically induced focusing," *Phys. Rev. Lett.*, vol. 74, p. 670, 1995.

[11] J. P. Marangos, "Topical review electromagnetically induced transparency," *J. Mod. Opt.*, vol. 45, p. 471, 1998.

Bibliography

[12] M. Fleischhauer, A. Imamoglu, and J. P. Marangos, "Electromagnetically induced transparency: Optics in coherent media," *Rev. Mod. Phys.*, vol. 77, p. 633, 2005.

[13] J. B. Johnson, S. Allen, D. R. Britton, J. Burdin, J. L. Hicks, K. Lyon, and W. D. Murry, "Picosecond multiphoton STIRAP detection of gas phase species: a test with sodium," *Proc. SPIE*, vol. 7304, p. 73040U, 2009.

[14] B. W. Shore, "Examples of counter-intuitive physics," *Contemp. Phys.*, vol. 36, p. 15, 1995.

[15] R. E. Blankenship, *Molecular mechanisms of photosynthesis.* Blackwell Science Ltd, 2002.

[16] N. H. Rizvi, P. M. W. French, and J. R. Taylor, "Generation of 33-fs pulses from a passively mode-locked Cr^{3+}:LiSrAlF$_6$ laser," *Opt. Lett.*, vol. 17, p. 1605, 1992.

[17] W. Min, S. Lu, G. R. Holtom, and X. S. Xie, "Triple-resonance coherent anti-stokes Raman scattering microspectroscopy," *ChemPhysChem*, vol. 10, p. 344, 2009.

[18] W. Min, S. Lu, M. Rueckel, G. R. Holtom, and S. Xie, "Near-degenerate four-wave-mixing microscopy," *Nano Lett.*, vol. 9, p. 2423, 2009.

[19] Schrödinger LLC, *PyMOL Molecular Graphics System.* v. 1.4.1.

[20] L.-M. Duan, M. D. Lukin, J. I. Cirac, and P. Zoller, "Long-distance quantum communication with atomic ensembles and linear optics," *Nature (London)*, vol. 414, p. 413, 2001.

[21] L.-M. Duan, "Entangling many atomic ensembles through laser manipulation," *Phys. Rev. Lett.*, vol. 88, p. 170402, 2002.

[22] C. H. van der Wal, M. D. Eisaman, A. André, R. L. Walsworth, D. F. Phillips, A. S. Zibrov, and M. D. Lukin, "Atomic memory for correlated photon states," *Science*, vol. 301, p. 196, 2003.

[23] A. Kuzmich, W. P. Bowen, A. D. Boozer, A. Boca, C. W. Chou, L.-M. Duan, and H. J. Kimble, "Generation of nonclassical photon pairs for scalable quantum communication with atomic ensembles," *Nature (London)*, vol. 423, p. 731, 2003.

[24] N. Sangouard, C. Simon, H. de Riedmatten, and N. Gisin, "Quantum repeaters based on atomic ensembles and linear optics," *Rev. Mod. Phys.*, vol. 83, p. 33, 2011.

[25] D. N. Matsukevich, T. Chanelière, M. Bhattacharya, S.-Y. Lan, S. D. Jenkins, T. A. B. Kennedy, and A. Kuzmich, "Entanglement of a photon and a collective atomic excitation," *Phys. Rev. Lett.*, vol. 95, p. 040405, 2005.

[26] D. Felinto, C. W. Chou, H. de Riedmatten, S. V. Polyakov, and H. J. Kimble, "Control of decoherence in the generation of photon pairs from atomic ensembles," *Phys. Rev. A*, vol. 72, p. 053809, 2005.

[27] R. Inoue, N. Kanai, T. Yonehara, Y. Miyamoto, M. Koashi, and M. Kozuma, "Entanglement of orbital angular momentum states between an ensemble of cold atoms and a photon," *Phys. Rev. A*, vol. 74, p. 053809, 2006.

[28] L. M. Duan, J. I. Cirac, and P. Zoller, "Three-dimensional theory for interaction between atomic ensembles and free-space light," *Phys. Rev. A*, vol. 66, p. 023818, 2002.

[29] D. Porras and J. I. Cirac, "Collective generation of quantum states of light by entangled atoms," *Phys. Rev. A*, vol. 78, p. 053816, 2008.

[30] M. O. Scully and M. S. Zubairy, "Playing tricks with slow light," *Science*, vol. 301, p. 181, 2003.

[31] M. O. Scully, E. S. Fry, C. H. R. Ooi, and K. Wódkiewicz, "Directed spontaneous emission from an extended ensemble of n atoms: Timing is evertyhing," *Phys. Rev. Lett.*, vol. 96, p. 010501, 2006.

[32] P. D. Lett, R. N. Watts, C. I. Westbrook, W. D. Phillips, P. L. Gould, and H. J. Metcalf, "Observation of atoms laser cooled below the doppler limit," *Phys. Rev. Lett.*, vol. 61, p. 169, 1988.

[33] C. I. Westbrook, R. N. Watts, C. E. Tanner, S. L. Rolston, W. D. Phillips, P. D. Lett, and P. L. Gould, "Localization of atoms in a three-dimensional standing wave," *Phys. Rev. Lett.*, vol. 65, p. 33, 1990.

[34] J. Y. Courtois, G. Grynberg, B. Lounis, and P. Verkerk, "Recoil-induced resonances in cesium: An atomic analog to the free-electron laser," *Phys. Rev. Lett.*, vol. 72, p. 3017, 1994.

[35] M. Mitsunaga, M. Yamashita, M. Koashi, and N. Imoto, "Temperature diagnostics for cold sodium atoms by transient four-wave mixing," *Opt. Lett.*, vol. 23, p. 840, 1998.

[36] J. H. Eberly, "Emission of one photon in an electric dipole transition of one among n atoms," *J. Phys. B: At. Mol. Opt. Phys.*, vol. 39, p. S599, 2006.

[37] P. D. Lett, W. D. Phillips, S. L. Rolston, C. E. Tanner, R. N. Watts, and C. I. Westbrook, "Optical molasses," *J. Opt. Soc. Am. B*, vol. 6, p. 2084, 1989.

[38] X. Y. Zou, L. J. Wang, and L. Mandel, "Induced coherence and indistinguishability in optical interference," *Phys. Rev. Lett.*, vol. 67, p. 318, 1991.

[39] L. Mandel, "Quantum effects in one-photon and two-photon interference," *Rev. Mod. Phys.*, vol. 71, p. S274, 1999.

[40] W. Denk, J. H. Strickler, and W. W. Webb, "Two-photon laser scanning fluorescence microscopy," *Science*, vol. 248, p. 73, 1990.

[41] J. J. Hopfield and J. M. Worlock, "Two-quantum absorption spectrum of KI and CsI," *Phys. Rev.*, vol. 137, p. A1455, 1965.

[42] S. Mukamel, *Principles of Nonlinear Optical Spectroscopy.* Oxford University Press, 1995.

[43] L. Mandel and E. Wolf, *Optical Coherence and Quantum Optics.* Cambridge University Press, 1995.

[44] J. Javanainen and P. L. Gould, "Linear intensity dependence of a two-photon transition rate," *Phys. Rev. A*, vol. 41, p. 5088, 1990.

Bibliography

[45] H.-B. Fei, B. M. Jost, S. Popescu, B. E. A. Saleh, and M. C. Teich, "Entanglement-induced two-photon transparency," *Phys. Rev. Lett.*, vol. 78, p. 1679, 1997.

[46] B. E. A. Saleh, H.-B. F. B. M. Jost, and M. C. Teich, "Entangled-photon virtual-state spectroscopy," *Phys. Rev. Lett.*, vol. 80, p. 3483, 1998.

[47] J. Kojima and Q.-V. Nguyen, "Entangled biphoton virtual-state spectroscopy of the $A^2\Sigma^+ - X^2\Pi$ system of OH," *Chem. Phys. Lett.*, vol. 396, p. 323, 2004.

[48] F. Schlawin, K. E. Dorfman, B. P. Fingerhut, and S. Mukamel, "Manipulation of two-photon fluorescence spectra of chromophore aggregates with entangled photons," *Phys. Rev. A*, vol. 86, p. 023851, 2012.

[49] M. B. Nasr, B. E. A. Saleh, A. V. Sergienko, and M. C. Teich, "Demonstration of dispersion-canceled quantum-optical coherence tomography," *Phys. Rev. Lett.*, vol. 91, p. 083601, 2003.

[50] J. L. Gouët, D. Venkatraman, F. N. C. Wong, and J. H. Shapiro, "Experimental realization of phase-conjugate optical coherence tomography," *Opt. Lett.*, vol. 35, p. 1001, 2010.

[51] J. D. Franson, "Nonlocal cancellation of dispersion," *Phys. Rev. A*, vol. 45, p. 3126, 1992.

[52] J. Brendel, H. Zbinden, and N. Gisin, "Nonlocal dispersion cancellation using entangled photons," *Opt. Comm.*, vol. 151, p. 35, 1998.

[53] S.-Y. Baek, Y.-W. Cho, and Y.-H. Kim, "Nonlocal dispersion cancellation using entangled photons," *Opt. Express*, vol. 17, p. 19241, 2009.

[54] V. Torres-Company, A. Valencia, M. Hendrych, and J. P. Torres, "Cancellation of dispersion and temporal modulation with nonentangled frequency-correlated photons," *Phys. Rev. A*, vol. 83, p. 023824, 2011.

[55] V. Torres-Company, J. P. Torres, and A. T. Friberg, "Shaping the ultrafast temporal correlations of thermal-like photons," *Phys. Rev. Lett.*, vol. 109, p. 243905, 2012.

[56] S. E. Harris, "Nonlocal modulation of entangled photons," *Phys. Rev. A*, vol. 78, p. 021807, 2008.

[57] S. Sensarn, G. Y. Yin, and S. E. Harris, "Observation of nonlocal modulation with entangled photons," *Phys. Rev. Lett.*, vol. 103, p. 163601, 2009.

[58] B. Dayan, A. Pe'er, A. A. Friesem, and Y. Silberberg, "Nonlinear interactions with an ultrahigh flux of broadband entangled photons," *Phys. Rev. Lett.*, vol. 94, p. 043602, 2005.

[59] D.-I. Lee and T. G. III, "Entangled photon absorption in an organic porphyrin dendrimer," *J. Phys. Chem. Lett. B*, vol. 110, p. 25582, 2006.

[60] D.-I. Lee and T. G. III, "Entangled and correlated two-photon absorption effects of an organic material," *IEEE/LEOS Summer Topical Meetings, 2007 Digest of the*, pp. 15–16, 2007.

[61] B. W. Shore, "Definition of virtual levels," *Am. J. Phys.*, vol. 47, p. 262, 1979.

[62] J. J. Sakurai, *Modern Quantum Mechanics.* Addison-Wesley, 1994.

[63] J. P. Jr, B. E. A. Saleh, and M. C. Teich, "Multiphoton absorption cross section and virtual-state spectroscopy for the entangled n-photon state," *Phys. Rev. A*, vol. 57, p. 3972, 1998.

[64] B. R. Mollow, "Two-photon absorption and field correlation functions," *Phys. Rev.*, vol. 175, p. 1555, 1968.

[65] J. P. Torres, K. Banaszek, and I. A. Walmsley, "Engineering nonlinear optic sources of photonic entanglement," *Progress in Optics*, vol. 56, p. 227, 2011.

[66] C. K. Law, I. A. Walmsley, and J. H. Eberly, "Continuous frequency entanglement: Effective finite Hilbert space and entropy control," *Phys. Rev. Lett.*, vol. 84, p. 5304, 2000.

[67] R. C. Etherton, L. M. Beyer, W. E. Maddox, and L. B. Bridwell, "Lifetimes of 3p, 4p, and 5p states in atomic hydrogen," *Phys. Rev. A*, vol. 2, p. 2177, 1970.

[68] C. L. Cesar, D. G. Fried, T. C. Killian, A. D. Polcyn, J. C. Sandberg, I. A. Yu, T. J. Greytak, D. Kleppner, and J. M. Doyle, "Two-photon spectroscopy of trapped atomic hydrogen," *Phys. Rev. Lett.*, vol. 77, p. 255, 1996.

[69] H. A. Bethe and E. E. Salpeter, *Quantum Mechanics of One- and Two-Electron Atoms.* Dover Publications, 2008.

[70] H. B. Bebb and A. Gold, "Multiphoton ionization of hydrogen and rare-gas atoms," *Phys. Rev.*, vol. 143, p. 1, 1966.

[71] O. Roslyak and S. Mukamel, "Multidimensional pump-probe spectroscopy with entangled twin-photon states," *Phys. Rev. A*, vol. 79, p. 063409, 2009.

[72] T. E. Keller and M. H. Rubin, "Theory of two-photon entanglement for spontaneous parametric down-conversion driven by a narrow pump pulse," *Phys. Rev. A*, vol. 56, p. 1534, 1997.

[73] M. Hendrych, M. Micuda, and J. P. Torres, "Tunable control of the frequency correlations of entangled photons," *Opt. lett.*, vol. 32, p. 2339, 2007.

[74] B. D. Fried and S. D. Conte, *The Plasma Dispersion Function.* Academic Press, 1961.

[75] T. Nakanishi, H. Kobayashi, K. Sugiyama, and M. Kitano, "Full quantum analysis of two-photon absorption using two-photon wavefunction: comparison of two-photon absorption with one photon absorption," *J. Phys. Soc. Jpn.*, vol. 78, p. 104401, 2009.

[76] A. Joobeur, B. E. A. Saleh, and M. C. Teich, "Spatiotemporal coherence properties of entangled light beams generated by parametric down-conversion," *Phys. Rev. A*, vol. 50, p. 3349, 1994.

[77] Y. H. Shih and A. V. Sergienko, "A two-photon interference experiment using type II optical parametric down conversion," *Phys. Lett. A*, vol. 191, p. 201, 1994.

[78] J. Frenkel, "On the transformation of light into heat in solids," *Phys. Rev.*, vol. 37, p. 17, 1931.

[79] J. Franck and E. Teller, "Migration and photochemical action of excitation energy in crystals," *J. Chem. Phys.*, vol. 6, p. 861, 1938.

[80] T. Förster, *Modern Quantum Chemistry.* Academic, 1965.

[81] R. E. Blankenship, *Molecular mechanisms of photosynthesis.* Blackwell Science Ltd, 2002.

[82] P. Ball, "Physics of life: The dawn of quantum biology," *Nature*, vol. 474, p. 272, 2011.

[83] N. Lambert, Y. N. Chen, Y. C. Cheng, C. M. Li, G. Y. Chen, and F. Nori, "Quantum biology," *Nat. Phys.*, vol. 9, p. 10, 2013.

[84] S. F. Huelga and M. B. Plenio, "Vibrations, quanta and biology," *Contemp. Phys.*, vol. 54, p. 181, 2013.

[85] G. S. Engel, T. R. Calhoun, E. L. Read, T.-K. Ahn, T. Mančal, Y.-C. Chen, R. E. Blankenship, and G. R. Fleming, "Evidence for wavelike energy transfer through quantum coherence in photosynthetic systems," *Nature*, vol. 446, p. 782, 2007.

[86] G. Panitchayangkoon, D. Hayes, K. A. Fransted, J. R. Caram, E. Harel, J. Wen, R. E. Blankenship, and G. S. Engel, "Long-lived quantum coherence in photosynthetic complexes at physiological temperature," *Proc. Natl. Acad. Sci.*, vol. 107, p. 12766, 2010.

[87] E. Collini, C. Y. Wong, K. E. Wilk, P. M. G. Curmi, P. Brumer, and G. D. Scholes, "Coherently wired light-harvesting in photosynthetic marine algae at ambient temperature," *Nature*, vol. 463, p. 644, 2010.

[88] C. Y. Wong, R. M. Alvey, D. B. Turner, K. E. Wilk, D. A. Bryant, P. M. G. Curmi, R. J. Silbey, and G. D. Scholes, "Electronic coherence lineshapes reveal hidden excitonic correlations in photosynthetic light harvesting," *Nature Chem.*, vol. 4, p. 396, 2012.

[89] A. Ishizaki and G. R. Fleming, "Unified treatment of quantum coherent and incoherent hopping dynamics in electronic energy transfer: reduced hierarchy equation approach," *J. Chem. Phys.*, vol. 130, p. 234111, 2009.

[90] A. Ishizaki and G. R. Fleming, "Theoretical examination of quantum coherence in a photosynthetic system at physiological temperature," *Proc. Natl. Acad. Sci.*, vol. 106, p. 17255, 2009.

[91] S. Hoyer, M. Sarovar, and K. B. Whaley, "Limits of quantum speedup in photosynthetic light harvesting," *New J. Phys.*, vol. 12, p. 065041, 2010.

[92] F. Fassioli and A. Olaya-Castro, "Distribution of entanglement in light-harvesting complexes and their quantum efficiency," *New J. Phys.*, vol. 12, p. 085006, 2010.

[93] J. Strümpfer, M. Şener, and K. Schulten, "How quantum coherence assists photosynthetic light-harvesting," *J. Phys. Chem. Lett.*, vol. 3, p. 536, 2012.

[94] T. Fujita, J. C. Brookes, S. K. Saikin, and A. Aspuru-Guzik, "Memory-assisted exciton diffusion in the chlorosome light-harvesting antenna of green sulfur bacteria," *J. Phys. Chem. Lett.*, vol. 3, p. 2357, 2012.

[95] I. Kassal, J. Yuen-Zhou, and S. Rahimi-Keshari, "Does coherence enhance transport in photosynthesis?," *J. Phys. Chem. Lett.*, vol. 4, p. 362, 2013.

[96] P. Rebentrost, M. Mohseni, I. Kassal, S. Lloyd, and A. Aspuru-Guzik, "Environment-assisted quantum transport," *New J. Phys.*, vol. 11, p. 033003, 2009.

[97] M. Plenio and S. Huelga, "Dephasing-assisted transport: quantum networks and biomolecules," *New J. Phys.*, vol. 10, p. 113019, 2008.

[98] P. W. Anderson, "Absence of diffusion in certain random lattices," *Phys. Rev.*, vol. 109, p. 1492, 1958.

[99] I. Kassal and A. Aspuru-Guzik, "Environment-assisted quantum transport in ordered systems," *New J. Phys.*, vol. 14, p. 053041, 2012.

[100] A. Eisfeld and J. S. Briggs, "Classical master equation for excitonic transport under the influence of an environment," *Phys. Rev. E*, vol. 85, p. 046118, 2012.

[101] J. S. Briggs and A. Eisfeld, "Equivalence of quantum and classical coherence in electronic energy transfer," *Phys. Rev. E*, vol. 83, p. 051911, 2011.

[102] V. May and O. Kühn, *Charge and Energy Transfer Dynamics in Molecular Systems.* Wiley-VCH, Weinheim, 3 ed., 2011.

[103] H.-P. Breuer and F. Petruccione, *The Theory of Open Quantum Systems.* Oxford University Press, 2002.

[104] A. Ishizaki and G. R. Fleming, "On the adequacy of the Redfield equation and related approaches to the study of quantum dynamics in electronic energy transfer," *J. Chem. Phys.*, vol. 130, p. 234110, 2009.

[105] M. Scully and M. S. Zubairy, *Quantum Optics.* Cambridge University Press, 2006.

[106] F. Strocchi, "Complex coordinates and quantum mechanics," *Rev. Mod. Phys.*, vol. 38, p. 36, 1966.

[107] R. Kubo, "Stochastic Liouville equations," *J. Math. Phys.*, vol. 4, p. 174, 1963.

[108] R. F. Fox, "Gaussian stochastic processes in physics," *Phys. Rep.*, vol. 48, p. 179, 1978.

[109] N. G. van Kampen, "Itô versus Stratonovich," *J. Stat. Phys.*, vol. 24, p. 175, 1981.

[110] J. Adolphs and T. Renger, "How proteins trigger excitation energy transfer in the FMO complex of green sulfur bacteria," *Biophys. J.*, vol. 91, p. 2778, 2006.

[111] R. E. Fenna and B. W. Matthews, "Chlorophyll arrangement in a bacteriochlorophyll protein from chlorobium limicola," *Nature*, vol. 258, p. 573, 1975.

Bibliography

[112] C. Sybesma and J. M. Olson, "Transfer of chlorophyll excitation energy in green photosynthetic bacteria," *Proc. Natl Acad. Sci. (USA)*, vol. 49, p. 248, 1963.

[113] M. Mohseni, P. Rebentrost, S. Lloyd, and A. Aspuru-Guzik, "Environment-assisted quantum walks in photosynthetic energy transfer," *J. Chem. Phys.*, vol. 129, p. 174106, 2008.

[114] J. S. Briggs and A. Eisfeld, "Coherent quantum states from classical oscillator amplitudes," *Phys. Rev. A*, vol. 85, p. 052111, 2012.

[115] S. Mostame, P. Rebentrost, A. Eisfeld, A. J. Kerman, D. I. Tsomokos, and A. Aspuru-Guzik, "Quantum simulator of an open quantum system using superconducting qubits: exciton transport in photosynthetic complexes," *New. J. Phys.*, vol. 14, p. 105013, 2012.

[116] F. Caruso, N. Spagnolo, C. Vitelli, F. Sciarrino, and M. B. Plenio, "Simulation of noise-assisted transport via optical cavity networks," *Phys. Rev. A*, vol. 83, p. 013811, 2011.

[117] P. Hänggi and F. Marchesoni, "Artificial Brownian motors: Controlling transport on the nanoscale," *Rev. Mod. Phys.*, vol. 81, p. 387, 2009.

[118] M. Gitterman, *The Noisy Oscillator: The First Hundred Years, From Einstein Until Now.* World Scientific, 2005.

[119] R. Graham, M. Höhnerbach, and A. Schenzle, "Statistical properties of light from a dye laser," *Phys. Rev. Lett.*, vol. 48, p. 1396, 1982.

[120] A. Ishimaru, *Wave propagation and Scattering in Random Media.* IEEE Press, 1997.

[121] M. Turelli, "Random environments and stochastic calculus," *Theoretical Population Biology*, vol. 12, p. 140, 1977.

[122] H. Takayasu, A.-H. Sato, and M. Takayasu, "Stable infinite variance fluctuations in randomly amplified Langevin systems," *Phys. Rev. Lett.*, vol. 79, p. 966, 1997.

[123] R. de J. León-Montiel and J. P. Torres, "Highly efficient noise-assisted energy transport in classical oscillator systems," *Phys. Rev. Lett.*, vol. 110, p. 218101, 2013.

[124] R. Berthet, A. Petrossian, S. Residori, B. Roman, and S. Fauve, "Effect of multiplicative noise on parametric instabilities," *Physica D*, vol. 174, p. 84, 2003.

[125] M. Gitterman and D. A. Kessler, "Mass dependence of instabilities of an oscillator with multiplicative and additive noise," *Phys. Rev. E*, vol. 87, p. 022137, 2013.

[126] C. Laing and G. J. Lord, *Stochastic Methods in Neuroscience.* Clarendon Press, 2008.

[127] N. G. V. Kampen, *Stochastic Processes in Physics and Chemistry.* Elsevier, 2007.

[128] K. Jacobs, *Stochastic Processes for Physicists: Understanding Noisy Systems.* Cambridge University Press, 2010.

[129] A. Chin, A. Datta, F. Caruso, S. Huelga, and M. Plenio, "Noise-assisted energy transfer in quantum networks and light-harvesting complexes," *New J. Phys.*, vol. 12, p. 065002, 2010.

[130] A. Shabani, M. Mohseni, H. Rabitz, and S. Lloyd, "Efficient estimation of energy transfer efficiency in light-harvesting complexes," *Phys. Rev. E*, vol. 86, p. 011915, 2012.

[131] K. M. Pelzer, A. F. Fidler, G. B. Griffin, S. K. Gray, and G. S. Engel, "The dependence of exciton transport efficiency on spatial patterns of correlation within the spectral bath," *New J. Phys.*, vol. 15, no. 9, p. 095019, 2013.

[132] M. Mohseni, A. Shabani, S. Lloyd, and H. Rabitz, "Energy-scales convergence for optimal and robust quantum transport in photosynthetic complexes," *J. Chem. Phys.*, vol. 140, no. 3, p. 035102, 2014.

[133] T. Mančal and L. Valkunas, "Exciton dynamics in photosynthetic complexes: Excitation by coherent and incoherent light," *New J. Phys.*, vol. 12, p. 065044, 2010.

[134] D. Manzano, "Quantum transport in networks and photosynthetic complexes at the steady state.," *PLoS One*, vol. 8, no. 2, p. e57041, 2013.

[135] A. Chenu, P. Malý, and T. Mančal, "Dynamic coherence in excitonic molecular complexes under various excitation conditions," p. arXiv:1306.1693, 2013.

[136] S. Jesenko and M. Žnidarič, "Excitation energy transfer efficiency: Equivalence of transient and stationary setting and the absence of non-Markovian effects," *J. Chem. Phys.*, vol. 138, p. 174103, 2013.

[137] X.-P. Jiang and P. Brumer, "Creation and dynamics of molecular states prepared with coherent vs partially coherent pulsed light," *J. Chem. Phys.*, vol. 94, p. 5833, 1991.

[138] P. Brumer and M. Shapiro, "Molecular response in one photon absorption: Coherent pulsed laser vs. thermal incoherent source," *Proc. Natl. Acad. Sci.*, vol. 109, p. 19575, 2012.

[139] K. Hoki and P. Brumer, "Excitation of biomolecules by coherent vs. incoherent light: Model rhodopsin photoisomerization," *Procedia Chem.*, vol. 3, p. 122, 2011.

[140] F. Fassioli, A. Olaya-Castro, and G. D. Scholes, "Coherent energy transfer under incoherent light conditions," *J. Phys. Chem. Lett.*, vol. 3, p. 3136, 2012.

[141] F. Caruso, A. W. Chin, A. Datta, S. F. Huelga, and M. B. Plenio, "Highly efficient energy excitation transfer in light-harvesting complexes: The fundamental role of noise-assisted transport," *J. Chem. Phys.*, vol. 131, p. 105106, 2009.

[142] K. M. Pelzer, T. Can, S. K. Gray, D. Morr, and G. S. Engel, "Coherent transport and energy flow patterns in photosynthesis under incoherent excitation," *J Phys. Chem. B*, p. DOI:10.1021/jp500746a, 2014.

[143] X. Chen and R. J. Silbey, "Excitation energy transfer in a non-Markovian dynamical disordered environment: Localization, narrowing, and transfer efficiency," *J. Phys. Chem. B*, vol. 115, no. 18, p. 5499, 2011.

Appendix A

To numerically solve Eqs. (1.2), (1.4) and (1.5), let us consider a moving frame defined by the variables

$$
\begin{aligned}
z' &\equiv z, & \text{(A.1)} \\
t' &\equiv t - \frac{z}{c}. & \text{(A.2)}
\end{aligned}
$$

In this moving frame, the time and space derivatives read as

$$
\begin{aligned}
\frac{\partial}{\partial t} &= \frac{\partial t'}{\partial t}\frac{\partial}{\partial t'} + \frac{\partial z'}{\partial t}\frac{\partial}{\partial z'} = \frac{\partial}{\partial t'}, & \text{(A.3)} \\
\frac{\partial}{\partial z} &= \frac{\partial t'}{\partial z}\frac{\partial}{\partial t'} + \frac{\partial z'}{\partial z}\frac{\partial}{\partial z'} = \frac{\partial}{\partial z'} - \frac{1}{c}\frac{\partial}{\partial t'}. & \text{(A.4)}
\end{aligned}
$$

Using Eqs. (A.3) and (A.4), the equation describing the evolution of the atomic ensemble [Eq. (1.2)] can be rewritten as

$$
\frac{\partial}{\partial t'}\rho\left(z',t'\right) = -\frac{i}{\hbar}\left\{\left[H\left(z',t'\right),\rho\left(z',t'\right)\right] + \mathcal{L}_{\text{diss}}[\rho\left(z',t'\right)]\right\}, \tag{A.5}
$$

where

$$
H\left(z',t'\right) = \frac{\hbar}{2}\begin{bmatrix} 0 & \Omega_{\text{p}}^*\left(z',t'\right) & 0 \\ \Omega_{\text{p}}\left(z',t'\right) & 2\Delta_{\text{p}} & \Omega_{\text{s}}\left(z',t'\right) \\ 0 & \Omega_{\text{s}}^*\left(z',t'\right) & 2\left(\Delta_{\text{p}} - \Delta_{\text{s}}\right) \end{bmatrix}. \tag{A.6}
$$

In the same fashion, the evolution of the optical fields [Eqs. (1.4) and (1.5)] take the form

$$
\begin{aligned}
\frac{\partial}{\partial z'}\Omega_{\text{p}}\left(z',t'\right) &= -iq_{\text{p}}\rho_{12}^*\left(z',t'\right), & \text{(A.7)} \\
\frac{\partial}{\partial z'}\Omega_{\text{s}}\left(z',t'\right) &= -iq_{\text{s}}\rho_{32}^*\left(z',t'\right), & \text{(A.8)}
\end{aligned}
$$

where $q_{\text{p,s}} = \alpha_{\text{p,s}}/c$.

Notice that the set of Eqs. (A.5), (A.7) and (A.8) can be solved by iteratively

computing the evolution of the atomic ensemble and the optical fields, in small steps of time $\Delta t'$ and distance $\Delta z'$. The iterative procedure starts by solving Eq. (A.5) for a time $t'_0 + \Delta t'$. Then, the obtained solutions $\rho_{ij}\left(z', t'_0 + \Delta t'\right)$ are used to calculate the evolution of the optical fields for a propagation distance $z'_0 + \Delta z'$. Finally, the result of this calculation $\Omega_{\mathrm{p,s}}\left(z'_0 + \Delta z', t'_0 + \Delta t'\right)$ is introduced into the Hamiltonian (A.6) to compute Eq. (A.5) for the next time step $t'_0 + 2\Delta t'$ and continue with the iterative computation. It is important to remark that once the calculation is finished, we need to transform the variables z' and t', by means of the relations (A.1) and (A.2), in order to obtain the real values of the propagation distance z and time t.

In this appendix, we describe how to numerically solve the classical equations (4.14). For this, we first introduce the auxiliary matrices

$$R_{nm} = \langle \widetilde{q}_n \widetilde{q}_m \rangle, \tag{B.1}$$

$$S_{nm} = \langle \widetilde{p}_n \widetilde{p}_m \rangle, \tag{B.2}$$

$$T_{nm} = \langle \widetilde{q}_n \widetilde{p}_m \rangle. \tag{B.3}$$

Using these new operators, the classical master equation takes the form

$$\sigma_{nm} = R_{nm} + S_{nm} + i\left(T_{mn} - T_{nm}\right). \tag{B.4}$$

In Ref. [100], Eisfeld and Briggs have demonstrated that one can make use of the time evolution equations of $\widetilde{q}_n$ and $\widetilde{p}_n$ to derive the set of coupled equations

$$\frac{\partial R_{nm}}{\partial t} = \omega_n T_{mn} + \omega_m T_{nm} + \mathcal{L}\left[R\right]_{nm}, \tag{B.5}$$

$$\frac{\partial S_{nm}}{\partial t} = -\left(\omega_n T_{nm} + \omega_m T_{mn}\right) - \sum_j \left(\frac{2V_{nj}}{\hbar} T_{jm} + \frac{2V_{mj}}{\hbar} T_{jn}\right) + \mathcal{L}\left[S\right]_{nm}, \tag{B.6}$$

$$\frac{\partial T_{nm}}{\partial t} = \omega_n S_{nm} - \omega_m R_{nm} - \sum_j \frac{2V_{mj}}{\hbar} R_{nj} + \mathcal{L}\left[T\right]_{nm}. \tag{B.7}$$

Now, to model the transfer of energy from the chosen site k to the reaction center, we directly introduce the corresponding decay operators into Eqs. (B.5)-(B.7), so the new set of equations describing the dynamics of the coupled oscillator network subjected to environmental noise, and energy transfer to a reaction center [Eq. (4.14)],

can be written as

$$
\frac{\partial R_{nm}}{\partial t} = \omega_n T_{mn} + \omega_m T_{nm} + \mathcal{L}\left[R\right]_{nm} + \mathcal{D}\left[R\right]_{nm}, \tag{B.8}
$$

$$
\frac{\partial S_{nm}}{\partial t} = -\left(\omega_n T_{nm} + \omega_m T_{mn}\right) - \sum_j \left(\frac{2V_{nj}}{\hbar}T_{jm} + \frac{2V_{mj}}{\hbar}T_{jn}\right)
$$
$$
+ \mathcal{L}\left[S\right]_{nm} + \mathcal{D}\left[S\right]_{nm}, \tag{B.9}
$$

$$
\frac{\partial T_{nm}}{\partial t} = \omega_n S_{nm} - \omega_m R_{nm} - \sum_j \frac{2V_{mj}}{\hbar}R_{nj} + \mathcal{L}\left[T\right]_{nm} + \mathcal{D}\left[T\right]_{nm}. \tag{B.10}
$$

The solutions of Eqs. (B.8)-(B.10) are then substituted into Eq. (B.4) in order to compute the time evolution of the population of each oscillator and calculate the energy transfer efficiency given by Eq. (4.17). Notice that in the classical model [Eq. (4.14)], the number of coupled differential equations that needs to be solved is three times larger than in the quantum case [Eq. (4.2)], which implies that the solution to the classical equations is more computationally demanding. Therefore, in order to reduce the computation time of our simulations, we have made use of adaptive methods for solving systems of ordinary differential equations, such as the ode-solver functions provided by MATLAB.